



Universidad
Zaragoza



Instituto Universitario de Investigación
en Ingeniería de Aragón
Universidad Zaragoza

Ph.D. Thesis

Characterization of Cardiovascular Remodeling Following Intrauterine Growth Restriction

Caracterización del remodelamiento cardiovascular
subsecuente a la restricción de crecimiento intrauterino

Autor

Freddy Leonardo Bueno Palomeque

Supervisors

Ana Mincholé Lapuente

Pablo Laguna Lasaosa

Instituto de Investigación en Ingeniería de Aragón
Universidad de Zaragoza

2025

Characterization of Cardiovascular Remodeling Following Intrauterine Growth Restriction

Freddy Leonardo Bueno Palomeque, 2025

Characterization of Cardiovascular Remodeling Following Intrauterine Growth Restriction

Date of current version: Friday 16th May, 2025

This Ph.D. thesis belongs to the inter-university Biomedical Engineering Ph.D. Program of the University of Zaragoza and Polytechnic University of Cataluña, and has been developed within the Biomedical Signal Interpretation and Computational Simulations (BSICoS) group of the Aragón Institute for Engineering Research (I3A), and the Department of Electronic Engineering and Communications at the University of Zaragoza (Zaragoza, Spain).

The research presented in this thesis was supported by projects PID2021-128972OA-I00, PID2022-140556OB-I00, CNS2022-135899 and TED2021-130459B-I00 funded by MCIN/AEI, by fellowship RYC2019-027420-I funded by Ramón y Cajal Program, by BSICoS group T39_23R from Aragon government and by PhD scholarship to Freddy Leonardo Bueno-Palomeque from Fundación Carolina, Universidad de Zaragoza, and Universidad Politécnica Salesiana. Computations were performed using ICTS NAN-BIOSIS (HPC Unit 27).

This thesis was printed thanks to the financial support of BSICoS Group at University of Zaragoza.



El latido del corazón es más fuerte cuando late en compañía.

A Noemí, Leonela, Joaquín y Gabriel.

Intrauterine growth restriction (IUGR) and preterm birth are linked to cardiovascular remodeling, which often manifests as a decrease in cardiac sphericity index (base-to-apex length/basal diameter ratio). These changes induced by IUGR are more pronounced in the left ventricle, can persist throughout life, and are associated with an increased predisposition to heart disease in adulthood.

Various studies conducted across different age groups have demonstrated the prevalence of these anatomical changes in cardiac muscle. In addition to morphological remodeling, assessed through the ventricular sphericity index, alterations in cardiac electrical function have been reported through the characterization of the depolarization and repolarization loops and their angular relationship as measured in a vectorcardiogram (VCG).

Variations in the duration of electrocardiogram (ECG) interval biomarkers have shown increased depolarization and repolarization phases in individuals with a history of fetal IUGR. However, additional studies present contradictory trends in these variations. While the effects of IUGR on cardiac electrophysiology are evident, the underlying relationship between morphological remodeling and the angular variation of the dominant QRS and T-wave vectors remains largely unexplored.

This study aimed to simulate the geometric changes induced by IUGR in a realistic biventricular heart and torso model, and to evaluate their impact on cardiac electrophysiology. This was carried out in three stages. In the first stage, we started with a control computational model and generated eight globular cardiac models (\mathcal{G}_A to \mathcal{G}_H) by reducing the apex-base length and increasing the ventricular basal diameter. We calculated the dominant QRS and T-wave vectors and angles from simulated pseudo-ECGs, comparing them with clinical measurements.

In the second stage, the ECG of preadolescents with IUGR was charac-

terized by comparing biomarkers such as the duration of the QRS complex (QRS_d), the T-peak to T-end interval (T_{pe}), and the QT interval between a control group and an IUGR group. We analyzed 12-lead ECG recordings from 33 subjects who had severe IUGR at birth and 60 control subjects, using spatial principal component analysis (PCA) to emphasize the QRS complexes and T waves.

Finally, in the third stage, to deepen the understanding of the effects induced by geometric changes, we conducted computational electrophysiological simulations based on eight different anatomical models derived from IUGR clinical data (\mathcal{G}_1 to \mathcal{G}_8). These models incorporated additional key geometric alterations such as ventricular wall thickness, and tissue volume. With these models, we evaluated the impact of cardiac anatomical variation on the studied biomarkers (QRS_d , T_{pe} , and the QT interval) and compared them with clinical results.

The *in silico* results from the first stage showed that the angles of the loops for both the QRS complex and the T-wave measured in the globular heart models exhibit a change consistent with those reported in clinical results, strengthening the hypothesis that morphological changes induced by IUGR could contribute to explaining the observed angular changes.

The clinical results from the second stage showed that for the IUGR group, the QRS_d and T_{pe} were significantly wider than in the control group, with no pronounced change in the QT interval.

In the third stage, the simulations revealed a significant prolongation of QRS_d , consistent with clinical findings. A moderate increase in the T_{pe} was also observed, aligning with clinical observations, while the prolongation of the QT interval partially contradicted clinical results. These findings suggest that while the simulated geometric changes replicate certain clinical observations, other factors such as changes in electrical activation and/or ionic remodeling might influence cardiac electrophysiology in IUGR cases.

This study highlights the impact of geometric and volumetric remodeling on the effects of IUGR on cardiac electrophysiology. It also emphasizes the need for further research on electrophysiological remodeling and its consequences for cardiac function.

Keywords: Intrauterine growth restriction, cardiac remodeling, electrophysiology, depolarization, repolarization, dominant vector, electrocardiogram, vectorcardiogram, QRS duration interval, T-peak to T-end interval, QT interval, biventricular model, globular model, apex-base length, basal diameter, sphericity index, ventricular wall thickness.

RESUMEN Y CONCLUSIONES

La restricción del crecimiento intrauterino (IUGR, por sus siglas en inglés) y el nacimiento prematuro están vinculados con el remodelamiento cardiovascular, el cual se manifiesta frecuentemente como una disminución del índice de esfericidad cardíaca (relación longitud base-ápex/diámetro basal). Estos cambios inducidos por IUGR son más pronunciados en el ventrículo izquierdo, pueden persistir a lo largo de la vida y están asociados con una mayor predisposición a enfermedades cardíacas en la adultez.

En diversos estudios realizados con diferentes grupos etarios, se ha evidenciado la prevalencia de estos cambios anatómicos en el músculo cardíaco. Además del remodelamiento morfológico del corazón, evaluado mediante el índice de esfericidad ventricular, se han reportado alteraciones en la función eléctrica cardíaca a través de la caracterización de los bucles de despolarización y repolarización y su relación angular, medidas en un vectorcardiogram (VCG).

Variaciones en los valores de los biomarcadores basados en intervalos temporales en el ECG han mostrado un incremento en las etapas de despolarización y repolarización en individuos con historial de IUGR durante la etapa fetal. No obstante, investigaciones adicionales presentan tendencias contrapuestas en estas variaciones. Aunque los efectos de IUGR sobre la electrofisiología cardíaca son evidentes, la relación subyacente entre el remodelamiento morfológico y la variación angular de los vectores dominantes QRS y T no ha sido explorada profundamente.

Este estudio tuvo como objetivo simular los cambios geométricos inducidos por IUGR en un modelo realista de corazón biventricular y de torso, y evaluar su impacto en la electrofisiología cardíaca. Esto se llevó a cabo en tres etapas. En la primera, partimos de un modelo computacional control y generamos ocho modelos cardíacos globulares (\mathcal{G}_A a \mathcal{G}_H) al reducir la longitud ápex-base y ampliar el diámetro basal ventricular. Calculamos los vectores y ángulos dominantes de QRS y onda T a partir de pseudo-ECG simulados, comparándolos

con mediciones clínicas.

En la segunda etapa, se caracterizó el ECG de preadolescentes con IUGR mediante la comparación de biomarcadores como la duración del complejo QRS (QRS_d), el intervalo de T-pico a T-fin (T_{pe}), y el intervalo QT entre un grupo control y otro IUGR. Analizamos registros de ECG de 12 derivaciones de 33 sujetos que presentaron IUGR severo al nacer y 60 sujetos control, utilizando el análisis de componentes principales (PCA) espaciales para enfatizar los complejos QRS y ondas T.

Finalmente, en la tercera etapa, para profundizar en el análisis de los efectos provocados por los cambios geométricos, realizamos simulaciones computacionales electrofisiológicas sobre ocho distintos modelos anatómicos derivados de datos clínicos de IUGR (\mathcal{G}_1 a \mathcal{G}_8). Estos modelos incluyeron alteraciones geométricas adicionales como el grosor de la pared ventricular y el volumen del tejido ventricular. Con estos modelos evaluamos el impacto de la variación anatómica cardíaca sobre los biomarcadores estudiados (QRS_d , T_{pe} y el intervalo QT) y los contrastamos con los resultados clínicos.

Los resultados *in silico* de la primera etapa, mostraron que los ángulos de los bucles tanto del complejo QRS como de la onda T medidos en los modelos globulares de corazón presentan un cambio congruente con los reportados en resultados clínicos, fortaleciendo la hipótesis de que los cambios morfológicos inducidos por IUGR podrían contribuir a explicar los cambios angulares evidenciados.

Los resultados clínicos de la segunda etapa mostraron para el grupo IUGR, un QRS_d y T_{pe} significativamente más anchos que el grupo control y un intervalo QT sin un cambio pronunciado.

En la etapa tres, los resultados de las simulaciones mostraron una prolongación significativa en la duración del complejo QRS, consistente con los hallazgos clínicos. También se observó un incremento moderado en el intervalo T_{pe} , alineado con las observaciones clínicas, mientras que la prolongación del intervalo QT contradice parcialmente los resultados clínicos. Estos hallazgos sugieren que, aunque los cambios geométricos simulados reproducen ciertas observaciones clínicas, otros factores como alteraciones en la activación eléctrica y/o remodelamiento iónico podrían estar influyendo en la electrofisiología cardíaca en casos de IUGR.

Este estudio subraya el impacto del remodelamiento geométrico y volumétrico en los efectos del IUGR sobre la electrofisiología cardíaca. Resalta también la necesidad de investigaciones futuras sobre el remodelamiento electrofisiológico y sus consecuencias en la función cardíaca.

Palabras clave: Restricción de crecimiento intrauterino, remodelamiento cardíaco, electrofisiología, despolarización, repolarización, vector dominante, electrocardiograma, vectorcardiograma, intervalo de duración QRS, intervalo T-pico a T-fin, intervalo QT, modelo biventricular, modelo globular, longitud ápex-base, diámetro basal, índice de esfericidad, ancho de pared ventricular.

ACKNOWLEDGEMENTS

First and foremost, I would like to express my gratitude to my supervisors for their guidance and support throughout this project. Thank you, Dr. Ana Mincholé, for helping me see the path beneath my feet and for pointing out the possible routes to continue moving forward. Your optimism and unwavering support have been invaluable. Thank you, Dr. Pablo Laguna, for your guidance and support in this project. Since your response to my first email on 22-02-2019 (it took you only 44 minutes to reply, and my whole life has changed because of it-thank you!), I have felt your support and guidance. Thank you, Dr. Esther Pueyo, for your guidance and support. This project has been enriching from multiple perspectives, and I am truly grateful to have had the best human and professional team as my mentors.

I would also like to extend my thanks to the entire BSICoS team, who, during my stays in Zaragoza since 2020, have made me feel at home.

Special thanks to Noemí, Leonela, Joaquín, and Gabriel for their support and patience over the years. This journey would not have been the same without you by my side.

To my parents, Freddy and Teresa, and my siblings, Lorena and Fernando, for their constant love and care. To my friends Edwin, Xavier, Efrén, and Dennis, for all the enjoyable conversations.

To all of you, beyond my gratitude, I dedicate this work.

Abstract		iii
Resumen y Conclusiones		v
Acknowledgements		ix
List of Acronyms		xv
1 Introduction		1
1.1 Framework of the Thesis		2
1.1.1 Motivation		2
1.1.2 Thesis goals		4
1.1.3 Thesis outline		6
1.2 Cardiac anatomy and function		11
1.3 Cardiac electrophysiology		13
1.3.1 Conduction system		13
1.3.2 Electrophysiological properties of myocardial cells		15
1.3.3 Spatial heterogeneities in depolarization and repolarization		18
1.4 Electrocardiogram and vectorcardiogram		18
1.4.1 Genesis of P, QRS and T waveforms, and their associated intervals		21
1.5 Intrauterine growth restriction and its cardiac impacts		22
1.5.1 Structural cardiac remodeling in IUGR		23
1.5.2 Electrophysiological changes in IUGR subjects		25
1.6 Biomarkers of cardiac electrophysiology		26

2	Methodology and computational models in cardiac electrophysiology	31
2.1	Modeling cardiac electrophysiology	32
2.1.1	Hodgkin-Huxley model	33
2.1.2	Ventricular action potential models	34
2.1.3	Bidomain and monodomain equations	35
2.2	Software and computational tools	37
2.2.1	Finite elements in electrophysiology	37
2.2.2	Simulation framework (ELECTRA)	39
2.3	Anatomical model with reduced sphericity index	42
2.3.1	Parameters controlling the deformation of the biventricular model	42
2.4	Signal processing and analysis	44
2.4.1	Pseudo-ECG generation and analysis	44
2.4.2	Dominant vectors of QRS and T Waves in VCG	45
2.4.3	Detection and delineation in ECG	45
2.4.4	Principal component analysis in ECG	48
2.4.5	Dataset	50
3	QRS-T angle changes in computational IUGR models	51
3.1	The conduction system in the computational model of human electrophysiology	52
3.1.1	Purkinje network	53
3.1.2	Fiber architecture	57
3.2	Transmural and apicobasal heterogeneities modeling intersubject variability	61
3.2.1	Endo-, mid-, and epi-cardium segmentation	61
3.2.2	Incorporation of apex-to-base heterogeneity	65
3.2.3	Generation of globular models	69
3.3	Confounding effect of heart location within the torso	72
3.4	Pseudo ECG/VCG calculation from the biventricular human model	73
3.5	Results	76
3.5.1	Transmural heterogeneities induced angular variation	76
3.5.2	Angular variation in globular, \mathcal{G} , models	79
3.5.3	Impact of electrode position	84
3.6	Discussion	85
3.6.1	Analysis of angular variability in simulation	85
3.6.2	Angular changes with electrode position	89
3.7	Conclusions	91

4	QRS width and T-peak to T-end interval in preadolescents with severe IUGR	93
4.1	Dataset and signal processing	94
4.1.1	Dataset	94
4.1.2	ECG waves delineation	94
4.1.3	ECG interval biomarkers from delineation marks	97
4.1.4	Optimal spatial transform leads for QRS or T waves measurement	98
4.2	Results	100
4.2.1	QRS width and T peak-to-end intervals in IUGR and control patients	100
4.2.2	Intervals result on PCA_{QRS} and PCA_T transform leads	104
4.3	Discussion	104
4.4	Conclusions	106
5	Cardiac remodeling electrophysiology in IUGR: Computational models insights	107
5.1	ECG biomarkers alterations as a consequence of IUGR	108
5.2	Computational modeling of human electrophysiology	108
5.2.1	Electrophysiological propagation	109
5.2.2	Transmural and apicobasal heterogeneities	110
5.2.3	ECG signal processing and the computation of biomarkers	112
5.2.4	Globular anatomical models with reduced sphericity index	112
5.3	Results	118
5.3.1	<i>In Silico</i> analysis of geometric effects on ECG biomarkers	118
5.3.2	Relationship between geometric variations and ECG biomarkers	120
5.3.3	Role of transmural heterogeneities	121
5.3.4	Mechanisms behind the subtle T_{pe} changes compared to the larger QRS_d changes	122
5.4	Discussion	126
5.4.1	Cardiac remodeling <i>in silico</i>	126
5.4.2	Impact of left basal diameter ϕ and wall width W in QRS_d	127
5.4.3	T_{pe} and QT intervals	128
5.5	Limitations	130
5.6	Conclusion	131
6	Conclusions and future work	133
6.1	Main findings	134

6.1.1	Angular variation of depolarization and repolarization loops <i>in silico</i>	134
6.1.2	ECG interval biomarkers in clinical studies	135
6.1.3	Biomarkers in the synthetic ECG	136
6.2	General conclusions	137
6.3	Perspectives for future work	138
	Bibliography	141
	List of Publications	157
	List of Figures	159
	List of Tables	167

LIST OF ACRONYMS

AGA	appropriate for gestational age	24
AP	action potential	13
APD	action potential duration	17
AV	atrioventricular	13
CV	conduction velocity	14
DWT	discrete wavelet transform	46
ECG	electrocardiogram	iii
endo	endocardial tissue	12
epi	epicardial tissue	12
FEM	finite element method	37
fMCG	fetal magnetocardiography	26
IUGR	intrauterine growth restriction	2
<i>L</i>	apex-base length	25
LV	left ventricle	3
mid	mid-myocardial tissue	12
ORd	O’Hara-Rudy action potential cell model	34
PCA	principal component analysis	48
PCA_{QRS}	PCA emphasizing the QRS complex	48
PCA_T	PCA emphasizing the T-wave	48
PMJ	Purkinje myocardial junctions	53
QRS_a	R amplitude	98

QRS_d	QRS duration	21
QT_c	corrected QT	97
RV	right ventricle	11
SA	sinoatrial	13
SGA	small for gestational age	2
SpI	sphericity index	3
T_a	amplitude of T-wave	98
T_{pe}	duration of the interval between the T-wave peak and its end ..	21
T_{pe,c}	corrected T _{pe}	97
T_{pe}/QT	ratio between T _{pe} and QT	21
VCG	vectorcardiogram	v
VTV	ventricular tissue volume	105
W	ventricular wall thickness	94
WT	wavelet transform	46

1.1 Framework of the Thesis

- 1.1.1 Motivation
- 1.1.2 Thesis goals
- 1.1.3 Thesis outline

1.2 Cardiac anatomy and function

1.3 Cardiac electrophysiology

- 1.3.1 Conduction system
- 1.3.2 Electrophysiological properties of myocardial cells
- 1.3.3 Spatial heterogeneities in depolarization and repolarization

1.4 Electrocardiogram and vectorcardiogram

- 1.4.1 Genesis of P, QRS and T waveforms, and their associated intervals

1.5 Intrauterine growth restriction and its cardiac impacts

- 1.5.1 Structural cardiac remodeling in IUGR
- 1.5.2 Electrophysiological changes in IUGR subjects

1.6 Biomarkers of cardiac electrophysiology

This chapter frames the thesis and introduces the fundamental principles of anatomy, function, and electrophysiology, emphasizing their relevance to the development of this study, from the ionic level to the organ level. Ventricular electrophysiological characteristics are thoroughly described. Furthermore, the chapter explores the features of intrauterine growth restriction in cardiac remodeling and its association with observed electrophysiological changes.

Additionally, it discusses the electrocardiogram and vectorcardiogram as diagnostic tools, along with the primary biomarkers that can be detected through these measurements.

1.1 Framework of the Thesis

1.1.1 Motivation

Cardiovascular diseases are among the leading causes of mortality worldwide, accounting for over 3 million deaths annually in Europe in 2023 [1]. In the United States, this figure reached 2 million annual deaths in 2019. In South America, the statistics vary by country; however, the Pan American Health Organization reported that in 2019, 28% of women and 43% of men were unaware of their hypertensive condition, a major cardiovascular risk factor [2].

In the 1980s, the hypothesis of the fetal origin of adult onset diseases was introduced, highlighting a potential relationship that brought significant considerations for public health, particularly in underdeveloped/developing countries, where the percentage of low-birth-weight neonates is six times higher than in developed nations [3]. During the current century, research on the fetal programming hypothesis has demonstrated that maternal malnutrition affects the fetal genome, causing permanent alterations in health [4]. In 2010, evidence showed that maternal malnutrition impacts placental and fetal development, leading to intrauterine growth restriction (IUGR), increased perinatal mortality, low-birth-weight neonates, and a higher risk of developing metabolic syndrome in adulthood [5].

Fetal growth in an unfavorable environment induces a state of malnutrition, with Doppler analysis revealing abnormal blood flow patterns. A neonate is considered small for gestational age (SGA) when birth weight is below the 10th percentile for gestational age or at least two standard deviations below the normal population. The incidence of IUGR in newborns may range between 3% and 7% of the total population [6], and approximately 30 million newborns are affected by IUGR globally each year. Overall, nearly 75% of all affected newborns are born in Asia, around 20% in Africa, other 5% in South America [3, 7], and a significant lower percentage in the rest of the Western world.

IUGR is currently recognized as a public health issue, as it represents one of the leading causes of perinatal mortality and morbidity. Neonatal morbidity includes asphyxia, meconium aspiration syndrome, persistent pulmonary hypertension, hypothermia, hypoglycemia, polycythemia, jaundice, feeding diffi-

culties, necrotizing enterocolitis, and sepsis. Long-term morbidity is associated with neurological disorders, cardiovascular diseases, and metabolic syndrome. Additionally, IUGR and preterm birth are linked to cardiovascular remodeling, which can manifest as a reduced sphericity index (SpI) of the heart (base-to-apex length/basal diameter).

Cardiac remodeling, characterized by structural and functional alterations in the myocardium, is a key factor in the development of cardiovascular diseases throughout life. Recent studies have shown that this phenomenon may have a congenital origin, associated with conditions such as IUGR, due to morphophysiological changes in cardiac mass, volume, and shape starting in the fetal stage. Individuals exposed to IUGR exhibit alterations such as a more spherical left ventricle (LV) and increased ventricular wall thickness, predisposing them to systolic and diastolic dysfunction at various life stages [8, 9]. Other electrophysiological abnormalities, such as prolonged depolarization and repolarization intervals, are associated with a higher risk of ventricular arrhythmias [10]. These findings underscore the importance of understanding the impact of cardiac remodeling as a consequence of IUGR, both in the development and persistence of cardiovascular pathologies into adulthood and in its role in the progression of related chronic diseases.

The degree of geometric remodeling is more pronounced in those born most prematurely. This was quantified using cardiac magnetic resonance imaging in infants, showing a higher weight-indexed left ventricular mass and greater end-diastolic volume in the IUGR cohort compared to term controls [11]. Additionally, variations in aortic wall thickness have been observed in term neonates with IUGR. The intima-media thickness was significantly greater in the IUGR group (810 μm in 25 neonates) compared to controls (743 μm in 25 neonates) [12].

Studies across different age groups have demonstrated the prevalence of anatomical changes in the cardiac muscle. In children, cardiovascular evaluations, including echocardiography and blood pressure measurements, have shown that cardiac changes persist from birth to six months of age [8]. In pre-adolescent patients, evidence obtained through echocardiography and three-dimensional heart shape analysis has indicated that cardiac remodeling persists, yielding results similar to those observed during childhood [13]. Subsequent studies on adults have corroborated the findings from studies in children and pre-adolescents. Using surface electrocardiography and generating vectorcardiograms, significant differences were observed in the angles between the dominant QRS depolarization vector and the T-wave repolarization vector in the XY plane between control patients and those diagnosed with IUGR.

This difference may play a key role in the cardiovascular risk of patients with IUGR [14, 15].

Experimental animal studies have explored the effects of fetal growth restriction, revealing morphophysiological cardiac alterations associated with adult diseases [16]. Various experimental approaches have been employed to alter the fetal environment, inducing conditions that mimic reduced efficiency in nutrient and oxygen exchange. Regardless of the specific method used, these models consistently result in common physiological consequences, many of which closely resemble those observed in human pathologies, such as reduced nephron number, impaired vascular function, and significant increases in blood pressure [17, 18].

Through computational simulations, it has become possible to integrate anatomical and physiological information at the organ level and simulate the propagation of action potentials, enabling the *in silico* representation of various pathological conditions. The use of an electrophysiological heart model, based on cellular and tissue-level frameworks and incorporated into realistic geometries derived from medical imaging, allows for the exploration of heterogeneity in action potentials, repolarization dispersion, and the mechanisms underlying the complex functioning of cardiac muscle.

The ability of these models to integrate electrical information from the cellular level to tissue behavior enables the simulation of electrocardiograms (ECGs) and the evaluation of biomarkers in the context of patients with IUGR. While previous studies have demonstrated significant anatomical and physiological impacts during neonatal and preadolescent stages, the relationship between geometric changes and cardiac electrophysiology remains a critical area requiring further investigation.

1.1.2 Thesis goals

The aim of this thesis is to characterize the electrophysiological parameters of the heart in preadolescents born with IUGR and their association with anatomical remodeling, through the analysis of ECG signals and biophysically-detailed computational models. To achieve this, several *in silico* experiments were conducted, simulating electrophysiological behaviour using realistic heart and torso models. Additionally, ECG parameters were measured in a cohort of IUGR and control subjects to evaluate depolarization and repolarization intervals, which were also analyzed *in silico*.

The research conducted and presented in this thesis was divided into the

following objectives:

- To develop a comprehensive computational framework for simulating normal 12-lead ECG traces within physiological ranges, incorporating a Purkinje-based conduction system tailored to each anatomical model.
- To derive anatomical models accounting for the anatomical changes observed in IUGR-preadolescents.
- To create a simulation framework for an electrophysiological heart model of an IUGR patient, enabling the characterization of ECG-based and anatomical parameters associated with cardiovascular risk.

Regarding the first objective, the Purkinje fibers were implemented in the model to simulate electrical stimulation, using a fractal projection method onto the endocardial tissue. This Purkinje network originated from the His bundle, incorporating varying diffusivity characteristics to reach the terminal nodes of the Purkinje network. A torso model was integrated with the heart to calculate the potentials that would be recorded using a virtual 12-lead ECG. The propagation model used was monodomain. The developed electrophysiological model and methodology enabled the creation of a finite element model for reaction-diffusion analysis, allowing the simulation of various scenarios by varying geometric parameters associated with cardiovascular remodeling.

To obtain normal T waves in agreement with clinical ranges, electrophysiological heterogeneities were introduced transmurally and along the apex-to-base direction. The biventricular model was divided into three sections: the apex section, mid-section, and base section. Each section was assigned a different G_{K_s} conductivity value to induce changes in the I_{K_s} current, enabling a detailed representation of repolarization dispersion.

For the second objective, IUGR-specific anatomical models were developed using a control ventricular model derived from medical imaging data. This involved applying cardiac remodeling parameters associated with IUGR, such as the sphericity index, apex-to-base length, and left ventricular thickness, as reported in the literature, to generate the anatomical models. These generated models will hereafter be referred to as globular cardiac models. The three-dimensional heart model differentiated the epicardium, myocardium, and endocardium tissues, and the direction of muscle fibers was assigned to each element of the tetrahedral mesh based on a rule-based method.

For the third objective, the impact of anatomical changes in the dominant vectors of the QRS, T-wave and QRS to T-wave was evaluated. Given that

inter-subject variability in the proportion of tissue division (endo, mid, and epi) affects repolarization, the effect of these changes on the direction of the dominant vectors of the QRS loop and the T-wave was analyzed.

Finally, we analyzed traditional ECG-based risk biomarkers, such as prolonged QRS complexes and T-wave durations, which were hypothesized to result from increased left ventricular wall thickness as a consequence of IUGR. To test this, the durations of the QRS complex, T-peak to T-end interval, QT interval, and Tpe/QT ratio were analyzed. This analysis was also performed on clinical data from a database of preadolescent control subjects and those with severe IUGR. The numerical simulation results were then compared with reported clinical findings to evaluate their statistical significance. Globular models were generated by varying the sphericity index and increasing left ventricular wall thickness, analyzing the impact of these changes on depolarization and repolarization dynamics.

1.1.3 Thesis outline

This document outlines the work and methodology developed during the doctoral research conducted in the Biomedical Engineering program at the University of Zaragoza and presents the findings of the thesis. The research aimed at characterizing the electrophysiological parameters of the heart of IUGR-born preadolescents and their association with anatomical remodeling, through the analysis of ECG signals and anatomically modified computational models. Previous studies have demonstrated anatomical and physiological impacts during neonatal and preadolescent stages; however, the relationship between geometric heart changes and cardiac electrophysiology requires further investigation. The findings of this research could contribute to evaluating the impacts of cardiac remodeling using ECG or vectorcardiogram (VCG) data and may also provide information on the effects of variations in sphericity index and thickness of the ventricular wall on ECG readings.

The structure of this Ph.D. thesis is organized into six chapters, detailing the research context, the methodology for generating computational models, and the measurement of the ECG interval resulting in depolarization and repolarization biomarkers related to cardiovascular risk. These analyzes are performed on clinical ECG signals and synthetic ECGs generated *in silico*.

- **Chapter 1:** This chapter frames the thesis and introduces the biological aspects of cardiac electrophysiology, including the anatomy and function of the heart, as well as the fundamental mechanisms underlying its

electrical activity. It covers the phases of the cardiac action potential, explaining the ionic events that occur during each phase, from rapid depolarization to the resting state. Additionally, the heterogeneity of ventricular tissue is discussed, highlighting the electrophysiological differences between the endocardium, mid-myocardium, and epicardium, with a particular focus on the variability in action potential duration among these layers. The chapter also includes a description of the ECG and VCG, emphasizing the key characteristics of depolarization and repolarization waves. After detailing the biological background, we incorporate a discussion on some collateral effects of IUGR on cardiac muscle, addressing both anatomical and physiological impacts. Finally, we describe the biomarkers identified in ECG and VCG associated with IUGR, as reported in the state of the art.

- **Chapter 2:** This chapter addresses several computational models proposed for simulating cardiac electrical activity, concluding with the characterization of the bidomain and monodomain models. Subsequently, the computational framework employed to solve a reaction-diffusion system using the finite element method is described. The chapter also details the biosignal processing tools used for applying linear transformations in principal component analysis to enable precise identification of QRS complexes and T-waves in virtual electrocardiographic signals. Finally, the calculation of the VCG from the synthetic ECG is described using the inverse Dower matrix, highlighting its importance for the interpretation of cardiac electrical biomarkers.
- **Chapter 3:** This chapter describes the methodology used to evaluate the relationship between morphological remodeling and the angular variation of QRS and T-wave dominant vectors. This was achieved using computational models based on realistic heart and torso geometries, in which IUGR-induced morphological changes were incorporated by reducing the ventricular sphericity index. Starting from a control model, we developed eight different globular heart models (\mathcal{G}_A a \mathcal{G}_H) by shortening the base-to-apex length and increasing the basal ventricular diameter. The aim of this chapter was to simulate the geometric cardiac changes resulting from IUGR and compare them with reported clinical findings.

We computed QRS and T-wave dominant vectors and their angles from simulated pseudo ECG and compared these with clinical measurements. By additionally varying the position of the ventricles relative to the torso and electrodes, we observed that electrode displacement could signifi-

cantly impact the calculated angles and should be considered when interpreting the results. The simulation-based findings suggest a connection between QRS-T angles and altered heart morphology, highlighting a potential non-invasive approach for assessing cardiac remodeling.

The following publications presented the results obtained in this chapter:

- **Bueno-Palomeque, F.L.**, Mountris, K.A., Mincholé, A., Ortigosa, N., Bailón, R., Pueyo, E. and Laguna, P., “Changes in QRS and T-wave Loops Subsequent to an Increase in Left Ventricle Globularity as in Intrauterine Growth Restriction: a Simulation Study”, 2020 Computing in Cardiology, Rimini, Italy, 2020, pp. 1-4, doi: 10.22489/CinC.2020.438.
 - **Bueno-Palomeque, F.L.**, Mountris, K.A., Mincholé, A., Ortigosa, N., Bailón, R., Pueyo, E. and Laguna, P., “Variación del ángulo entre QRS y onda T del ECG en función del índice de esfericidad ventricular en sujetos con crecimiento intrauterino retardado: un estudio computacional.” Jornada de Jóvenes Investigadores del I3A 10 (2022).
 - **Bueno-Palomeque, F.L.**, Mountris, K.A., Ortigosa, N., Bailón, R., Bijmens, B., Crispi, F., Pueyo, E., Mincholé, A., and Laguna, P., “QRS-T Angles as Markers for Heart Sphericity in Subjects With Intrauterine Growth Restriction: A Simulation Study,” in IEEE Journal of Biomedical and Health Informatics, vol. 27, no. 10, pp. 4707-4718, Oct. 2023, doi: 10.1109/JBHI.2023.3297550.
- **Chapter 4:** This chapter describes how increased globularity and wall thickness resulting from IUGR in preadolescents affects the QRS width, T-peak to T-end and QT intervals, all biomarkers associated with susceptibility to ventricular arrhythmia. The results revealed significant differences in several biomarkers, providing evidence of electrophysiological changes caused by cardiac remodeling in preadolescents. The IUGR subjects showed significantly wider QRS (4 ms), longer T_{pe} intervals (2 ms), and higher ratio between T_{pe} and QT (3%) as compared to control group.

The following publication summarized the results obtained in this chapter:

- **Bueno-Palomeque, F.L.**, Mountris, K.A., Ortigosa, N., Bailón, R., Bijmens, B., Crispi, F., Pueyo, E., Mincholé, A., and Laguna, P.,

“QRS Width and T-Peak to T-End Interval Are Prolonged in Preadolescents with Severe Intrauterine Growth Restriction at Birth when Compared to Controls,” 2023 Computing in Cardiology (CinC), Atlanta, GA, USA, 2023, pp. 1-4, doi: 10.22489/CinC.2023.344.

- **Chapter 5:** This chapter describes the various electrophysiological *in silico* simulations conducted using eight different globular models (\mathcal{G}_1 a \mathcal{G}_8) derived from a reference control model. These models reflected the anatomical cardiac changes resulting from IUGR and assessed their impact on depolarization and repolarization intervals.

Measurements on the *in silico* PCA transformed leads showed an increase in QRS width, R amplitude, and in T_{pe} interval in the globular models, consistent with clinical data measured in the chapter 4. Despite the increase in QRS width, the QT interval increases but in a way not linearly related to ventricular wall thickness change.

These findings suggest that cardiac remodeling primarily influences the depolarization cycle, notably QRS width, while repolarization intervals increases but not directly related to the left ventricular wall thickness increase. The study contributes to a deeper understanding of the impact of geometric and volumetric changes in IUGR-related cardiac remodeling, also emphasizing the need for further research introducing electrophysiological remodeling, additional to the anatomical/geometrical one here considered, and their impact on cardiac function.

The following publications presented the results obtained in this chapter:

- **Bueno-Palomeque, F.L.**, Zacur, E., Pueyo, E., Crispi, F., Laguna, P. and Mincholé, A., “Implications of IUGR-Related Geometric Heart Changes on the ECG and Electrophysiology: an In silico Perspective.” 2024 Computing in Cardiology (CinC), Karlsruhe, Germany, 2024, pp. 1-4, doi: 10.22489/CinC.2024.462.
 - **Bueno-Palomeque, F.L.**, Zacur, E., Pueyo, E., Crispi, F., Laguna, P. and Mincholé, A., “Electrophysiological Characterization of Preadolescents Born with Intrauterine Growth Restriction: Insights from Clinical and Computational Data”, Journal of Physiology, doi: 10.1113/JP288197.
- **Chapter 6:** This chapter summarizes the main findings of this research, the conclusions drawn, and the limitations encountered during this study, which was part of the doctoral program in biomedical engineering. The

findings are discussed in the context of the current state of the art, and guidelines for future work are proposed.

1.2 Cardiac anatomy and function

The heart is the primary organ of the cardiovascular system, responsible for continuously distributing blood throughout the body. In this process, the heart supplies oxygen and nutrients while removing metabolic waste products generated by various biological processes.

The heart has four chambers: two upper chambers (atria) and two lower chambers (ventricles). The right atrium receives blood from three vessels: the superior vena cava, the inferior vena cava, and the coronary sinus. Blood flows from the right atrium to the right ventricle (RV) through the tricuspid (or right atrioventricular) valve. The RV contains internal ridges formed by bundles of muscle fibers called trabeculae carneae, some of which are part of the heart's conduction system. The RV is separated from the LV by the interventricular septum. Blood from the RV flows through the pulmonary valve into the pulmonary trunk, which divides into the right and left pulmonary arteries that carry blood to the lungs (Fig. 1.1) [19].

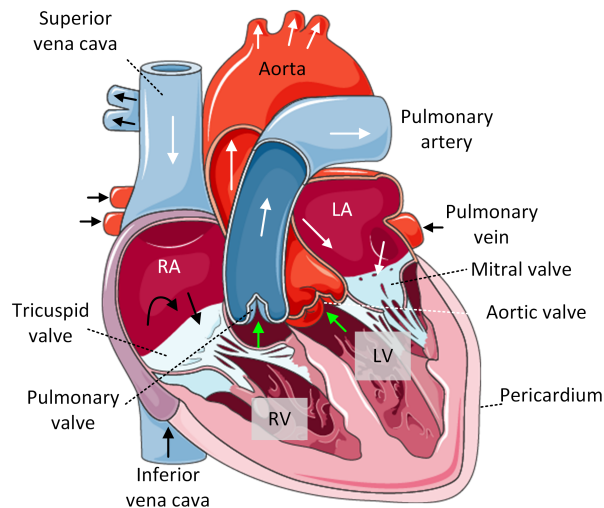


Figure 1.1: Longitudinal view of the heart, showing the chambers and the valve system for their connection. Regions marked in red represent the chambers and the system responsible for the conduction of oxygenated blood throughout the body. Blue regions correspond to the circulation of deoxygenated blood to the lungs for reoxygenation. Adapted from <https://smart.servier.com/>

On the other side, the left atrium receives blood from the lungs via four pulmonary veins. Blood flows from the left atrium to the LV through the

bicuspid (or mitral) valve. The LV, which has the thickest wall of the four chambers, forms the apex of the heart. Blood flows from this chamber through the aortic valve into the ascending and descending aorta. When a heart chamber contracts, it ejects a volume of blood into a ventricle or an artery. The valves open and close in response to pressure changes that occur during the cardiac cycle of contraction and relaxation. Valves are unidirectional, opening to allow blood flow and closing to prevent backflow.

The heart rests on the diaphragm, with approximately two-thirds of its mass located to the left of the body's midline (the line that divides the body into right and left sides). The heart has a conical shape; its apex is formed by the LV and points anteriorly, inferiorly, and to the left. The base of the heart, opposite to the apex, forms the posterior surface and is composed mainly of the atria, predominantly the left atrium.

The heart is enclosed by a membrane called the pericardium, which holds it in position while allowing freedom of movement for contraction. The pericardium is divided into two layers: the fibrous pericardium, made of dense connective tissue, which prevents excessive stretching of the heart; and the serous pericardium, a deeper layer that forms a double membrane around the heart (Fig. 1.2) [19].

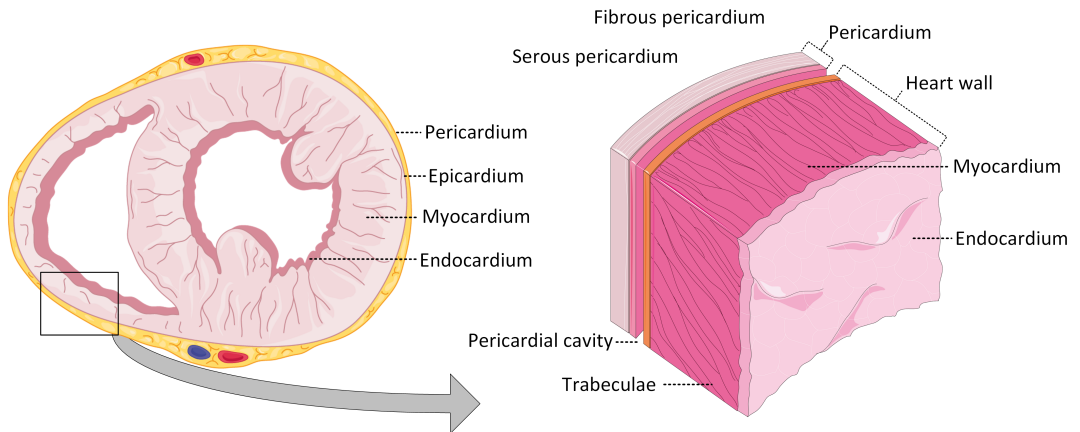


Figure 1.2: Pericardium and heart wall with their divisions. Adapted from <https://smart.servier.com/>

The heart wall, composed of three main layers, the epicardial tissue (epi), mid-myocardial tissue (mid), and endocardial tissue (endo), plays a critical role in its functionality. In particular, the myocardium, formed by specialized muscle tissue, enables the rhythmic and synchronized contractions of the

heart, driven by an intrinsic electrical conduction system. This anatomical architecture, combined with the mechanical and electrical properties of the heart, ensures efficient circulation while adapting to the body's metabolic demands.

The endo tissue is the innermost layer of the heart, lining the cardiac chambers and valves. It is primarily composed of endothelial tissue and serves as a barrier that facilitates smooth blood flow without friction. At the center of the heart wall lies the mid tissue, the muscular layer responsible for the rhythmic contractions that pump blood. This layer is formed by specialized muscle fibers that enable synchronized and efficient contractions. The myocardial muscle fibers are wrapped and surrounded by connective tissue made up of endomysium and perimysium. These cardiac muscle fibers are organized into bundles that run diagonally around the heart, facilitating blood ejection. Cardiac muscle is a striated, involuntary muscle. Finally, the epi tissue, the outermost layer, is composed of connective tissue and a thin layer of mesothelial cells. In addition to serving as a protective layer, the epicardium is part of the pericardium, the membranous sac that surrounds the heart. The epicardium contains blood vessels, lymphatic vessels, and nerves that supply the myocardium. These three layers not only have distinct structures but also function in coordination, which is essential for the proper performance of the organ.

1.3 Cardiac electrophysiology

1.3.1 Conduction system

The electrical function of the heart is carried out by a specialized conduction system that ensures the generation and propagation of electrical impulses necessary for the synchronized contraction of the myocardium. This system begins with the sinoatrial (SA) node, located in the right atrium, which serves as the primary pacemaker by generating spontaneous action potential (AP) through automatic cells. Electrical impulses propagate from the SA node to the atria, inducing their contraction, and reach the atrioventricular (AV) node. Here, a critical delay occurs to allow ventricular filling before contraction. From the AV node, the electrical stimulus is transmitted to the bundle of His and then to the Purkinje fibers, which distribute the AP rapidly and uniformly throughout the ventricles (Fig. 1.3). This process is facilitated by low-resistance connections in the intercalated discs, such as gap junctions, which enable rapid cellular depolarization. The pattern of electrical activation, combined with

the electrophysiological properties of the different myocardial layers, results in coordinated movements that optimize the efficient pumping of blood into the systemic and pulmonary circulation.

The Purkinje fibers are distinguished by their capacity to transmit electrical impulses at velocities ranging from 1.5 to 4.0 meters per second [20]. This rapid conduction is attributed to their large diameter and the abundance of gap junctions in the intercalated discs. Due to this high conduction velocity (CV) and the distribution of Purkinje fibers, excitation reaches the contractile myocardium of both ventricles almost simultaneously.

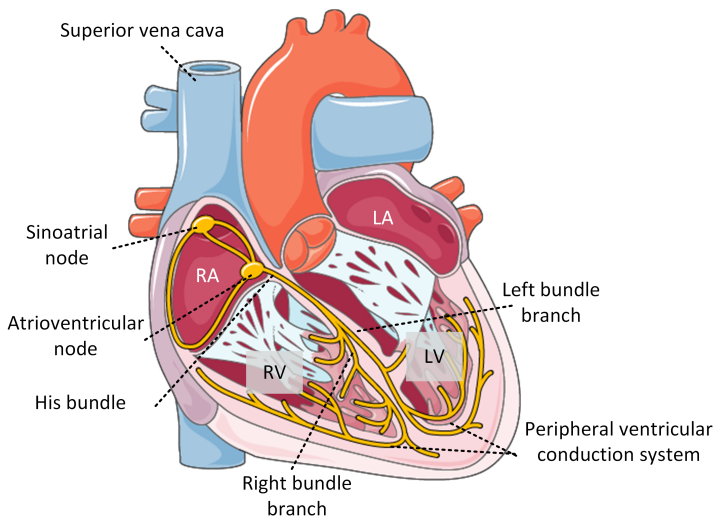


Figure 1.3: This figure presents a longitudinal section of the heart, highlighting the cardiac conduction system. Adapted from <https://smart.servier.com/>

The direction of the myocardial fibers is organized in a unique helical arrangement that varies across the layers of the myocardial wall. In the endocardial layer, the fibers are predominantly oriented longitudinally (+60 degrees), while in the midmyocardial tissue, the fibers adopt a circumferential orientation. In the epicardial layer, the fibers revert to a longitudinal orientation but in the opposite direction to the endo (-60 degrees) [21]. This helical pattern allows for coordinated contraction and relaxation of the myocardium, facilitating a torsional motion that enhances the efficiency of blood ejection. During systole, the counterclockwise rotation of the ventricular base and the clockwise rotation of the apex produce a “twisting” effect that improves ventricular ejection. During diastole, this motion is reversed, favoring ventricular filling. This arrangement not only optimizes the mechanical performance of the heart

but also evenly distributes stress and minimizes energy expenditure during the cardiac cycle.

1.3.2 Electrophysiological properties of myocardial cells

The electrical potential difference between the inner and outer of a cell varies depending on the cell type and its specialized properties of the cell membrane that separates these two environments. The presence of dominant ions in the intracellular and extracellular fluids makes it a conductive medium. Sodium (Na^+), potassium (K^+), and chloride (Cl^-) are fundamental in neural cells, while calcium (Ca^{2+}) is a more important element in cardiac muscle cells [22, 23]. Among the active characteristics of the membrane are integral proteins that function as pumps, using energy to transport ions across the membrane against a concentration gradient, an electrical gradient, or both. The sodium-potassium pump moves sodium ions out of the intracellular space and bringing potassium ions in. Other proteins function as channels, opening or closing pathways through the membrane at different times. While the pump establishes the concentration differences that allow certain events to occur, the channels utilize this energy to create rapid voltage changes and small, intense loops of current that form the signaling system through nerves to muscles [24].

Over a period of time, ion channels, exchangers and ion pumps cause different concentrations of ions to accumulate inside and outside a cell. A transmembrane voltage is generated because there is a difference in concentration across the membrane. In a steady state, the transmembrane potential for a system involving the four main ions species can be modeled using the equation:

$$V_m = \frac{g_K}{g_m} V_K + \frac{g_{Na}}{g_m} V_{Na} + \frac{g_{Ca}}{g_m} V_{Ca} + \frac{g_{Cl}}{g_m} V_{Cl}, \quad (1.1)$$

where V_m is the membrane potential in mV, g_i is the i -th ionic specie channel conductivity, $i \in \{K^+, Na^+, Ca^{2+}, Cl^-\}$, $g_m = \sum_{i=1}^4 g_i$ is the sum of all the conductivities, and V_i the i -th ionic specie equilibrium potential given by the Nernst equilibrium equation:

$$V_i = \frac{R T}{z_i F} \ln \left(\frac{[\eta_i]_{out}}{[\eta_i]_{in}} \right), \quad (1.2)$$

where R is the universal gas constant, T is the absolute temperature in ($^{\circ}\text{K}$), F is the Faraday constant, z_i is the valence of i -th specie ion, $[\eta_i]_{out}$ and $[\eta_i]_{in}$ are the extracellular and intracellular concentrations, respectively, of i -th ions.

The effects of the diffusion gradient and the potential gradient are nearly equal and opposite when the intracellular potential is -90mV relative to the extracellular potential, resulting in a steady state.

Membranes generate AP by changing their permeability to specific ions, such as sodium and potassium. An AP lasts approximately 400 ms. In the cardiac conduction system, an AP begins with a resting voltage near -90 mV , followed by an excitation phase where membrane permeability changes, and the voltage rapidly rises. After reaching a peak of about $+20\text{ mV}$, the potential is maintained at a plateau close to 0 mV for approximately 300 ms, after which it returns to its resting state. This sequence of five well-defined phases, that ensure the synchronized contraction and relaxation of the myocardium, are listed and represented in the Fig. 1.4.

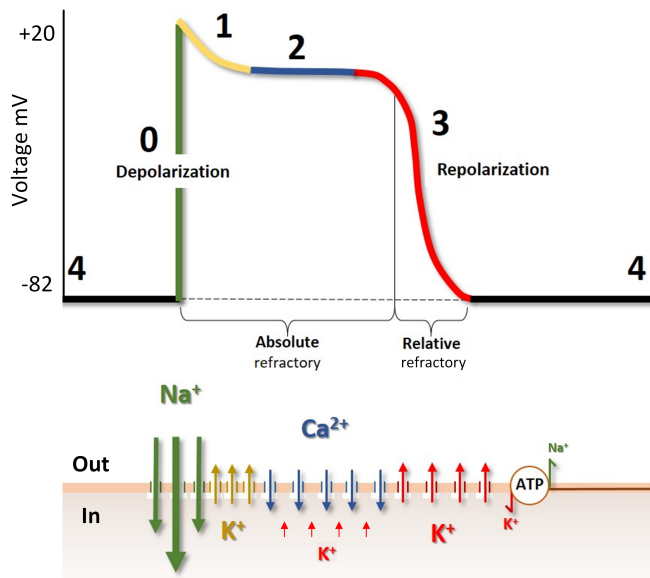


Figure 1.4: Diagram of the ventricular cell AP and the ionic exchange involved in its generation. Adapted from <https://smart.servier.com/>.

- Phase 0 - Rapid Depolarization: This phase begins with the opening of fast Na^+ channels, allowing a massive influx of sodium ions into the cell. This positive flow generates an abrupt increase in the membrane potential, reaching values near $+20\text{ mV}$. This rapid change is crucial for activating the action potential and triggering myocardial contraction.
- Phase 1 - Initial Repolarization: Following depolarization, the fast Na^+

channels inactivate, and transient potassium (I_{to}) channels open, allowing a brief efflux of K^+ out of the cell. This generates a slight drop in membrane potential, initiating the repolarization process.

- Phase 2 - Plateau: Sustained calcium (Ca^{2+}) influx through L-type calcium channels counteracts potassium efflux, maintaining a stable membrane potential around 0 mV. This prolonged equilibrium ensures sustained myocardial contraction, which is essential for the effective pumping of blood from the cardiac chambers to the circulation.
- Phase 3 - Complete Repolarization: During this phase, L-type calcium channels gradually inactivate, while delayed rectifier potassium channels (I_{Kr} and I_{Ks}) become increasingly active, facilitating potassium efflux and restoring the membrane potential to negative values. This process returns the cell to its basal electrical state, concluding the action potential.
- Phase 4 - Resting State: In the final phase, the membrane potential remains stable at approximately -90 mV, maintained by the sodium-potassium pump (Na^+/K^+ ATPase), which restores ionic gradients by expelling sodium and reintroducing potassium, and by the sodium-calcium exchanger (Na^+/Ca^{2+}), which regulates intracellular calcium levels. This resting state prepares the cardiac cell to initiate a new depolarization cycle.

Quantifying the electrophysiological properties of the cardiac AP is crucial for evaluating myocardial function and identifying potential abnormalities. Among the key parameters is the action potential duration (APD), which represents the time elapsed from the onset of depolarization to the end of repolarization, measured at different percentages of repolarization (APD_{50} , APD_{90}). This parameter reflects the cell's ability to sustain contraction and is influenced by ion channel activity. Another critical metric is the effective refractory period, corresponding to the interval during which a cell cannot be re-excited, ensuring synchronization and preventing arrhythmias. The post-refractory recovery measures the time required for cells to fully regain excitability after the effective refractory period, which is relevant for analyzing susceptibility to disorganized rhythms. Lastly, the CV quantifies the speed at which electrical impulses propagate through cardiac tissue, depending on cellular connectivity and myocardial electrophysiological properties.

1.3.3 Spatial heterogeneities in depolarization and repolarization

Human ventricular tissue is highly heterogeneous, both functionally and structurally, with significant differences between the endo, mid, and epi tissue. The endo tissue, in direct contact with the bloodstream, contains fibers oriented for efficient conduction and demonstrates a reduced response to rapid electrical stimuli, adapting to its role in initiating ventricular contraction [25]. The epi tissue, located on the heart's outer surface, is composed of fibers with a higher density of K^+ channels, enabling faster repolarization. The mid tissue, situated between these two layers, has been reported a longer APD [26].

The APD varies significantly among these tissues due to differences in ion channel expression and functionality. In the endo, the APD is typically longer because of reduced activity of delayed rectifier K^+ channels, which slows repolarization. In contrast, the epi tissue exhibits a shorter APD due to a higher density of I_{to} channels, which promotes earlier repolarization. The mid tissue, characterized by a high concentration of M cells, shows a longer APD and develop early afterdepolarizations in response to blockers of the rapidly activating delayed rectifier potassium current (I_{Kr}), whereas epicardial and endocardial cells are generally less likely to do so [26, 27]. This variation in APD across ventricular layers creates a repolarization gradient that plays an important role in coordinating ventricular contraction.

The heterogeneity of APD among ventricular layers has significant clinical implications, particularly in arrhythmia susceptibility. The repolarization gradient between the endo, mid, and epi can act as a trigger for reentry, a common mechanism in ventricular arrhythmias [28, 29]. Additionally, under pathological conditions such as ischemia or ventricular hypertrophy, this heterogeneity may be exacerbated, increasing the risk of severe arrhythmic events. Understanding the role of these electrophysiological variations among ventricular layers is essential not only for developing therapeutic strategies but also for risk stratification. Computational models that accurately simulate cardiac electrical activity across various health and disease states may help deepen our understanding of this role.

1.4 Electrocardiogram and vectorcardiogram

The heart's electrical activity and its variations over time propagate through the body due to its conductive properties. As a result, measurements through electrodes placed on the torso's skin taken outside the cells will provide a

superposition of contributions from the APs generated by the muscle fibers propagated throughout the body. The recording of the heart's electrical activity during the cardiac cycle is done through an ECG. The series of waveforms recorded via electrodes placed on the body's surface -along with their shape, duration, and patterns- provide information that has become a fundamental tool in diagnosing heart diseases. The importance of the ECG has been further strengthened by the use of computational tools that allow for the analysis of subtle variations in ECG signals and the ability to process large amounts of data relatively quickly.

ECG signals are recorded from various locations on the body to provide a three-dimensional representation of the heart's electrical activity. The standard 12-lead ECG system consists of 12 leads derived from 10 electrodes, which include six limb leads (I, II, III, aVR, aVL, aVF) and six chest leads (V1 to V6). Fig. 1.5 illustrates the three-dimensional orientation of these 12 standard leads within the XYZ-coordinate system.

A VCG represents both the spatial and temporal information of cardiac activity. The depolarization and repolarization loops can have clinical relevance in detecting cardiac conditions such as myocardial infarction or myocardial injury during coronary surgery, features that are not easily observable in a standard ECG signal. Spatial VCG signals have been shown not only to facilitate a basic understanding of the electrical phenomena associated with cardiac function, but also to reveal pathological features that are difficult to detect in an ECG [30].

The information provided by the VCG complements the ECG in the analysis of acute myocardial infarctions and allows for a more detailed evaluation of the association between conduction blocks and chamber hypertrophies. VCG has been demonstrated to be a valuable tool in identifying conditions such as right ventricular hypertrophy, lateral infarction, ventricular pre-excitation syndrome, and Brugada syndrome [31], among other pathologies [32]. The simultaneous analysis of ECG and VCG has also proven to be an important tool for diagnosing certain cardiac pathologies [33], through what is known as electrovectorcardiography.

The Frank lead system is a vectorcardiographic approach designed to capture the three-dimensional electrical activity of the heart more accurately than the standard ECG system [34]. It employs a set of orthogonal leads, typically labeled as XYZ, to directly measure the heart's electrical vectors along three mutually perpendicular axes (see Fig. 1.5). These leads provide a more precise spatial representation of cardiac electrical activity by minimizing projection

distortions seen in the standard ECG.

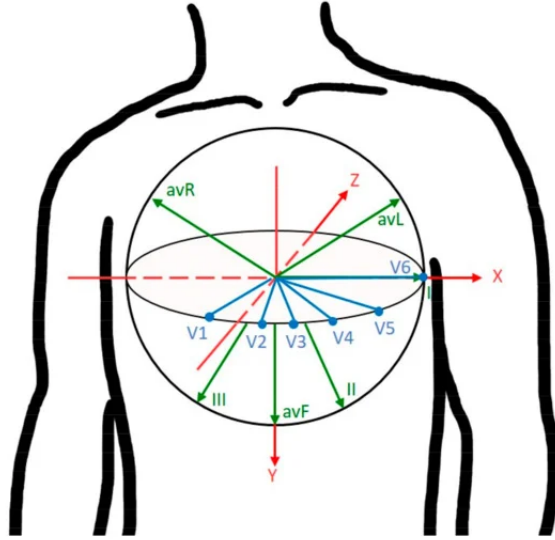


Figure 1.5: The three-dimensional view of 12 ECG leads on the xyz-coordinate axis system. Adapted from [35] <https://www.mdpi.com/1424-8220/20/24/7246>.

Linear mathematical transformations such as Dower or Kors [36–38], can be applied to the standard 12-lead ECG to project the electrical signals into a three-dimensional space, thereby synthesizing the VCG or XYZ components of cardiac electrical activity. These synthesized XYZ leads aim to replicate the orthogonal views provided by systems like the Frank lead configuration. Dower conducted his research based on the torso models developed by Frank and introduced a linear transformation matrix to derive a 3-lead VCG from the standard 12-lead ECG. This transformation was shown to preserve clinically relevant information related to the heart’s electrical dynamics [30].

The Kors/Dower transformations derive the VCG from the recorded leads $x_{l_i}(n)$ where $l_i = V1, V2, V3, V4, V5, V6, I, II$ leads, based on equation 1.3.

$$\begin{bmatrix} x_{\text{VCG}}(n) \\ y_{\text{VCG}}(n) \\ z_{\text{VCG}}(n) \end{bmatrix} = \begin{bmatrix} a_{11} & a_{12} & \dots & a_{1m} \\ a_{21} & a_{22} & \dots & a_{2m} \\ a_{31} & a_{32} & \dots & a_{3m} \end{bmatrix}^{-1} \cdot \begin{bmatrix} x_{l_1}(n) \\ x_{l_2}(n) \\ \vdots \\ x_{l_m}(n) \end{bmatrix}, \quad (1.3)$$

where $x_{\text{VCG}}(n), y_{\text{VCG}}(n), z_{\text{VCG}}(n)$ are the components of the VCG along the XYZ axes, $x_{l_1}(n), x_{l_2}(n), \dots, x_{l_m}(n)$ are the ECG signals from the standard

12-lead ECG (V1 to V6, I, and II leads) and a_{ij} are the elements of the transformation matrix that relates the VCG signals to the ECG signals. In this way, by applying the inverse matrix in (1.3), an equivalent VCG can be obtained from an ECG recording.

The set of cardiac cells that depolarize at a given moment in time can be represented as a dipole, which can be associated with a vector whose position, direction, and magnitude describe the behavior of the dipole over time. The sum of all the vectors can be represented as a dominant vector that describes the direction of the electrical impulse during the depolarization and repolarization phases in a three-dimensional plane. This vector can be visualized through a VCG.

1.4.1 Genesis of P, QRS and T waveforms, and their associated intervals

An ECG signal presents several important waves and intervals that are critical for clinical analysis, and detecting these has been a key area of development in biosignal processing. The names and intervals of the ECG in humans are exemplified in Fig. 1.6. Atrial depolarization is identified by the P wave, while ventricular depolarization is represented by the QRS complex, and the T-wave reflects the ventricular repolarization phase. Atrial repolarization is difficult to determine, as it coincides largely with the QRS complex. The QRS complex encompasses the depolarization process of both ventricles, and its duration can range from 70 to 110 ms. The amplitude during this phase can reach 2-3 mV.

From the standard 12-lead ECG, the QRS duration (QRS_d) is a characteristic associated with morphophysiological abnormalities and serves as a predictor of congestive heart failure [39], an incident of atrial fibrillation [40], and death. The RR interval represents the length of a cardiac cycle and is measured between two successive R peaks.

The T-wave is generated by ventricular repolarization and can last around 300 ms. The duration of the interval between the T-wave peak and its end (T_{pe}) is a parameter also measured to analyze the dispersion of repolarization. The QT interval represents the time from the onset of ventricular depolarization to the complete ventricular repolarization. Since this parameter varies with heart rate, it is important to correct it to have biomarkers heart rate independent.

During the repolarization phase, the QT and T_{pe} intervals have been identified as predictors of ventricular arrhythmias in severe cardiac conditions [41]. The ratio between T_{pe} and QT (T_{pe}/QT) shows the relationship between the dispersion of repolarization relative to ventricular APD and is considered an

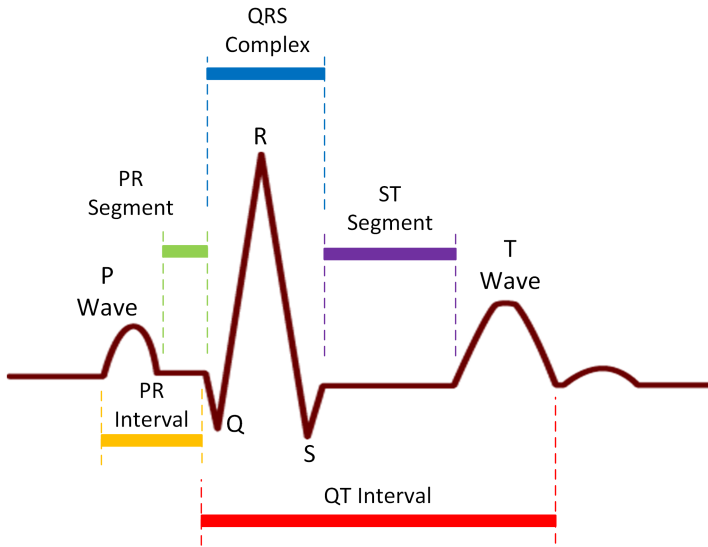


Figure 1.6: Diagram of an ECG with representative markers at different stages of the cardiac cycle: the P wave corresponding to atrial depolarization, the QRS complex corresponding to ventricular contraction, and the T-wave corresponding to repolarization.

index of arrhythmogenesis [42].

1.5 Intrauterine growth restriction and its cardiac impacts

Cardiac remodeling is widely recognized as a major contributor to cardiovascular disease. Anatomical and physiological changes such as alterations in size, geometry, and function, can result from cardiac injury or be triggered by various factors, including ischemia/reperfusion, pressure and volume overload, genetic predisposition, IUGR, or neuroendocrine activation, among other causes [43]. When cardiac remodeling occurs as a result of IUGR, it is often referred to as fetal programming [44]. Although the connection between cardiac remodeling and myocardial dysfunction is well-established, the underlying progression of this phenomenon remains incompletely understood. Consequently, recent research has increasingly focused on the potential influence of the fetal environment on the development of adult diseases.

Cardiac adaptation, as a compensatory strategy to respond to an inadequate growth environment, is expected to reverse once the initial stressor is removed. However, in some cases, cardiac remodeling persists into adulthood.

IUGR affects 7-10% of all pregnancies, with a higher incidence in underdeveloped or developing countries [45]. There is substantial evidence linking intrauterine development with adult-onset cardiac diseases [46]. IUGR is associated with adult obesity and increased risk of death from cardiovascular diseases and stroke. Animal models studying fetal growth have also shown that this condition leads to permanent alterations in cardiac morphophysiology, which are connected to diseases later in life. Various experimental methods have been applied to alter the fetal environment to simulate less efficient growth conditions. Regardless of the method used, common consequences such as a reduced nephron number, impaired vascular function, and significant increases in blood pressure, can often be observed, resembling conditions seen in humans [16].

1.5.1 Structural cardiac remodeling in IUGR

Altin et al. [10] demonstrated that systolic and diastolic functions are altered in infants born SGA with mild growth retardation, and these alterations differ during the first six months of life. Further evidence supporting the occurrence of primary cardiac remodeling during the fetal stage, which continues into infancy (up to six months of corrected age), is presented by Cruz Lemini et al. [8]. Their study utilized echocardiography and blood pressure measurements in a cohort of 80 SGA fetuses and 80 control fetuses, reinforcing the idea that cardiac changes begin in utero and persist postnatally.

Another study, conducted with a cohort of 58 IUGR children and 94 controls, provides evidence that cardiac remodeling persists until preadolescence, showing similar characteristics to those observed in the prenatal stage and early childhood. The study confirmed the presence of a spherical ventricle and reduced longitudinal motion, using 2D and 3D echocardiography, along with blood pressure and/or ECG measurements (see Fig. 1.7) [13].

Additionally, children with IUGR exhibited a higher prevalence of post-systolic shortening in the LV, particularly in the septal and lateral walls, which is associated with pressure overload and generates increased stress on the septum. A large study involving nearly 150 000 adolescents, reported by Nilsson [47], demonstrated that systolic blood pressure is inversely correlated with birth weight, with lower birth weights linked to higher blood pressure. This finding further supports the concept of fetal programming and its long-term effects into adolescence.

On the other hand, Arnot et al., [48] in a study with a cohort of 784 young adults (aged 34-49 years, all born at term and followed since birth), reported that while adults who were SGA at birth exhibit cardiac changes in geometry

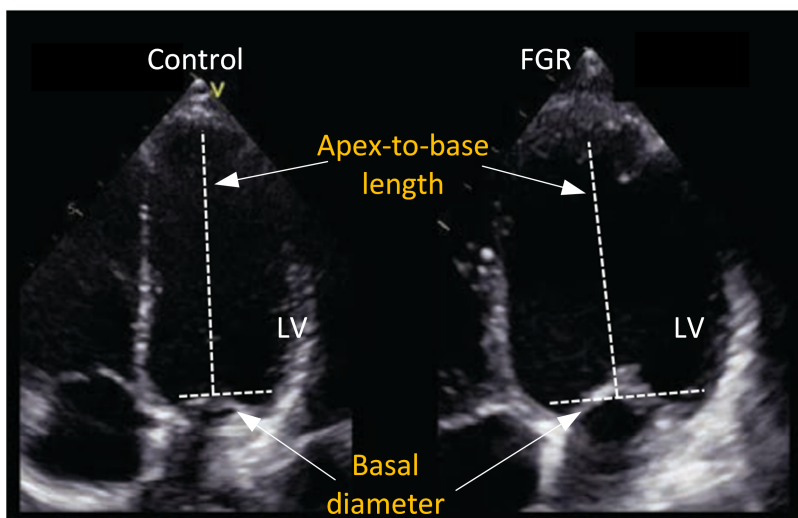


Figure 1.7: 2D echocardiographic image showing the four heart chambers at the end of diastole, comparing a control subject and a subject with fetal growth restriction (FGR). The apex-to-base length and basal diameter are indicated, highlighting the more spherical shape of the heart in the FGR subject. The control heart appears more elongated in contrast. Image edited from [13]

and function similar to those observed in SGA children and adolescents, only subtle alterations in cardiac anatomy and physiology are evident compared to individuals born at a normal weight or appropriate for gestational age (AGA). This analysis was conducted using 2D transthoracic echocardiograms.

Birth weight and its relationship with vascular function may stem from reprogramming during the fetal stage. Studies have demonstrated a link between low birth weight and impaired endothelium-dependent dilation, both in childhood and in individuals aged 20 to 30. However, the impact of this relationship diminishes progressively in the presence of an increased cardiovascular risk [49].

Several studies have shown that the effects of IUGR can persist during the early years after birth. However, the literature review revealed a lack of studies linking the postnatal environment experienced by individuals born with this condition to the persistence of cardiac remodeling. It is evident that the postnatal developmental environment of infants influences growth, just as it did during the fetal stage. Factors such as postnatal nutrition, parental socioeconomic status, and the social environment significantly affect the overall development of the individual [45]. On the other hand, regarding final height,

the study by Legger et al. found that the ultimate stature and individual height gain of children with IUGR are influenced by maternal and paternal height as well as birth length, while discarding other variables such as pregnancy-related risk factors associated with IUGR [50].

1.5.2 Electrophysiological changes in IUGR subjects

Cardiac remodeling is present with preterm birth, leading to changes in ventricular mass, volume, and shape, particularly in the LV. The extent of geometric remodeling is more pronounced in those born extremely preterm. Using cardiac magnetic resonance imaging, Cox et al. [11] studied 34 preterm infants and 10 term controls, finding a higher weight-indexed LV mass and greater end-diastolic volume compared to the term controls. Echocardiography in IUGR newborns also revealed a more globular heart with a reduced apex-base length (L), likely an adaptation to manage pressure and volume overload.

Changes in pressure and volume are associated with a more globular heart shape, dilated atria, and thicker myocardial walls, primarily due to hypoxia and elevated placental resistance during the fetal stage, as seen in IUGR cases [8]. The SGA group demonstrated a more globular cardiac shape, with a lower left SpI: 2.06 in controls vs. 1.87 in SGA prenatally, and 1.92 vs. 1.67 postnatally, as well as signs of systolic longitudinal dysfunction.

The effects of cardiac remodeling are evident in the depolarization and repolarization processes. Previous studies on ECG signals from adults who experienced IUGR have shown that the angle between the dominant vectors of the QRS and T waves is significantly different from that in control individuals. This may reflect the cardiovascular electrophysiological remodeling that follows IUGR and preterm birth into adolescence [14]. In a cohort of adults, there is further evidence of ECG differences, with statistically significant differences in the angle between the dominant vector of the QRS loop and the dominant vector of the T-wave in the frontal plane [15].

In the fetal stage, QRS_d measurements have been shown to be two standard deviations below the normal value when comparing an IUGR group (26 pregnant women) with AGA fetuses. These measurements were taken from ECG recordings on the maternal surface within 10 days before delivery [51]. Similar results were found by Pardi [52], where 54 of 68 fetuses were classified as IUGR, and of these, 44 showed QRS_d below two standard deviations from the mean normal value for their gestational age.

In contrast to these findings, Grimm et al. [53] compared the intervals

using fetal magnetocardiography (fMCG) in a group of 30 IUGR and 60 control subjects, finding a non-significant increase in QRS_d . Similarly, Van Leeuwen et al. [54] found significantly longer QRS_d in an IUGR group, measured through fMCG. Additionally, Velayo et al., [55] found no significant difference in QRS_d between the IUGR group (15 subjects) and controls (20 subjects), though a significant prolongation of the QT interval was observed in the IUGR group, measured through transabdominal fetal ECG.

Variations in the repolarization segment have also been observed in neonates, reflected in greater QT and JT dispersion in the IUGR group [56], further strengthening the link between IUGR and electrophysiological remodeling. Changes in T-wave morphology are associated with the action potential of different transmural layers during repolarization [57]. Considering the geometric changes in the basal diameter (ϕ), which widen the ventricular wall, these changes could potentially affect the morphology of the T-wave and the QRS complex.

While these markers (QRS_d , QT, and T_{pe}) have shown a correlation with IUGR subjects, the relationship between geometric remodeling and its impact on their variation is not yet clearly understood. It has been suggested to further investigate their role in distinguishing between IUGR and AGA individuals [58].

1.6 Biomarkers of cardiac electrophysiology

Among the consequences of IUGR, cardiac remodeling has been observed [8, 13, 59], affecting the ventricular SpI, ratio of apex-base length \mathcal{L} to basal diameter ϕ ($SpI = \mathcal{L}/\phi$), primarily in the LV [60]. This morphological remodeling has been observed in both newborns and preadolescents (8-12 years) [13], although its persistence into adulthood appears to be subtle [48]. Additionally, studies in adults suggest that individuals who experienced restricted growth during fetal and early childhood stages exhibit greater left ventricular mass, particularly affecting the interventricular septum and left posterior wall. This is reflected by a significant increase in the relative wall thickness in the IUGR cohort [61], with a similar trend also observed in preadolescents diagnosed with severe IUGR [13]. Another study in adults born at term with a history of IUGR reported a significant reduction in basal left ventricular diameter in the IUGR cohort, but no differences in posterior ventricular wall thickness [62].

Regarding electrophysiology, clinical data from preadolescents have shown differences in the dominant vectors of depolarization and repolarization loops across the three spatial planes of the VCG [14], findings that are supported

by *in silico* simulations [63]. Similar electrical alterations have also been observed in adults [15]. Moreover, *In silico* studies highlight significant shifts in the direction of dominant vectors due to geometric remodeling, though some discrepancies remain when compared to clinical results [64].

The QRS_d obtained from the standard 12-lead ECG is a key marker associated with morphophysiological abnormalities and has been shown to predict congestive heart failure [39], incidents of atrial fibrillation [40], and death. Studies examining fetal QRS_d in IUGR have yielded conflicting results: while some report reduced QRS_d [51, 52], one study found no significant change [53], another observed a prolongation [54], and yet another detected no difference [55] when compared to controls.

During the repolarization phase, the QT and the T_{pe} intervals are important indicators of ventricular arrhythmias in severe cardiac conditions [41]. The T_{pe}/QT ratio serves as an index of arrhythmogenesis, reflecting the relationship between repolarization dispersion and ventricular APD [42]. Changes in the T-wave morphology are linked to AP changes across the ventricles [57].

The review of the state of the art and some of the most relevant findings aligned with this thesis are summarized in the Table 1.1. It primarily lists scientific articles that have reported geometric alterations in the heart of IUGR subjects, as well as studies that have identified changes in cardiac electrophysiology.

Study	Study design	Population	Follow-up duration	Biomarkers measured
Zaharie et al., 2019 [60]	Longitudinal prospective cohort study	40 neonates with IUGR and 21 newborns with birthweight AGA	Evaluation at 24–48 hours of life and follow-up at 6 months of age	Left heart measurements were significantly lower in IUGR newborns compared to AGA cohort
Sarvari et al., 2017 [13]	Prospective cohort study	58 children with FGR and 94 controls with normal fetal growth	From fetal life to preadolescence (8–12 years old)	LV SpI reduced in IUGR cohort
Arnott et al., 2015 [48]	Prospective longitudinal cohort study	157 adults born SGA and 627 born AGA	31 years (from birth to age 34–49)	Adults born SGA have some statistically significant but subtle changes in cardiac structure and function
Vijayakumar et al., 1995 [61]	Prospective cohort study	290 men born between 1920 and 1930 in East Hertfordshire, England	From birth to adulthood	Enlarged LV mass associated with reduced growth in infancy, affecting both the interventricular septum and the LV posterior wall
Bjarnegård et al., 2013 [62]	Prospective cohort study	19 young adults (aged 22–25 years) born at term after IUGR with abnormal fetal blood flow, and 18 healthy controls	Approximately 22–25 years	Significant reduction in basal LV diameter in the IUGR cohort, but no differences in posterior ventricular wall thickness
Ortigosa et al., 2016 [14]	Cross-sectional study	125 preadolescents: 33 with severe IUGR and medically-induced preterm birth, 32 with spontaneous preterm birth and AGA, and 60 controls born at term with AGA		Preterm-IUGR subjects showed increased angles in depolarization (vs. XY plane and repolarization vector) and decreased repolarization angle (vs. XZ plane) compared to controls
Bueno-Palomeque et al., 2020 [63]	Computational simulation study	Not applicable	Not applicable	T-wave/XZ-plane angle increased in globular model. QRS-T XY-plane angle was lower in control. A more globular LV alters QRS/T-wave loop angles
Ortigosa et al., 2018 [15]	Cross-sectional study	87 adults (54 with a history of IUGR and 33 controls)	Not applicable	In the frontal plane (XY), the QRS-T angle was statistically significantly larger in controls (13.49 ± 13.65) compared to IUGR adults (9.26 ± 8.47)
Bueno-Palomeque et al., 2023 [64]	Computational simulation study	Not applicable	Not applicable	QRS-T angle trends align with clinical data, supporting the link between IUGR-induced morphological remodeling and observed angle changes

Ilkhanoff et al., 2012 [39]	Prospective cohort study	4,591 adults (mean age 61 years; 51% women; 39% White) without baseline cardiovascular disease	Mean of 7.1 years	$QRS_d > 100$ ms was significantly associated with incident heart failure
Aeschbacher et al., 2018 [40]	Prospective cohort study	15,314 participants from the Atherosclerosis Risk in Communities (ARIC) study, free of atrial fibrillation at baseline	Not specified	QRS_d was an independent predictor of incident atrial fibrillation among women, but not in men
Brambati et al., 1982 [51]	Observational study	26 fetuses diagnosed with IUGR	Not applicable	QRS_d measurements two standard deviations below the normal value in IUGR group
Pardi et al., 1986 [52]	Observational study	68 fetuses with ultrasound evidence of growth retardation	Not applicable	44 showed QRS_d below two standard deviations from the mean normal value
Grimm et al., 2003 [53]	Observational study using fetal magnetocardiography	30 fetuses with IUGR and 60 normotrophic fetuses	Not applicable	Non-significant difference in QRS_d
Van Leeuwen et al., 2001 [54]	Observational study using fetal magnetocardiography	6 fetuses with IUGR and 39 healthy fetuses as controls	Not applicable	Significantly longer QRS_d in an IUGR group
Velayo et al., 2017 [55]	Descriptive observational study	15 fetuses with early IUGR and 20 gestational age-matched healthy controls, between 20+0 and 33+6 weeks of gestation	Not applicable	No significant difference in QRS_d . A significant prolongation of the QT interval in the IUGR group
Yamaguchi et al., 2003 [41]	Observational study	27 patients with acquired Long QT Syndrome	Not applicable	QT and T_{pe} have been identified as predictors of ventricular arrhythmias in severe cardiac conditions
Gupta et al., 2008 [42]	Review article	Not applicable	Not applicable	The ratio T_{pe}/QT is considered an index of arrhythmogenesis
Emori and Antzelevitch, 2001 [57]	Experimental study using canine ventricular myocyte	Canine ventricular myocytes	Not applicable	Changes in the T-wave morphology are linked to AP changes across the ventricles

Table 1.1: Characteristics of the studies included in this research



CHAPTER 2

METHODOLOGY AND COMPUTATIONAL MODELS IN CARDIAC ELECTROPHYSIOLOGY

-
- 2.1 Modeling cardiac electrophysiology**
 - 2.1.1 Hodgkin-Huxley model
 - 2.1.2 Ventricular action potential models
 - 2.1.3 Bidomain and monodomain equations
 - 2.2 Software and computational tools**
 - 2.2.1 Finite elements in electrophysiology
 - 2.2.2 Simulation framework (ELECTRA)
 - 2.3 Anatomical model with reduced sphericity index**
 - 2.3.1 Parameters controlling the deformation of the biventricular model
 - 2.4 Signal processing and analysis**
 - 2.4.1 Pseudo-ECG generation and analysis
 - 2.4.2 Dominant vectors of QRS and T Waves in VCG
 - 2.4.3 Detection and delineation in ECG
 - 2.4.4 Principal component analysis in ECG
 - 2.4.5 Dataset
-

Computational models play an important role in cardiac electrophysiology, serving as fundamental tools for the understanding of underlying mechanisms in biomedical engineering research. These models integrate anatomical, functional, biophysical, and electrophysiological data, facilitating the analysis of cellular and tissue dynamics under diverse physiological and pathological conditions. Within the scope of this research, computational simulations were

developed using realistic heart and torso models. Based on these, globular models were generated to model the anatomical remodeling of IUGR subjects, and subsequently to simulate electrophysiological behaviour at the organ level.

This chapter details the methods and tools employed in the development of the simulation environment, the cellular models utilized, and the aspects incorporated into the simulations to enhance their realism. Additionally, it details the biosignal processing tools used for the delineation and analysis of ECG-based interval measurements.

2.1 Modeling cardiac electrophysiology

Cellular electrophysiology has undergone remarkable advancements through the development of mathematical and computational models that describe the electrical behavior of excitable cells, leveraging experimental data. In particular, AP models have evolved from simplified representations to highly detailed descriptions that integrate multiple physiological and molecular variables [65].

Early models, such as the one developed by Hodgkin and Huxley in 1952 [66], focused on the quantitative description of primary ionic currents: sodium, potassium, and a leakage current. This model, based in differential equations, provided a framework to describe the ionic current dynamics responsible for the generation and propagation of AP, laying the foundation for future model developments. Experimental techniques, such as the voltage-clamp method, were essential in providing precise data on the biophysical characteristics of ionic channels [65].

In recent decades, technological and computational advancements have facilitated the creation of models that incorporate interactions among multiple cellular components, such as voltage-gated ion channels, Na^+/K^+ ATPase pumps, $\text{Na}^+/\text{Ca}^{2+}$ exchangers, and intracellular calcium dynamics. These developments have expanded the capabilities of models to simulate complex phenomena, including cellular refractoriness, pharmacological modulation, and intracellular calcium oscillations, which are crucial for understanding cardiac contraction [66].

Furthermore, the personalization of AP models using individual data has gained prominence with the integration of artificial intelligence and machine learning techniques. These tools have enabled the fine-tuning of specific parameters based on patient characteristics, driving advancements in personalized medicine and the design of more effective treatments [67]. AP models as the one developed by O'Hara et al., have incorporated high-resolution experimen-

tal human data, achieving simulations that accurately represent normal and pathological cardiac electrophysiology [25].

2.1.1 Hodgkin-Huxley model

The Hodgkin-Huxley model first described the dynamics of the AP in excitable cells such as neurons or muscle fibers. This model, based on differential equations, represented the flow of ionic currents across the cell membrane and their relationship with changes in the membrane potential. The model specifically characterized the propagation of the electrical impulse in a squid giant axon, modulated by three ionic currents: the sodium current (I_{Na}), the potassium current (I_{K}), and a leakage current (I_{l}). Each current was defined as follows:

$$I_{\text{Na}} = g_{\text{Na}}m^3h(V_m - E_{\text{Na}}), \quad (2.1)$$

$$I_{\text{K}} = g_{\text{K}}n^4(V_m - E_{\text{K}}), \quad (2.2)$$

$$I_{\text{l}} = g_{\text{l}}(V_m - E_{\text{l}}), \quad (2.3)$$

where g_{Na} , g_{K} , and g_{l} represent the maximum conductances for sodium, potassium, and leakage currents in mS/cm^2 , E_{Na} , E_{K} , and E_{l} represent the equilibrium potentials for sodium, potassium, and leakage currents in mV. The m , h , and n are the so-called gating variables that control the opening and closing of ion channels and can vary between 0 and 1 to represent the channel's state. Each gating variable follows the time-dependent equation:

$$\frac{dx}{dt} = \alpha_x(1 - x) - \beta_x x, \quad (2.4)$$

where x represents the gating variables (m , h , and n), α_x represents the rate of channel opening, and β_x determines the rate of channel closing. The equations governing these variables are as follows:

$$\begin{aligned} \alpha_m &= 0.1 \frac{25 - V}{e^{(25-V)/10} - 1}, & \beta_x &= 4e^{-V/18}, \\ \alpha_h &= 0.07e^{-V/20}, & \beta_h &= \frac{1}{e^{(30-V)/10} + 1}, \\ \alpha_n &= 0.01 \frac{10 - V}{e^{(10-V)/10} - 1}, & \beta_n &= 0.125e^{-V/80}. \end{aligned}$$

To simulate an AP, these differential equations are solved numerically using methods such as Euler or Runge-Kutta [68], adjusting initial conditions

and experimental parameters. Numerical methods are essential because the equations are nonlinear and require iterative approaches to obtain accurate temporal solutions for the membrane potential and gating variables.

The Hodgkin-Huxley model provides a conceptual framework for understanding how ionic channels interact to generate and propagate electrical signals in excitable cells. This model has served as the foundation for the development of more sophisticated models in neuroscience and cardiology, enabling the simulation of complex phenomena such as arrhythmias, synaptic integration, and neural network activity.

2.1.2 Ventricular action potential models

The evolution of computational models for studying cardiac APs has been crucial for understanding the electrical mechanisms of the human heart. From the early models based on the work of Hodgkin-Huxley in 1952 to Denis Noble's contributions in 1960, these approaches have advanced significantly, incorporating increasingly detailed and specific experimental data to address complex phenomena. Nowadays, the O'Hara-Rudy action potential cell model (ORd), stands out as one of the most comprehensive and advanced tools in cardiac electrophysiology [25].

The ORd model was developed using a robust dataset derived from over 100 healthy human hearts. This approach represented a substantial improvement over earlier models, which primarily relied on animal data extrapolated to human physiology. The ORd model reformulated equations to more accurately represent the behavior of critical ionic currents, such as L-type calcium current (I_{CaL}), I_{K+} , and Na^+/Ca^{2+} exchanger currents, all of which are essential for maintaining the AP.

An innovative feature of the ORd model was the inclusion of Ca^{2+} /calmodulin-dependent protein kinase II (CaMKII) effects on ionic currents, enabling the simulation of intracellular calcium modulation under both physiological and pathological conditions. Additionally, the model incorporated transmural heterogeneities, accounting for functional differences among epicardial, midmyocardial, and endocardial cells based on messenger RNA and protein expression data.

Unlike models such as TP06 by ten Tusscher [67] or GPB by Grandi [69], the ORd significantly improved the representation of calcium dynamics. These advancements enabled the simulation of complex phenomena such as early afterdepolarizations, which previous models struggled to replicate accurately.

Furthermore, the ORd provided a robust framework for studying arrhythmias and evaluating pharmacological therapies' effects on ionic currents and APs.

The ORd model has been widely used to investigate arrhythmic mechanisms, assess the efficacy of pharmacological treatments, and explore the pathophysiology of cardiac diseases. Its efficient design allows for multiscale simulations, ranging from individual cells to tissue and whole-heart models. This multiscale approach facilitates the analysis of complex interactions between cellular and tissue levels, offering valuable insights for developing personalized therapies.

The ORd model for healthy tissue was used for the simulations performed in this study, both for the control model and for all globular models. Apicobasal heterogeneities were incorporated by reducing I_{K_s} to achieve a more realistic propagation. These modifications were applied consistently across all simulated models. The adjustment factor is detailed in Section 3.2.2.

Among recent models of human ventricular electrophysiology is the ventricular cell model developed by Tomek et al. (ToR-ORd) [70], builds upon the ORd framework and accurately reproduces experimental data under both normal and pathological conditions. It includes updated formulations for ion channels such as the L-type calcium current, and emphasizes accurate restitution properties and drug-response simulation. Another notable model is the BPS2020 model by Bartolucci et al. [71], which was developed with a focus on reproducing experimental variability and inter-subject heterogeneity exploring changes in ventricular electrophysiology induced by electrolyte changes such as Ca^{2+} concentrations. Both models contribute to the understanding of ventricular electrophysiology, supporting a wide range of applications from mechanistic studies to *in silico* drug testing.

2.1.3 Bidomain and monodomain equations

In computational modeling of cardiac electrophysiology, the equations describing the propagation of the AP in cardiac tissue are not limited to reproducing ionic activity in cardiomyocytes but also represent varying levels of complexity and simplification in simulating the heart's electrical activity.

The bidomain equation describes the propagation of the electrical potential by considering two distinct domains: the intracellular domain and the extracellular domain. The interaction between these domains is mediated by the cell membrane, which acts as a capacitor separating the two regions. The bidomain system allows modeling phenomena such as the anisotropy of electrical

conductivity in cardiac tissue, providing a detailed representation of the electrical activity. However, it is computationally expensive due to the requirement to solve equations for both domains simultaneously.

The bidomain equations are derived from the conservation of current and charge, assuming the sources are related to the cell membrane. By combining the capacitive current (I_c) and the ionic current (I_{ions}) into the total transmembrane current (I_m), the bidomain equations can be expressed as follows:

$$\nabla \cdot (\sigma_i \nabla \phi_i) = \beta \left(C_m \frac{\partial V_m}{\partial t} + I_{\text{ion}} \right), \quad (2.5)$$

$$\nabla \cdot (\sigma_e \nabla \phi_e) = -\beta \left(C_m \frac{\partial V_m}{\partial t} + I_{\text{ion}} \right), \quad (2.6)$$

where σ_i and σ_e are the conductivities of the intracellular and extracellular domains in S/m, ϕ_i and ϕ_e represent the potentials in the intracellular and extracellular domains in V, β is the surface-to-volume ratio of the cell membrane in m^{-1} , C_m is the capacitance of the cell membrane in F/m^2 , $V_m = \phi_i - \phi_e$ is the transmembrane potential in V, and I_{ion} is the ionic current density through ion channels, pumps, and exchangers in A/m^2 .

The boundary conditions assume that currents at the boundaries only flow through the extracellular space:

$$\mathbf{n} \cdot (\sigma_i \nabla \phi_i) = 0, \quad (2.7)$$

$$\mathbf{n} \cdot (\sigma_e \nabla \phi_e) = I_e, \quad (2.8)$$

where \mathbf{n} is the outward-facing unit normal vector and I_e is the applied extracellular current density in A/m^2 . The bidomain equations are important in scenarios where the extracellular space is relevant such as research in defibrillation shocks [72].

The monodomain equation is a simplification of the bidomain equation, assuming a linear relationship between intracellular and extracellular conductivities [73]. Under this assumption, the two domains are combined into a single domain, removing the need to calculate ϕ_i and ϕ_e separately. This assumption reduces computational complexity, making the monodomain model less expensive to solve compared to the bidomain model. The monodomain equation is formulated as:

$$\nabla \cdot (\sigma \nabla V_m) = \beta \left(C_m \frac{\partial V_m}{\partial t} + I_{\text{ion}} \right), \quad (2.9)$$

where σ is the intracellular conductivity in S/m, V_m is the transmembrane potential ($\phi_i - \phi_e$). The monodomain model typically assumes isolated (no-flux) boundaries, enforcing zero transmembrane current via a homogeneous Neumann condition.

In this thesis, electrical impulse propagation is simulated using the monodomain model, which has been reported as suitable for studying propagation of APs at the scale of the human heart in the absence of applied currents [74].

2.2 Software and computational tools

2.2.1 Finite elements in electrophysiology

The finite element method (FEM) is commonly used to solve problems in electrophysiology, which involve the conservation of intracellular and interstitial charge, and is based on a system of nonlinear partial differential equations, specifically, a system of reaction-diffusion equations. This equation describes the phenomenon of electrical potential propagation through the cardiac muscle, along with the reactions generated due to the opening and closing of ion channels.

For the application of FEM, the domain under study is divided into a finite number of subdomains or elements, and the Galerkin method is applied to each one of these [75]. The elements do not overlap or intersect. Generally, in 2D, triangular or square elements are used, while in 3D, tetrahedrons and hexahedrons are employed. The size of each element and its aspect ratio are crucial for proper analysis using FEM. The smaller the element, the more accurate the solution, but it involves a high computational cost. To determine the formulation of the solution for a reaction-diffusion system, a one-dimensional space can be established within a defined domain (Ω). The weak formulation of equation (2.9) is obtained by multiplying the equation by a weight w and integrating over the domain Ω of the problem [76].

$$\int_{\Omega} C_m V_t w \, d\Omega = - \int_{\Omega} D \nabla V w \, d\Omega + \oint_{\Gamma} D \nabla V w \, d\Gamma - \int_{\Omega} I_{ion} w \, d\Omega, \quad (2.10)$$

where Γ defines the boundary of the system's domain.

To discretize the proposed expression, the number of elements into which the original domain was divided is considered, and the potential can be expressed as a linear combination of base functions as follows:

$$V(\mathbf{x}, t) \approx \sum_{j=1}^{n^e} N_j^e(\mathbf{x}) V_j^e(t), \quad (2.11)$$

where n^e is the total number of nodes of an element, $V_j^e(t)$ is the voltage at the j -th node, dependent on time t , and $N_j^e(\mathbf{x})$ are the basis functions associated with node j . This equation can be written in matrix form as follows:

$$\mathbf{V}(\mathbf{x}, t) = (\mathbf{N}^e)^T \mathbf{V}^e(t), \quad (2.12)$$

by substituting the approximations of V into the weak form of equation (2.10) and setting $w = N$, a time-discretized equation for node i of element j is obtained:

$$\sum_{j=1}^{n^e} (M_{i,j}^e \dot{V}_j^e + K_{i,j}^e V_j^e) = Q_i^e, \quad (2.13)$$

$$\mathbf{M}^e \{\dot{\mathbf{V}}^e\} + \mathbf{K}^e \{\mathbf{V}^e\} = \mathbf{Q}^e, \quad (2.14)$$

where:

$$M_{ij}^e = \int_{\Omega} C_m N_i N_j d\Omega, \quad (2.15)$$

$$K_{ij}^e = \int_{\Omega} D(N_i)_x (N_j)_x d\Omega, \quad (2.16)$$

$$Q_i^e = \int_{\Omega} (N_i) I_{ion} d\Omega. \quad (2.17)$$

The matrices are assembled to generate a system of equations for the entire domain:

$$\mathbf{M}\dot{\mathbf{V}} + \mathbf{K}\mathbf{V} = \mathbf{Q}. \quad (2.18)$$

Solving the resulting reaction-diffusion system of equations requires very small time steps, for which various time-stepping methods exist. A fixed, small time step can be used to ensure the convergence of the result, or an adaptive time step can be assigned, as there are stages of the cardiac AP, such as depolarization, where the potential changes rapidly over a short period of time.

2.2.2 Simulation framework (ELECTRA)

ELECTRA v0.5.1 is a cardiac electrophysiology simulator developed by the BSICoS research group (Biomedical Signal Interpretation and Computational Simulation) at the University of Zaragoza. The software was primarily built using a C++ library and employs FEM [77] and Meshfree [78, 79] techniques to solve monodomain and bidomain models for simulating the heart's electrical activity. ELECTRA enables detailed simulations of action potential propagation in cardiac tissue, facilitating the study of phenomena such as arrhythmias and other cardiovascular diseases. It integrates seamlessly with real anatomical data, allowing for precise and clinically relevant simulations in both research and clinical contexts.

The interaction with ELECTRA requires a universal scripting file in JSON (JavaScript Object Notation) format. This file contains all the information associated with the electrophysiological simulation process. Below are the parameters that must be configured for the simulation:

- **Version and Data:** The header of the document includes information about the software, its version, license details, and contact information.
- **Simulation:** In the version used (v0.5.1), the user must specify a simulation name and the simulation scale (cell or tissue).
- **Reference Units:** This section defines the units for time, capacitance, and current to be used during the simulation. For our case, we used ms (milliseconds), pF (picofarads), and mA (milliamps).
- **Tissue:** This section defines the attributes of the geometry, including units, dimensionality, number of vertices, and the file path for the geometry to be used in the simulation (the input mesh file should be in **.inp* format):
 - The dimensions parameter allows the user to select 1D, 2D, or 3D simulations.
 - The number of vertices refers to the element type:
 - 1D: linear elements with 2 vertices.
 - 2D: triangular or quadrilateral elements with 3 or 4 vertices.
 - 3D: tetrahedral or hexahedral elements with 4 or 8 vertices, respectively.
- **Material:** This section defines the electrical properties for the simulation:

- Type: ELECTRA currently supports only transverse anisotropy.
 - Diffusivity units: In our study, we used cm^2/ms .
 - Transmembrane diffusivity: A single value is set for monodomain models. For bidomain models, two additional diffusivity parameters can be set for internal and external.
 - Transversal ratio: Specifies the percentage of diffusivity applied in the direction perpendicular to the fiber orientation.
- Fibers: In the version of ELECTRA used, a unit vector representing fiber direction is required. The number of components in the vector corresponds to the simulation dimensionality (X, Y for 2D; X, Y, Z for 3D).
 - Stimuli: This section defines the characteristics of the electrical stimuli that initiate propagation in the model:
 - Number of stimuli: An n number of stimuli can be defined, with each stimulus described as follows:
 - Id: stimulus identifier.
 - Nodeset: node group where the stimulus is applied.
 - Start: stimulus onset time.
 - Duration: duration of the applied stimulus.
 - Cycle length: period after which the stimulus repeats.
 - Amplitude: current amplitude of the stimulus.
 - Electrophysiology: This section defines the action potential propagation models to be used in the simulation.
 - Model number: Specifies how many regions of the geometry will be assigned distinct electrophysiological models.
 - Model-1: This defines the model type, cell type, and associated nodeset. Ventricular models include: Bueno2008 [80], O’Hara2011 [25], Gong2020 [81], and Paci2013v [82]. For the conduction system, the Stewart2009 [20] model is available. Cell types can also be configured as ventricular (endo, mid, epi), atrial (left atrial, right atrial) or Purkinje.
 - Initial conditions for the model’s state variables can also be imported from an external file

- **Conduction System:** The cardiac conduction system is treated as a separate section.
 - **Geometry:** Specifies the file path of the Purkinje network geometry, units for node positioning, and the PMJ radius (representing the connection region between Purkinje terminals and the endocardial surface of the ventricular model).
 - **Nodesets:** Two groups are defined:
 - **av_node:** nodes corresponding to the atrioventricular section of the network.
 - **puki_end_nodes:** terminal nodes of the Purkinje branches.
 - **Diffusivity:** Defines the global or local diffusivity of the network and PMJs.
 - **Electrophysiology:** Specifies the action potential model for the conduction system.
- **Physics:** This section configures the reaction-diffusion system:
 - **Type:** monodomain or bidomain.
 - **Solver:** numerical solver to be used for system resolution. The simulator allows users to choose between monodomain and bidomain models and offers various numerical solvers: Forward Euler, a dual adaptive explicit time integration method [77], Backward Euler, and Crank-Nicholson. Finally, the output file paths must be specified in the configuration file, ensuring the results are stored in designated directories.
 - **Dt unit:** defines the time step unit and its min/max limits.
 - **Simulation time:** total simulation duration.
 - **Output Interval:** Specifies the frequency at which computed results are saved.
- **Post-Processing:** Defines the time window for computing local activation times.
- **Output:** Specifies the directory for saving simulation results, including both propagation in the Purkinje network and the cardiac model.

In used version of ELECTRA, the program runs just on a CPU. For the simulations in this study, we used a desktop computer with an Intel(R) Core(TM)

i7-9700K processor running at 3.6 GHz, and with 32 GB of RAM. Simulating one heartbeat for the biventricular model with the Purkinje network required approximately 1.3 hours.

2.3 Anatomical model with reduced sphericity index

In various studies across different age groups, the prevalence of these anatomical changes in the cardiac muscle has been demonstrated. In children, cardiovascular assessments that included echocardiography and blood pressure measurement have shown that cardiac changes persisted from birth until 6 months of age [8]. In preadolescent patients, evidence obtained through echocardiography and three-dimensional analysis of heart shape indicates that remodeling persists, showing similar results to those observed in childhood [13]. Subsequent tests conducted on adults have corroborated the findings observed in studies on children and preadolescents. Using surface electrocardiography recordings and generating a VCG, a statistically significant variation was found between the angle of the dominant QRS depolarization vector and the T repolarization angle in the XY plane between a control group and a group with IUGR. This difference could be crucial for the cardiovascular risk of patients with IUGR [15].

2.3.1 Parameters controlling the deformation of the biventricular model

The *in silico* simulation of the geometric changes in the cardiac muscle was based on the human biventricular model, which was used in this study as the control model (\mathcal{C}). This biventricular mesh was embedded in a torso volume generated from computer tomography images of a 43 year old woman. The heart and torso meshes were combined by rotating and translating into anatomically-realistic concordance as described in [83].

To deform the \mathcal{C} model, we used the nonlinear finite element solver for biomechanics FEBIO v2.9.1 [84]. In the preprocessing application for FEBIO, PreView, we formulated a stress-strain problem to deform the human biventricular model, characterized as an elastic tissue and subjected to mechanical stress applied to the ventricular walls until a deformation percentage similar to that reported in the literature was reached. For this purpose, the coordinate and connectivity matrices from the original **.mat* file were converted into an **.stl* file, and the information was imported into the PreView software. At this stage of the research, we analyzed the proposed methodology for generat-

ing globular models and its applicability in obtaining appropriate results for SpI reduction and subsequent electrophysiological simulation. The geometric change approach focused on the LV in accordance with the evidence reported in [13,85]. Fig. 2.1 presents a synthesis of our main objective at this stage: to simulate the geometric changes resulting from IUGR.

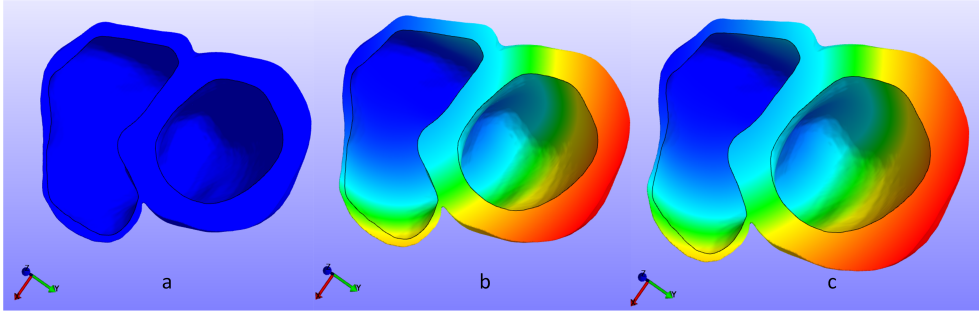


Figure 2.1: a: Biventricular control model and, b and c: two globular variations obtained by applying tensile force to the free wall of the LV. The color blue indicates regions without deformation, while the color red represents maximum deformation.

To generate a geometric change in the LV, we applied certain movement constraints to specific regions of the heart model, particularly on the RV. The displacement along the X -axis is denoted as $f_x(x_k)$ at the x_k coordinate of the k -th node, $f_y(y_k)$ for the Y -axis, and $f_z(z_k)$ for the Z -axis. A restriction on node movement along a specific axis is denoted as $f_x(x_k), f_y(y_k), f_z(z_k) = 0$. The regions with constraints and the forces applied are shown in Fig. 2.2, setting various regions of movement restrictions and applying force in the radial direction from the LV endo. In general, we applied two types of forces to reduce the SpI. The first force was applied to the LV free wall to increase the basal diameter ϕ , followed by a force applied along the longitudinal axis in the apex-to-base direction to reduce its length \mathcal{L} . The procedure for generating the globular models is detailed in the next section.

As a result of the deformation processes on the \mathcal{C} model, a displacement matrix for each of the mesh nodes was obtained. This information was used to generate the globular models in MATLAB by adding nodal displacements to the original coordinate matrix. This methodology for generating globular models was maintained throughout this study, with several algorithmic improvements to develop them more efficiently. Chapter 3 will detail the parameters used for the generation of eight globular models (\mathcal{G}_A to \mathcal{G}_H), and Chapter 5 will present the geometric parameters employed to generate eight different globular models (\mathcal{G}_1 to \mathcal{G}_8).

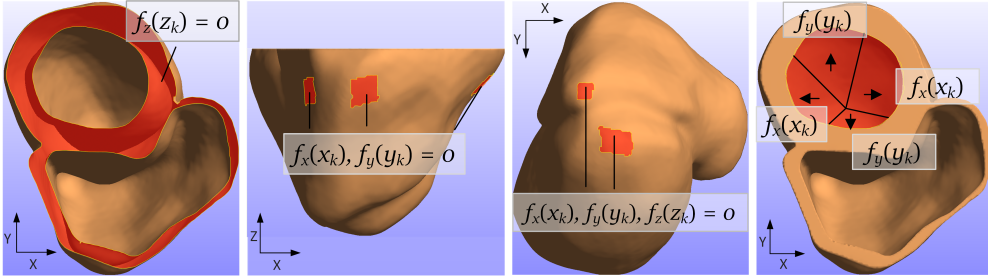


Figure 2.2: *.stl file of the human biventricular model in PreView software, showing surface regions assigned with zero mobility ($f_x(x_k), f_y(y_k), f_z(z_k) = 0$) as reference and the forces applied to the LV endocardial surface to achieve the globular models.

2.4 Signal processing and analysis

2.4.1 Pseudo-ECG generation and analysis

For the calculation of the surface ECG, an algorithm was used that utilizes the monodomain system solution previously obtained from ELECTRA. By inputting the torso volume, the extracellular potential is computed. This extracellular potential calculation on the virtual electrodes was performed in MATLAB, using a volume conductor model [22, 86] as follows:

$$\phi(\mathbf{e}, t) = \int_{\Omega} \left(-\mathbf{D} \cdot \nabla_{\mathbf{r}} V_m(\mathbf{r}, t) \cdot \left(\nabla_{\mathbf{r}} \frac{1}{\|\mathbf{r} - \mathbf{e}\|} \right) \right) d\mathbf{r}, \quad (2.19)$$

where $\phi(\mathbf{e}, t)$ is the extracellular potential calculated at $\mathbf{e} = [e_x \ e_y \ e_z]$, the spatial coordinates of the electrodes; \mathbf{D} is the diffusion tensor of the tissue, considered constant and homogeneous in this study; $V_m(\mathbf{r}, t)$ is the membrane potential; and $1/\|\mathbf{r} - \mathbf{e}\|$ represents the decay of the electric field with distance, and Ω is the volume where the tissue is located. For the simulation of the control model \mathcal{C} and globular models \mathcal{G} , a desktop computer Intel Core i7-9700K CPU at 3.60 GHz and 32 GB of RAM was used. Later, to perform the displacement test described in the Section 3.3, the extracellular calculation was executed on the HERMES cluster of the I3A Institute, as this test required simulating over 100 different scenarios. As a result of this algorithm, a matrix was obtained with a number of rows corresponding to the simulation time in milliseconds (3000 rows for a simulation of 3 heartbeats lasting 1000 ms each) and 12 columns representing the leads I, II, III, aVR, aVL, aVF, V1, V2, V3, V4, V5, and V6.

2.4.2 Dominant vectors of QRS and T Waves in VCG

The spatial representation of electrical activity through a VCG can be generated from an ECG using various methods. The most widely used method is Dower's [87], which employs a linear transformation matrix that relates the standard ECG leads to the X, Y, and Z components of the VCG. Other commonly used methods include Frank's and Kors' methods [36–38], which also use inversion matrices but with different coefficients. The table below presents the coefficients proposed in Dower's method.

Lead	X	Y	Z
V1	-0.172	0.057	-0.229
V2	-0.074	-0.019	-0.310
V3	0.122	-0.106	-0.246
V4	0.231	-0.022	-0.063
V5	0.239	0.041	0.055
V6	0.194	0.048	0.108
I	0.156	-0.227	0.022
II	-0.010	0.887	0.102

Table 2.1: Inverse Dower matrix coefficients

To assess the dominant vector direction of the electrical wavefront along the depolarization and repolarization loops, we used the inverse Dower's transform [87] to transform the 12-lead ECG into the orthogonal leads X, Y, and Z of a VCG, rather than directly computing the VCG. The rationale behind this choice is to closely replicate the approach used in the studies analyzing clinical data [14], which are being used as a reference for comparing clinical and simulated results. Next, we calculated the angles of the dominant vectors relative to the transverse, XZ, frontal, XY, and sagittal, ZY planes according to the angular variables measured in [15].

2.4.3 Detection and delineation in ECG

Biomedical signals are signals that carry information that is used in the biomedical field for the diagnosis, monitoring, or treatment of various conditions or pathologies under study. The entire process of obtaining information from a biosignal may involve different processing stages depending on the quality of the acquired signal and the specific information that needs to be observed. The role of ECG signal processing has gained increasing prominence as it allows ac-

curate measurements of signals recorded under complex conditions, such as in ambulatory settings.

The diagram in the Fig. 2.3 shows a set of blocks that group the main signal processing tools that could be used for the processing of an ECG signal, starting with the noise filtering stage, which addresses noise from various sources related to the recording process and from electromagnetic sources, QRS complex detection, delineation, and data compression. This general scheme can be adapted to emphasize different types of specific analyses.

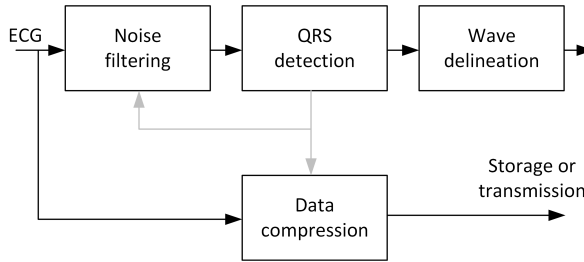


Figure 2.3: General diagram of the stages for ECG signal processing [23].

One of the stages in ECG signal processing is automatic delineation, which functions to determine the boundaries of the different recorded PQRST waves, allowing for the measurement of their amplitude and the duration of various intervals. Accurate delineation of these waves is crucial for the diagnosis of several cardiac conditions. Different mathematical and computational techniques are currently used for automatic detection. Among these methods are wavelet transform-based techniques [88, 89] and deep learning application [90, 91], among others, which aim to achieve higher precision and are evaluated through testing on various databases.

The wavelet transform (WT) decomposes a signal and represents it as a combination of a set of basis functions obtained by dilating a factor “ a ” and translating in time by “ b ” a mother wavelet $\psi(t)$. The WT of a signal $x(t)$ is defined as follows:

$$W_x(a, b) = \int_{-\infty}^{\infty} x(t) \frac{1}{\sqrt{|a|}} \psi\left(\frac{t-b}{a}\right) dt, a > 0. \quad (2.20)$$

For the detection of the waves in an ECG signal, a wavelet prototype $\psi(t)$, such as the derivative of a smoothing function $\theta(t)$, can be used, mainly because an ECG signal consists of slopes, positive and negative peaks at different scales [89]. The first five scales of the discrete wavelet transform (DWT) contain most

of the energy of an ECG signal. In Fig. 2.4, simulated ECG signals are shown along with the response up to the fifth scale of the DWT. It can be observed in this image that the different scales provide distinct information for the various stages of the ECG. In Fig. 2.4, QRS, it is evident that scales 1 and 2 clearly detect the QRS complex, while for the P or T waves, their shapes are better represented in scales 4 and 5.

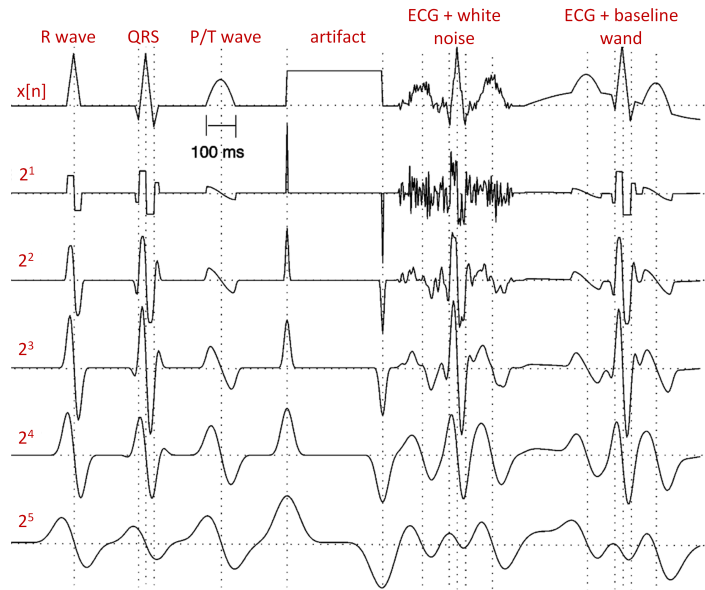


Figure 2.4: Five levels of WT interval scales from a simulated ECG signal. Adapted from [89].

To detect the QRS complex, the different scales obtained from the DWT are analyzed, and certain signal shape parameters are detected. In the QRS complex, the detection of the R peak is relatively easy, as it involves searching for values that exceed specific thresholds, which can be done across various scales (see Fig. 2.4). Subsequently, isolated or redundant maximum lines are removed. For each pair of maximum and minimum values, the point where the signal crosses zero is identified, and finally, a sweeping process is performed to ensure no QRS complex is missed.

For the detection and delineation of the T-wave, the prior identification of the QRS complex is crucial, as its presence and the identification of the RR interval indicate the region where the T-wave should be located. The detection can be performed by defining a search window. Within this window, maximum peaks are searched. If at least two points exceed the threshold, the presence

of a T-wave is considered. Next, the points where the signal crosses zero are identified. Subsequently, the wave is classified according to its polarity, and if it cannot be detected, a different scale is analyzed.

2.4.4 Principal component analysis in ECG

The principal component analysis (PCA) is a statistical technique used to reduce the dimensionality of a data set while preserving the main characteristics of the original data. This tool has important applications in the analysis of ECG signals, considering that in clinical practice, a standard 12-lead ECG set is typically available for each patient [92,93]. The principal components of a group of signals are obtained from the linear combination of these original variables. Each principal component results from the weighted sum of the original variables, each characterized by specific weights. The assigned weights are determined such that the principal components are orthogonal to each other, ensuring no redundancy between them and that each component contains different information. The first components represent the most significant variations and patterns of the original dataset, while the following components contain less variability (see Fig. 2.5) [92].

Two transform leads, one applying PCA emphasizing the QRS complex (PCA_{QRS}), and other applying PCA emphasizing the T-wave (PCA_T), were generated. PCA separates the orthogonal components of the $L=8$ independent leads in descending order of variance [92]. The matrix Ψ_{PCA} defining the transformation was obtained (learned) from the eigenvectors of the 8×8 inter-lead ECG auto-correlation matrix computed using the samples in the QRS (or T waves) [92,94] within the corresponding learning window, for PCA_{QRS} (or PCA_T).

The 8×8 auto-correlation matrix is computed from a larger matrix, see below, where each row corresponds to one lead and contains the concatenated samples of all QRS complexes (or T waves) within the learning window. Thus, the auto-correlation captures the temporal and inter-lead relationships across all collected beats, providing the basis for extracting the principal components. As a result, the transform lead coming from the first PCA component is the lead maximizing the QRS (or T-wave) energy and selected as PCA_{QRS} (or PCA_T). To illustrate computation of matrix Ψ_{PCA} , let K be the number of segmented and aligned T waves (or QRS complexes) in the learning window, having N samples each, for L available leads. Let $x_{k,l}(n)$ denote the n -th selected sample of the k -th beat in the l -th lead of the filtered ECG signal. In vector notation, $\mathbf{x}_{k,l} = [x_{k,l}(0) \ \cdots \ x_{k,l}(N-1)]^T$ represents the T-wave (or

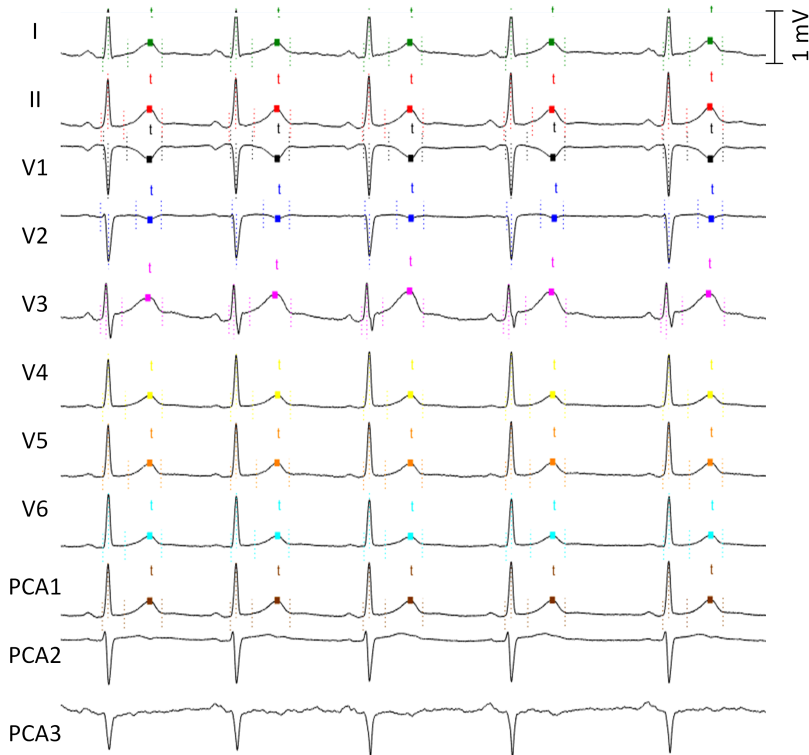


Figure 2.5: 8-lead ECG (I, II, V1 to V6) and the first three principal components of the signals. Marks are shown at the onset of the QRS, R-wave, and the onset, peak, and end of the T-wave, with different colors for each lead. The PCA transform is applied to the entire ECG waveform.

QRS complex) from the k -th beat of the l -th lead, which are piled together in the $L \times N$ matrix \mathbf{X}_k :

$$\mathbf{X}_k = [\mathbf{x}_{k,1} \quad \mathbf{x}_{k,2} \quad \dots \quad \mathbf{x}_{k,L}]^T, \quad (2.21)$$

where the n -th column of \mathbf{X}_k contains the amplitudes of the L leads at a given sample n . A data matrices \mathbb{X} is then constructed by concatenating K consecutive matrices \mathbf{X}_k ,

$$\mathbb{X} = [\mathbf{X}_1 \quad \mathbf{X}_2 \quad \dots \quad \mathbf{X}_K]. \quad (2.22)$$

To maximize the signal energy at the transform leads, it is known that the 8×8 transform matrix $\Psi_{\text{PCA}} = [\psi_1 \quad \psi_2 \quad \dots \quad \psi_8]$ should accomplish the following equation:

$$\mathbf{R}_{\mathbb{X}} \Psi_{\text{PCA}} = \Psi_{\text{PCA}} \Lambda, \quad (2.23)$$

being $\mathbf{R}_{\mathbb{X}}$ the spatial correlation matrix of \mathbb{X} , estimated as

$$\mathbf{R}_{\mathbb{X}} = \frac{1}{KN} \mathbb{X} \mathbb{X}^T, \quad (2.24)$$

and $\mathbf{\Lambda}$ a diagonal matrix containing the eigenvalues of $\mathbf{R}_{\mathbb{X}}$ at the diagonal.

If $\mathbf{x}(n) = [x_1(n) \ x_2(n) \ \cdots \ x_L(n)]^T$, $x_l(n)$ being the ECG signal samples at l -th lead, represents, in matrix notation, the multilead ECG signal at the n -th sample, then the first transform lead $\text{PCA}(n)$ (PCA_{QRS} or PCA_T) becomes

$$\text{PCA}(n) = \psi_1^T \mathbf{x}(n). \quad (2.25)$$

These transformed leads were delineated to identify the beginning, peak and end points, with lead PCA_{QRS} used for the QRS complex and lead PCA_T for the T-wave, as these leads are better suited for each case, as illustrated in Figure 2.5.

2.4.5 Dataset

The study involved the measurement of ECG intervals during both depolarization and repolarization phases using 12-lead surface ECG recordings (see Chapter 4). The study population included 93 preadolescents (from 8 to 12 years old), divided into two cohorts. The control cohort consisted of 60 term-born subjects with normal growth profiles, while the IUGR cohort comprised 33 subjects diagnosed with severe IUGR and who underwent medically induced delivery. IUGR was defined as a birth weight below the 10th percentile for gestational age combined with an abnormal umbilical artery Doppler, indicated by a pulsatility index above the 95th percentile. Adequate growth was considered when a birth weight above the 10th percentile for gestational age occurs, based on standards in [95].

The study population was described in a previously published cohort study, conducted at a tertiary university hospital in Barcelona, Spain [96]. The study conformed to the standards set by the Declaration of Helsinki, except for registration in a database. The study was approved by the Hospital Clinic Ethics Committee (Ref: HCB2014/0598) and written parental consent was obtained. For each subject, a 13-second ECG recording sampled at 1000 Hz was collected. ECG data used in this study is available under reasonable request from the authors of the clinical data acquisition study described in [96].

CHAPTER 3

QRS-T ANGLE CHANGES ASSOCIATED WITH HEART SPHERICITY IN COMPUTATIONAL IUGR MODELS

3.1 The conduction system in the computational model of human electrophysiology

- 3.1.1 Purkinje network
- 3.1.2 Fiber architecture

3.2 Transmural and apicobasal heterogeneities modeling intersubject variability

- 3.2.1 Endo-, mid-, and epicardium segmentation
- 3.2.2 Incorporation of apex-to-base heterogeneity
- 3.2.3 Generation of globular models

3.3 Confounding effect of heart location within the torso

3.4 Pseudo ECG/VCG calculation from the biventricular human model

3.5 Results

- 3.5.1 Transmural heterogeneities induced angular variation
- 3.5.2 Angular variation in globular, \mathcal{G} , models
- 3.5.3 Impact of electrode position

3.6 Discussion

- 3.6.1 Analysis of angular variability in simulation
- 3.6.2 Angular changes with electrode position

3.7 Conclusions

In Chapter 1, the state of the art related to the geometric changes observed in the cardiac muscle as a consequence of IUGR was reviewed. The evidence has shown a reduction in the SpI, characterized by a shortening of the apex-to-base length and an expansion of the basal diameter, primarily in the LV. Additionally, significant alterations in the direction of the depolarization and repolarization loops have been reported in individuals with a history of IUGR. In Chapter 2, the tools used for the electrophysiological simulations described in the current chapter were established.

To better understand the mechanisms behind these electrophysiological changes in IUGR subjects, this chapter outlines the methodology used to develop the framework for *in silico* simulations investigating how morphological changes associated with IUGR affect ventricular electrophysiological function. This chapter focuses on the dominant QRS and T angles, as well as QRS-T angles in the VCG. Additionally, it details the creation of globular cardiac models to represent hearts with varying degrees of sphericity. Simulated results of the dominant vector directions relative to different body planes were compared with clinical data [14]. The findings suggest that QRS-T angles could serve as non-invasive biomarkers for detecting structural changes in the heart caused by IUGR.

3.1 The conduction system in the computational model of human electrophysiology

In silico simulations provide a tool to study the interplay between cardiac structure and function. They enable to model hearts with specific anatomical and electrical properties, such as the changes in sphericity examined in this study. These simulations allow for a controlled exploration of how such variations impact cardiac performance, something that would be challenging or impractical to achieve in clinical or experimental settings. *In silico* simulations provide an ethical, efficient, and cost-effective alternative, enabling the study of conditions like IUGR, refining diagnostic techniques such as QRS-T angle validation, and advancing personalized medicine by modeling patient-specific cardiac characteristics to improve non-invasive diagnostics and targeted treatments.

In silico simulations of the electrophysiological activity of the ventricles were conducted using a biventricular geometry [97], taken as the reference model. The geometry was discretized into a high-resolution tetrahedral mesh, consisting of approximately $\sim 1\,870\,000$ elements and $345\,000$ nodes, ensur-

ing accurate spatial representation. Numerical simulations were carried out using the software ELECTRA [77], which implemented FEM to solve the monodomain model of electrical propagation in cardiac tissue.

3.1.1 Purkinje network

Simple approaches to initiate electrical stimulation in the biventricular model involve selecting specific regions of the endocardial tissue where the initial stimulus is applied [97,98]. The selected regions and the sequence of activation pulses are organized in a controlled manner to achieve a physiological propagation pattern. In preliminary tests conducted in this study, the endocardial surface of the ventricles was divided into regions from the apex to the base, and a sequence of stimuli was applied to achieve activation in the longitudinal ventricular direction, as shown in Fig. 3.1a. In this figure, it can be observed that the stimulated regions at the apex (red-colored regions) are larger compared to those in the mid-ventricular and basal areas.

An alternative and more realistic approach to stimulating cardiac tissue involves implementing a Purkinje network, which transmits the electrical stimulus along its branches and ultimately connects to the endocardial surface through Purkinje myocardial junctions (PMJ). These PMJs are defined based on the structure of the Purkinje network and the terminal points of its branches (see Fig. 3.1b).

The electrical propagation using this latter method starts at the bundle of His and propagated through the Purkinje network until reaching the endocardial tissue. The Purkinje network was incorporated into the model using a method based on fractal projection [99,100].

In this thesis, the electrical propagation is simulated using the latter method, starting at the bundle of His and transmitted through the Purkinje network until it reaches the endocardial tissue. To incorporate this mechanism into the model, the Purkinje network was generated using a fractal projection-based method, allowing for a realistic representation of its branching structure and connectivity.

The generation of a Purkinje network through computational modeling provides a valuable tool for realistic visualization and simulation of the fast conduction system allowing the investigation of its impact on electrical propagation in the cardiac muscle.

To generate the Purkinje network on the biventricular model, it is necessary to first identify the endocardial surfaces of the model. The model's entire

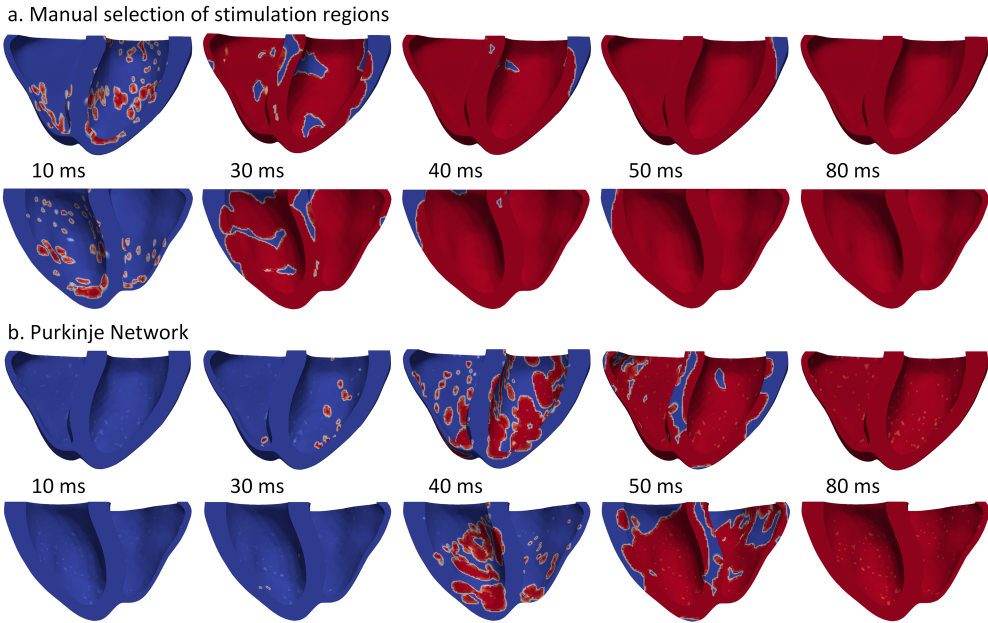


Figure 3.1: Propagation sequence of the AP. a: Simulation with manual selection of the regions where the stimulus initiates, and b: Simulation using a Purkinje network. The blue color represents an AP of -80 mV, and the red color represents $+20$ mV.

surface is represented by a triangular mesh, with the nodes belonging to the tetrahedral volumetric mesh. Considering the specific models used in this research, three surfaces were identified: the epicardial surface, and those of the RV and LV, as shown in Fig. 3.2a.

On the endocardial surface of the RV, a main branch is defined from the bundle of His to the apex, excluding stimulation terminals in the right septal region. From the bundle of His, two main branches also extend over the LV, one towards the anterior part and the other towards the posterior surface (see Fig. 3.2b). The bifurcation was positioned at the base of the biventricular model, and both the left and right bundles extend along the septal endocardial surface. The initiation site of electrical stimulation, representing the His bundle [101], was defined 2 mm from the bifurcation point.

The Purkinje network was generated using the algorithm proposed in [99]. In addition to the aforementioned guiding points, a minimum branch length and the angle between branches were input. Using the endocardial surfaces as a reference for the network, we configured a network with a branch length of 0.04 cm for the ventricular region and a branch angle of 0.45 radians for both

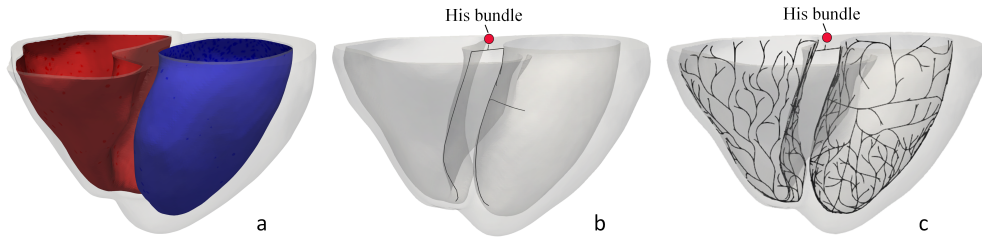


Figure 3.2: a: Endocardial surface of the right (red) and left (blue) ventricles. b: Main branch of the Purkinje network extending from the bundle of His towards the ventricles. c: Purkinje network on the ventricular endocardial surface.

ventricles. The average branch length of the resulting Purkinje network was 0.042 ± 0.026 cm, with a total of $\sim 12\,500$ nodes for the entire network. The distribution of nodes on the endocardial surfaces can be observed in greater detail in Fig. 3.3 for both ventricles.

The fast conducting system was coupled to the biventricular model, and a heartbeat simulation was performed using the ELECTRA software. During the evaluation of simulation time, it was observed that the time step for solving the system of equations decreased, which led to an extension of the overall simulation time. Without modifying the biventricular model or its mesh, we identified that the minimum configured distance between Purkinje network nodes was too small, causing the time steps to shorten. As a result, we explored Purkinje networks with a reduced number of nodes. By testing various mesh reductions, we halved the number of nodes, resulting in a decrease in total simulation time without compromising the propagation velocity across the myocardium.

During the reduction process, the nodes at branch bifurcations were identified and retained as reference points for the generation of the new mesh. From the nodes between bifurcations, every second node was selected. The final average branch length of the Purkinje network increased to 0.076 ± 0.035 cm, with a total of $\sim 7\,000$ nodes in the new complete network. Finally, using the generated nodes, two vectors were created: one containing the coordinates of the network nodes, and another for connectivity, indicating the connection order of the network branches.

This reduction in the number of nodes affected the propagation time over the biventricular model, delaying it by 1 ms. This was evidenced by analyzing the activation time of various nodes both at the apex and the base of the LV. To avoid altering subsequent results, it was decided to retain this reduced

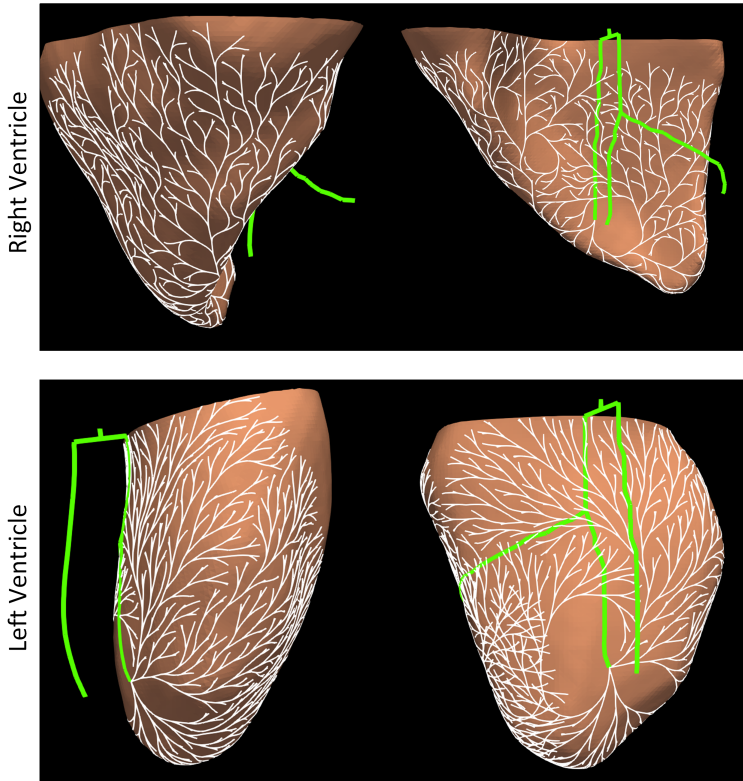


Figure 3.3: Distribution of the Purkinje network on the endocardial surface of both ventricles, shown with white lines. The main branch and its division towards the ventricles are highlighted in green.

Purkinje network for both the control and pathological simulated models.

For the PMJ that eventually make contact with the endocardial surface, a radius of 0.1 cm was selected around the PMJ, and all ventricular endocardial surface nodes within this circle were chosen as contact nodes for the application of the electrical stimulus (see Fig. 3.4). The different anisotropic conductivities in the ventricular myocardium and the His-Purkinje were adjusted using appropriate diffusion coefficients and set to result in a longitudinal CV of 67 cm/s in the myocardium and of 2.5 - 3.0 m/s in the His-Purkinje system, respectively.

The CV between the Purkinje tree and the PMJs that contact the endocardial surface was reduced to smooth the transition to the cardiac tissue. The cellular membrane kinetics of the Purkinje network were represented by the Stewart AP model [20] and the human ventricular cell electrophysiology by the ORd model for healthy tissue [25].

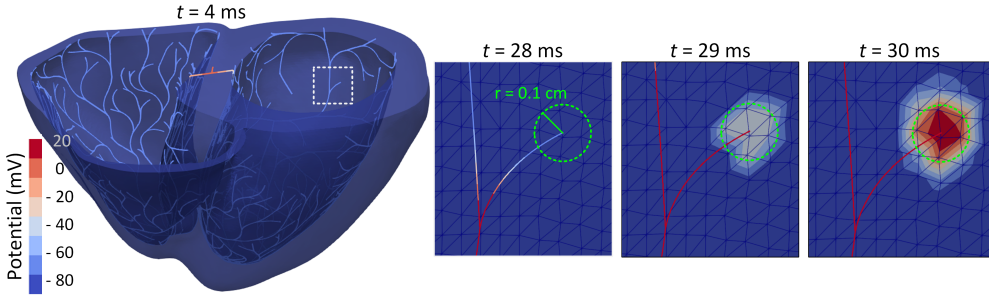


Figure 3.4: Each PMJ of the Purkinje network connects to the endocardial surface with the nodes located within a radius of 0.1 cm. The propagation can be seen starting from the bundle of His ($t=4$ ms), and on the right, the propagation from $t=29$ ms to $t=30$ ms is shown through the selection of nodes on the endocardial surface.

3.1.2 Fiber architecture

Another factor that influences the propagation of the AP and is important to incorporate into simulations is the direction of the potential's propagation. The computational models' mesh is made up of nodes, which are the basic elements of the propagation structure, and each requires proper orientation to realistically represent a cardiomyocyte. Determining fiber orientation in a patient poses a challenge that limits *in silico* model customization. However, there are two main ways to incorporate this information: using *ex vivo* fiber maps [102] or rule-based methods [103–105].

For this research, we used the algorithm proposed in [104] to determine fiber orientation on the endocardial surfaces of the RV and LV and the entire epicardial surface.

The algorithm establishes a local coordinate system to determine the direction of a 3D unit vector for each mesh node. This system consists of longitudinal (\hat{e}_l), transmural (\hat{e}_t), and circumferential (\hat{e}_c) axes. The first two axes are defined by solving the Laplace equation using the model's defined surfaces as Dirichlet boundary conditions, and by calculating the solution gradient. The circumferential axis is defined as the cross product of the transmural and longitudinal axes.

The transmural direction ($\nabla\Phi$) is obtained by solving the Laplace equation between the endocardial and epicardial surfaces of each ventricle, and by calculating the gradient of the solution. Dirichlet boundary conditions assign $\Phi = -2$ for the endocardium of the LV, $\Phi = 1$ for the endocardium of the RV, and $\Phi = 0$ for the epicardium:

$$\nabla^2\Phi = \begin{cases} 0, & \text{on } \Gamma_{\text{epi}} \\ 1, & \text{on } \Gamma_{\text{RV endo}} \\ -2, & \text{on } \Gamma_{\text{LV endo}} \end{cases} \quad (3.1)$$

The longitudinal direction ($\nabla\Psi$) is computed from apex to base, considering a biventricular model. Dirichlet boundary conditions are set with $\Psi = 0$ at the base and $\Psi = 1$ at the apex:

$$\nabla^2\Psi = \begin{cases} 0, & \text{on } \Gamma_{\text{base}} \\ 1, & \text{on } \Gamma_{\text{apex}} \end{cases} \quad (3.2)$$

Using the computed gradients, the local coordinate system for each node of the mesh is obtained as follows:

$$\hat{e}_l = \frac{\nabla\Psi}{\|\nabla\Psi\|}, \quad \hat{e}_t = \frac{\nabla\Phi - (\hat{e}_l \cdot \nabla\Phi)\hat{e}_l}{\|\nabla\Phi - (\hat{e}_l \cdot \nabla\Phi)\hat{e}_l\|}, \quad \hat{e}_c = \hat{e}_l \times \hat{e}_t. \quad (3.3)$$

Finally, the rotation process for each vector associated with the mesh nodes is performed by rotating the coordinate system in the following way: the vector \hat{e}_c rotates counterclockwise around \hat{e}_t by an angle α .

$$\alpha = \alpha_{\text{endo}}(w) \cdot (1 - d) + \alpha_{\text{epi}}(w) \cdot d, \quad (3.4)$$

where d represents normalized transmural depth between 0 and 1. The value of w is obtained from an intraventricular interpolation function that guides the fiber direction between apex-base within the ventricle. The values of α_{endo} and α_{epi} were chosen following the Streeter rule from apex to base in a counterclockwise direction, ranging from -60° on the endocardium to 60° on the epicardium for both ventricles [21].

The second rotation involves the vector \hat{e}_c rotating counterclockwise around \hat{e}_l by a transverse angle β , defined by the following equation:

$$\beta = \beta_{\text{endo}}(w) \cdot (1 - d) + \beta_{\text{epi}}(w) \cdot d. \quad (3.5)$$

In our study, we selected values of RV $\beta_{\text{endo}} = 120^\circ$, $\beta_{\text{epi}} = 180^\circ$, and for the LV: $\beta_{\text{endo}} = 180^\circ$, and $\beta_{\text{epi}} = 0^\circ$.

The process of preparing the files for the application of the proposed algorithm involved several preprocessing stages, which were semi-automated as

follows. We began with the biventricular model meshed with 4 nodes tetrahedral elements. Next, labels were applied to specific points on the cardiac model surface to set Dirichlet conditions and generate the local reference system. These surfaces included the left and right endocardium, and the left and right apex. This selection and labeling were done manually using Paraview software. Four **.xlsx* files containing the node list for each identified region were generated. From there, we developed a MATLAB based pipeline with the following stages:

- Biventricular model input: We first imported the biventricular model (**.mat*), ensuring only the coordinate and connectivity matrices were defined. Additionally, the output file directory was specified.
- Border identification: We then imported the **.xlsx* files containing the node lists for each identified region: RV endo and apex, and LV endo and apex. This stage generates an initial mesh model with the identified border regions (see Fig. 3.5 a).
- Surfaces detection: This process generated a second one mesh file, which identified five groups of nodesets: the epicardial surface, the entire model surface (all_{surf}), the endocardial surfaces of the right and left ventricles, and myocardium, corresponding to all remaining nodes outside the surface ($\Omega - \text{all}_{surf}$) (see Fig. 3.5 b - f). With this file, we can execute Doste's algorithm [104] to generate a mesh file with an attribute corresponding to the fiber orientation field at each node (see Fig. 3.5 g).

This MATLAB tool was developed to reduce testing time, as the research involved multiple trials that required modifying anatomical meshes and consequently generating fiber directions to simulate electrophysiological propagation. For this reason, we included three additional options:

- The first additional option allowed for incorporating study regions that can be labeled and included in the generated model, done by manually selecting nodes in Paraview, generating an **.xlsx* file.
- The second option generates model files with **.inp* and **.vtk* extensions. The former is necessary for working in ELECTRA, and the latter is useful for viewing all model details graphically in Paraview.
- The third additional option allows generating a **.json* file that includes the names of the generated files, identified subregions, and also incorpo-

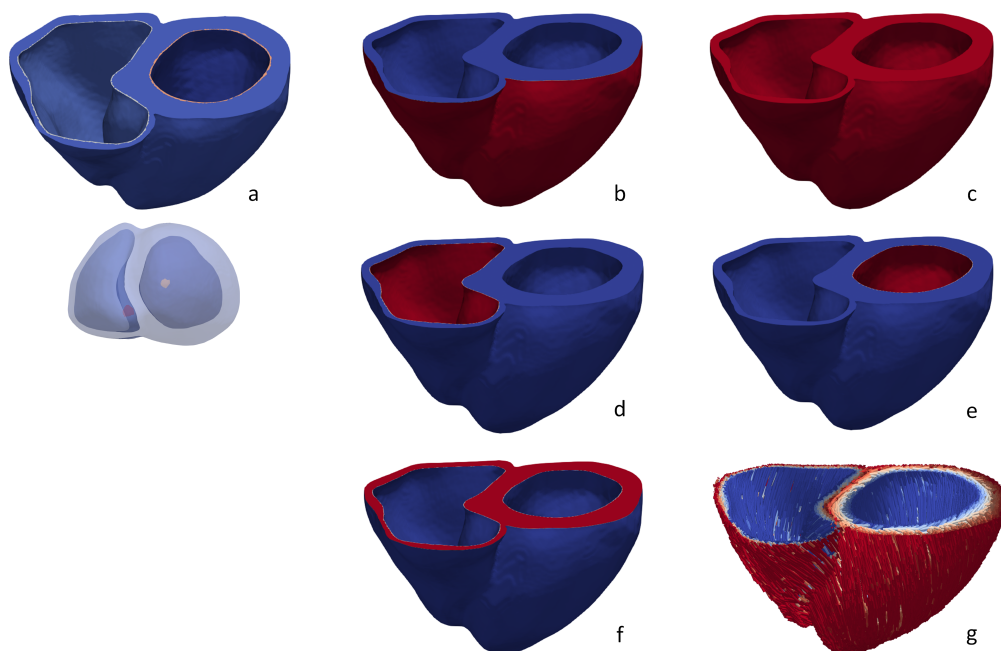


Figure 3.5: a: Right and left ventricular borders and apex labeled for fiber direction generation algorithm import, b: Detected epicardial surface, c: Complete model surface, d: RV endocardium, e: LV endocardium, f: Myocardium of the model, g: Fiber orientation per node from endocardium to epicardium.

rates fiber data. Parameters configured in this file are detailed in the Section 2.2.2.

In ELECTRA, the longitudinal axis, aligned with the fibers, was configured for faster propagation than along the transverse axis. The propagation ratio between these two axes was set at 4:1. A sequence of three stimuli, separated by 1000 ms, was applied to generate electrical activity in the ventricles. The stimuli consisted of a square impulse with an amplitude of 200 mA and a duration of 0.5 ms. The third beat was used for analysis.

3.2 Transmural and apicobasal heterogeneities modeling intersubject variability

Computational simulation of the electrical activity in the human heart continues to incorporate parameters that enable a closer representation of this complex biological system. Despite these advancements, biological systems exhibit subject-specific characteristics, posing a significant challenge to *in silico* representation for the ongoing development of computational simulation. Nevertheless, this challenge is well received in the simulation field, as it allows for the representation of numerous pathological or histological scenarios. High-performance computing systems facilitate advanced simulations, reducing computational time. Among the various inter-subject characteristics present in cardiac electrophysiology, we chose to focus on two primary factors in this research project: the inclusion of transmural heterogeneities through cardiac tissue segmentation into endocardium, mid-myocardium, and epicardium regions, and adjustments to the apico-basal propagation speed of the slow potassium current I_{Ks} .

3.2.1 Endo-, mid-, and epi-cardium segmentation

In the development of this research project, transmural heterogeneities were incorporated into the biventricular model by segmenting the cardiac tissue into three groups: endocardium, mid-myocardium, and epicardium. Each of these three subregions in the biventricular model was represented using the ORd for healthy human ventricular cell electrophysiology [25]. The primary differences among the endo, mid, and epi models are due to variations in ionic parameters, which lead to differences in APD. In the endo and mid models, the transient outward potassium current (I_{to}) is less pronounced, resulting in a slower repolarization compared to the epi model. Additionally, the slow (I_{Ks}) and rapid (I_{Kr}) potassium rectifier currents are less dense in the endo and mid cells, leading to a prolonged AP. In contrast, the epi model, with higher I_{Kr} and I_{Ks} density, allows for a more rapid repolarization. Midmyocardial cells exhibit the highest late sodium current (I_{NaL}), along with reduced I_{Kr} and I_{Ks} , leading to the longest APD of the three. Endocardial cells exhibit intermediate levels of these currents and APD [25].

In Fig. 3.6, the results of a 2D surface simulation are shown, using square mesh elements with a side length of 1 mm. A stimulus of 200 mA was applied at $t=0$ ms with a duration of 0.5 ms, targeting a group of 4 nodes located in the bottom left corner of the model. The simulation of AP propagation was

conducted using FEM, and three simulations were performed: in the first, the entire surface was represented as epi cells, in the second as endo cells, and in the third as mid cells. A monodomain model was used for these simulations, and the AP was evaluated at 60, 100, 200, and 300 ms. Additionally, on the right side of the figure, the differences in amplitude and duration across the three simulated ORD are shown, taking an intermediate point of the mesh located in the lower-left quadrant of the surface.

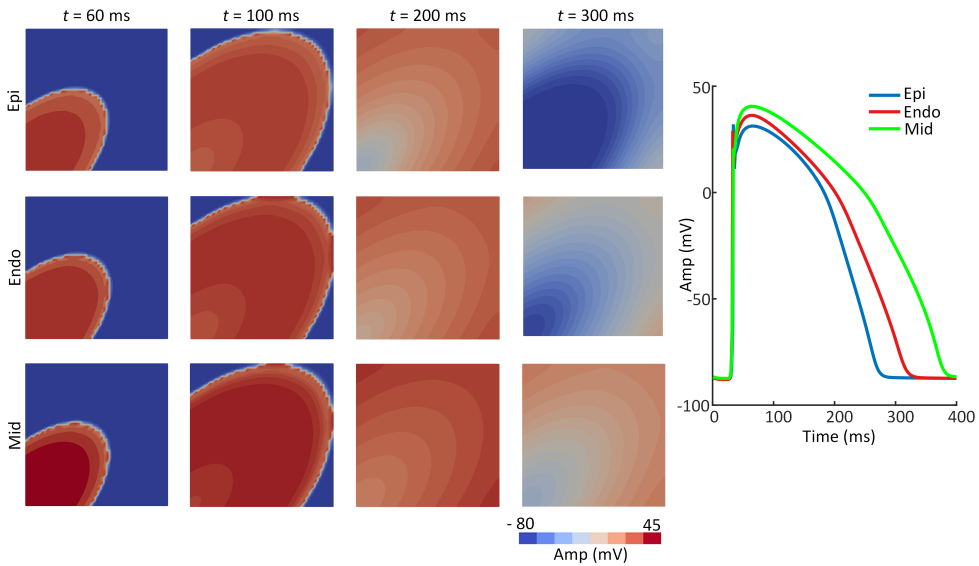


Figure 3.6: Simulated AP on a 2D surface represented as epi, endo, and mid tissue at $t=60$, 100, 200, and 300 ms. On the right, the AP is shown on a node with the entire surface modeled as epi, endo, and mid cells.

The spatial distribution of transmural heterogeneity in membrane kinetics was modelled by incorporating distinct endo-, mid-, and epi-cardial cell layers with varying relative thicknesses. The full width of the cardiac wall was divided into three regions modeled as endo, mid, and epi. The division percentages were varied in different decile proportions to assess their impact on the electrophysiology of the study. Each configuration was denoted as $Cuvw$ where u , v and w denote the first digit (decile) of the percentage proportions of endo-, mid- and epicardial cells, respectively, $u + v + w = 10$, (e.g. C334 represents the case with 30% endo-, 30% mid- and 40% epicardial cells).

We identified three surfaces on the mesh model, the left and right ventricular endocardial surfaces and the epicardial surface. From the k -th node in the mesh, located at coordinates $\mathbf{n}_k = [x_k \ y_k \ z_k]$, we selected those which

corresponded to the ventricular endocardial surfaces, \mathbf{n}_{ken} , k_{en} belonging to the subset of $\{k \in endo\}$, and looked out for the nearest point in the epicardial surface \mathbf{n}_{kep} , k_{ep} in the subset $\{k \in epi\}$, by determining the minimal Euclidean distance, $D_m(k_{en})$, between two nodes as

$$D_m(k_{en}) = \min_{k_{ep}} \left\| \begin{bmatrix} x_{ken} & y_{ken} & z_{ken} \end{bmatrix} - \begin{bmatrix} x_{kep} & y_{kep} & z_{kep} \end{bmatrix} \right\|. \quad (3.6)$$

A proportion, p_{en} , of the nodes in the $D_m(k_{en})$ transmural section from endo to epi, departing from endo, were set to endocardial nodes. Another proportion, p_{epi} , of those departing from epicardium were set to epicardial nodes. Those in middle were considered as midmyocardial nodes. This was implemented by considering a sphere with center in $\begin{bmatrix} x_{ken} & y_{ken} & z_{ken} \end{bmatrix}$ and radius $r_{en} = p_{en} \times D_m(k_{en})$. Every node inside the sphere was classified as an endocardial node. This process was repeated for the epicardial nodes (see Fig. 3.7).

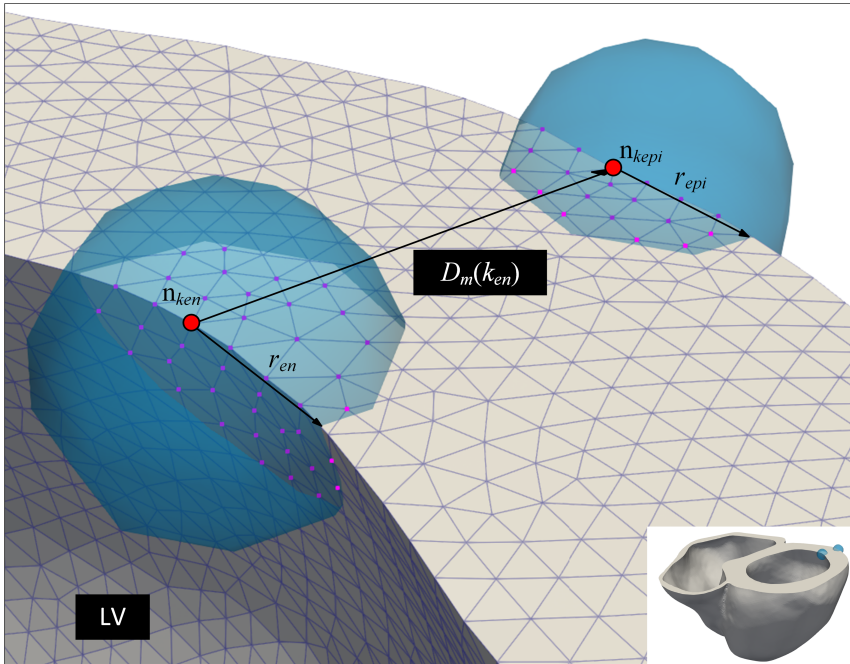


Figure 3.7: Representation of the algorithm for dividing cardiac tissue into endo, mid, and epi. The red circles represent nodes \mathbf{n}_{ken} and \mathbf{n}_{kepi} ; their distance is calculated and then divided into percentages according to r_{en} and r_{epi} , which are the radius of the spheres within which the nodes are selected as endo or epi.

The implementation of this algorithm was carried out in MATLAB, and in its initial version, it was performed by sweeping the entire LV endocardial surface, then the RV, and finally the epicardial surface. This algorithm functioned correctly as long as an additional file was included indicating the mesh nodes corresponding to the septum. This information was generated when applying the Laplace equation on the endocardial surfaces to determine fiber orientation (see Section 3.1.2), where the nodes of the RV and LV were clearly identified.

Regarding the interventricular septum, we tested the inclusion of a mid-myocardial region, but it introduced pronounced repolarization gradients that distorted the morphology of the precordial T waves. Then, When the septum was modeled as a single endocardial region, T-wave shapes in the precordial leads returned to within physiological ranges.

Once the heterogeneities were set, the region-detection algorithm was optimized starting from the epicardial surface. From this surface, for each node comprising it, the closest endocardial node, either from the left or RV, was identified, and the Euclidean distance to this node was measured. This distance $D_m(k_{epi})$ was then divided into 10 partitions by using a parameter $p_{epi} \in \{0.1, 0.2, \dots, 0.9\}$.

Next, a sphere was defined with its center at $[x_{k_{epi}} \ y_{k_{epi}} \ z_{k_{epi}}]$ and radius $r_{epi} = p_{epi} \times D_m(K_{epi})$, and all nodes within this sphere were considered as epi nodes. After executing this algorithm, we obtained a file listing the epi nodes for spheres of 10, 20, 30, \dots , 90% of $D_m(k_{epi})$, which was then used to generate additional models with different tissue segmentation. With this algorithm, any combination of endo, mid, and epi tissue can be automatically generated, restricting $u + v + w = 10$.

Once we had the epi file, we were able to generate different models with varying endo, mid, and epi assignments more quickly. However, as this project stage aimed to represent a wide range of tissue combinations to understand their impact on the ECG, we adapted the aforementioned algorithm for execution on the high-performance cluster provided by the Aragón Institute for Engineering Research (I3A) at the University of Zaragoza. For algorithm execution, two external files were required: the first containing the original mesh, including the node coordinates, the connectivity matrix, and subgroups indicating the nodes belonging to the RV and LV located on the endocardial and epicardial surfaces; and the second file listing the different percentages of $D_m(k_{epi})$ ¹.

¹The code requires four input arguments: the model combination name, w (epi percentage), and a parameter u_{aux} (sum of the mid and epi percentages), both used in the $D_m(k_{epi})$

A total of fifteen configurations were developed considering variations from 10% to 30%, in steps of 10%, in the midmyocardial, and this paired with all possible combinations from 10% to 50% in the endocardial, and 20% to 80% in the epicardial segment, restricted transmurally to sum up to 100%

3.2.2 Incorporation of apex-to-base heterogeneity

Apex-to-base electrophysiological heterogeneities were introduced in the model. The variability in electrophysiological behavior within myocardial tissue has been reported in both animals and humans, with changes observed in I_{to} , the I_{Na} , and the I_{Kr} and I_{Ks} currents [106, 107]. The variability present during the repolarization phase and APD along the ventricular walls has been associated with heterogeneity in the relative densities of I_{Kr} and I_{Ks} [106].

To capture the longer APD observed at the base compared to the apex, we scaled the conductance of the slow delayed rectifier potassium current (G_{Ks}) [108], who reported significant differences in the expression levels of proteins forming the I_{Ks} channel between the apical and basal regions of the heart. The conductance value of I_{Ks} , prior to introducing the apex-to-base scaling factor, was adopted from the human model by ORD, where the ratio of G_{Ks} for epi/endo is 1.4 and mid/endo is 1 [25].

The biventricular human model was divided into three regions along the apex-to-base direction: apex, middle, and base to account for the longer APD at the base compared to the apex. For this division, we consider the longitudinal coordinate variable ζ , moving in the apex to base direction, for each node \mathbf{n}_k , $\zeta_{\mathbf{n}_k}$. The minimum (ζ_{min}) and maximum (ζ_{max}) values of the model nodes along the longitudinal base-to-apex axis were considered and the longitudinal distance \mathcal{L} defined as $\mathcal{L} = \zeta_{max} - \zeta_{min}$. The threshold value between the regions was calculated as $\zeta_{th} = \mathcal{L}/3$, and the mesh nodes were subsequently classified in three regions \mathcal{R}_{apex} , \mathcal{R}_{middle} and \mathcal{R}_{base} according to the following definitions:

percentage file. These parameters enable quick identification of elements belonging to the endocardial (endo), mid, and epicardial layers. For instance, to generate a model with 40% endo, 10% mid, and 50% epi distribution across the ventricular wall, the input should be $w = 50$ and $u_{aux} = 60$. From these, it is straightforward to determine that epi region will be 50%, endo will be $100 - u_{aux} = 40\%$, and the mid region will be the remaining 10%.

$$\begin{aligned}
\mathcal{R}_{apex} &\equiv \{\mathbf{n}_k \mid \zeta_{min} \leq \zeta_{\mathbf{n}_k} \leq \zeta_{min} + \zeta_{th}\}, \\
\mathcal{R}_{middle} &\equiv \{\mathbf{n}_k \mid \zeta_{min} + \zeta_{th} < \zeta_{\mathbf{n}_k} \leq \zeta_{min} + 2\zeta_{th}\}, \\
\mathcal{R}_{base} &\equiv \{\mathbf{n}_k \mid \zeta_{min} + 2\zeta_{th} < \zeta_{\mathbf{n}_k} \leq \zeta_{max}\}.
\end{aligned} \tag{3.7}$$

Nodes at each region were assigned a distinct factor that contributed to the reduction of G_{Ks} , leading to a variation in I_{Ks} magnitudes. Specifically, G_{Ks} was reduced with a distinct scaling factor: 5 at the apex, 2.6 in the middle, and 0.2 at the base [109]. This segmentation resulted in an ECG that closely resembles a physiological ECG, as shown in Fig. Fig. 3.8. Other strategies, such as implementing linear gradient transitions, are not expected to significantly affect T-wave morphology, as cell-to-cell coupling through gap junctions tends to attenuate sharp transitions. Nonetheless, this strategy will be incorporated in future work.

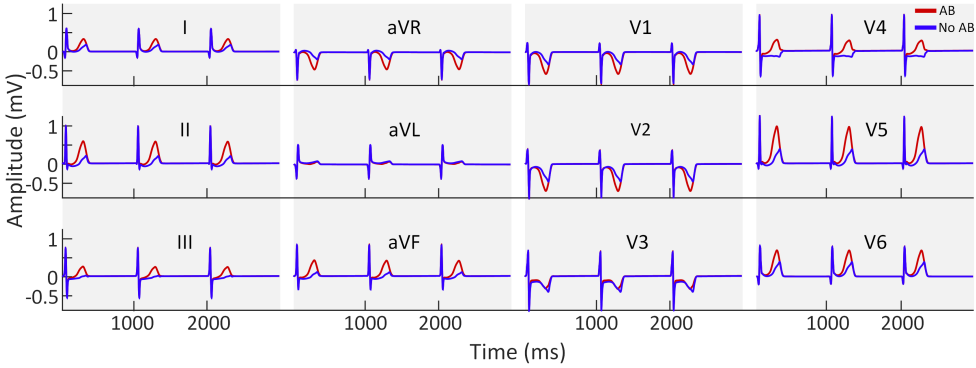


Figure 3.8: Pseudo ECG from the simulation of 3 heartbeats on a biventricular model, showing the effect of incorporating apex-to-base heterogeneities in red compared to the simulation without apex-to-base heterogeneities in blue.

This new grouping of nodes was introduced into the algorithm detailed in Section 3.2.1 for the incorporation of transmural heterogeneities, so that the nodal subgroups were automatically generated. The biventricular model was ultimately divided into 9 regions, taking into account the previously detailed transmural and apex-to-base heterogeneities, as shown in Fig. 3.9. These characteristics were used in all the models generated in this research.

In Fig. 3.10, the effect of incorporating apex-to-base heterogeneities on the propagation of the AP along a 2D surface, meshed with square elements of 1 mm per side, is shown. In this figure, it can be observed that in the apex

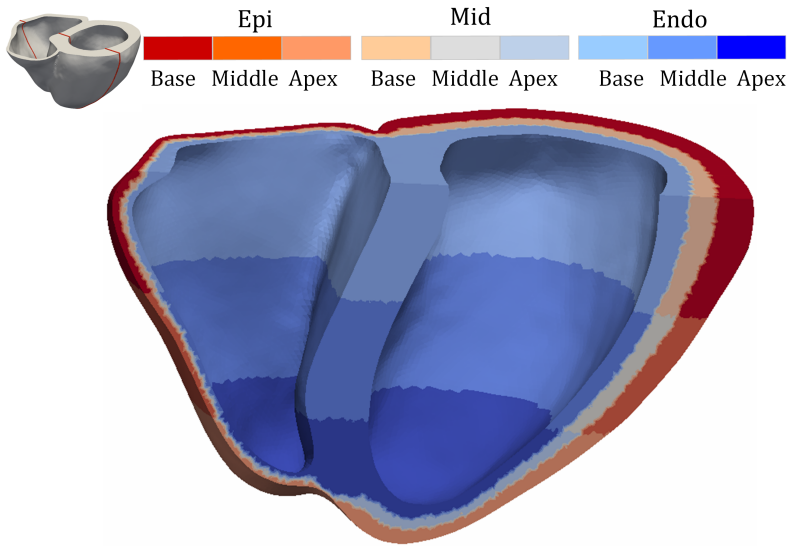


Figure 3.9: Biventricular human model with incorporated transmural and apex-to-base heterogeneities.

region there is a higher density of I_{Ks} , which results in a faster repolarization phase. In the middle region, the repolarization phase is accelerated, although to a lesser extent than in the apex. Finally, in the base region, the repolarization phase is prolonged due to the slowing effect introduced in G_{Ks} .

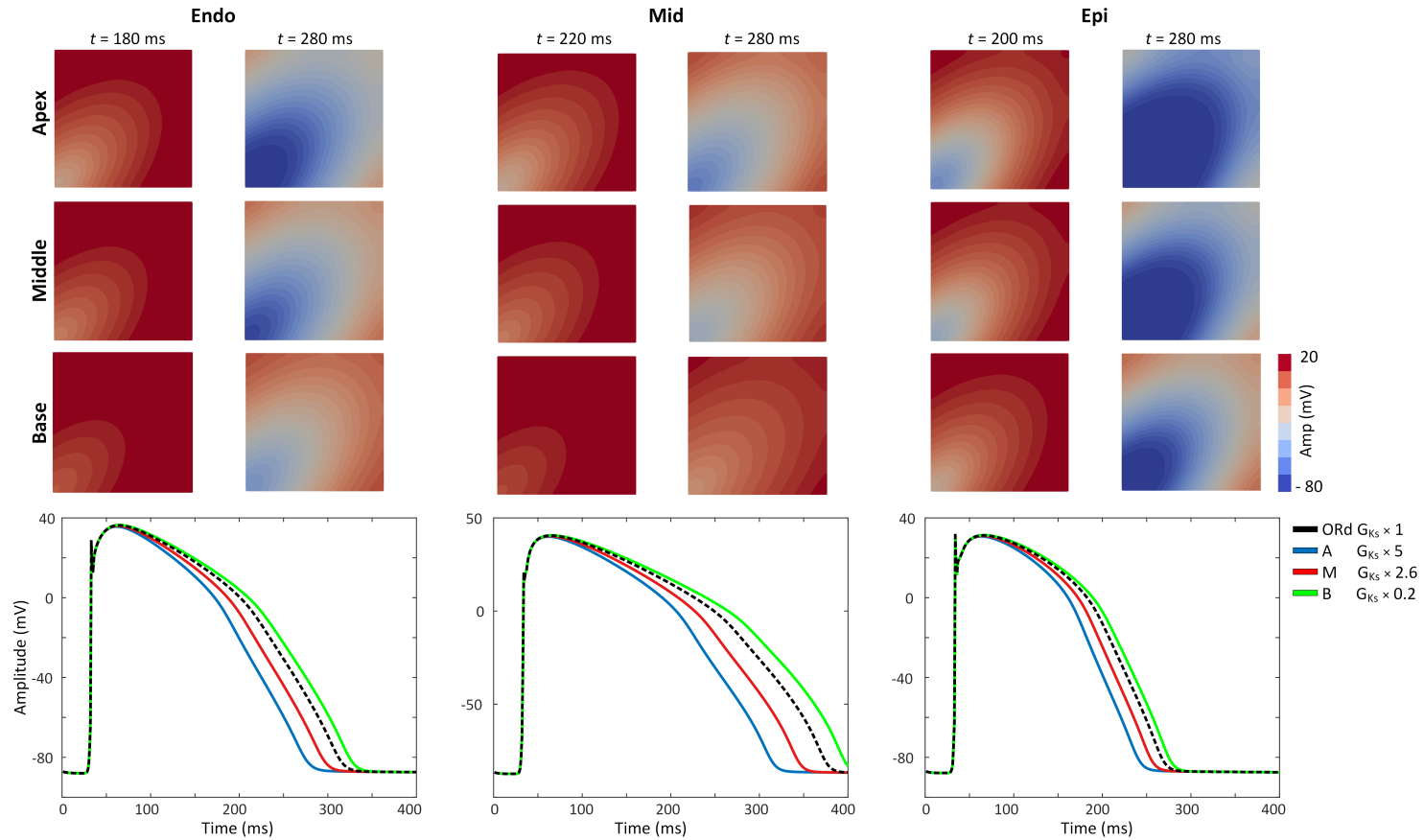


Figure 3.10: Propagation of the AP along a 2D surface at time $t=180$ and 280 ms for endo tissue, $t=220$ and 280 ms for mid tissue, and $t=200$ and 280 ms for epi tissue. On the bottom, the AP curve is shown for endo, mid, and epi tissue. The reference curve from the human model by ORd, without scaling, is added in black.

This scaling represented a significant change in the 12-lead ECG simulation on the biventricular human model, particularly during the repolarization phase, as shown in Fig. 3.8. The incorporation of this scaling factor allowed for a more realistic pseudo-ECG.

3.2.3 Generation of globular models

The anatomical changes resulting from IUGR (see Section 1.5.1) have lasting consequences into adulthood, as demonstrated by several studies (see Table 1.1). Cardiovascular remodeling can manifest as a reduction in the ventricular SpI defined as the ratio between the base-to-apex length, \mathcal{L} , to the basal diameter (ϕ), $\text{SpI}=\mathcal{L}/\phi$, and these changes have been shown to be more prominent in the LV. They may even be associated with an increased risk of mortality in adulthood [110].

The models introducing deformation changes emulating the IUGR globular cardiac morphologically remodeling are denoted as \mathcal{G} models, and built departing from the control model \mathcal{C} . To build \mathcal{G} from \mathcal{C} , we incorporated echocardiographic findings on left and right ventricular morphometry as reported in [13]. Specifically, we increased the basal diameter ϕ and shortened the apex-base length \mathcal{L} , resulting in a reduction of the SpI (see Table 3.1). In order to focus the study on evaluating the impact of geometrical changes on the simulations, the electrophysiological characteristics of the \mathcal{G} model, such as fiber orientation, ventricular heterogeneities, and CV, were kept unchanged with values as previously described in the control model.

To deform the \mathcal{C} model, we used FEBIO software and the cardiac tissue was modeled as an isotropic, homogeneous, hyperelastic, and incompressible Mooney-Rivlin material [111] with an invariant term $C1=0.38$ MPa and $C2=0.31$ MPa. Nodes, $\mathbf{n}_k = [x_k \ y_k \ z_k]$ were deformed, generating a nodal displacement to $\mathbf{n}_k + \mathbf{d}_k$, with $\mathbf{d}_k = [u_k \ v_k \ w_k]$.

We generated eight distinct deformed models \mathcal{G} with the same SpI (Fig. 3.11). We first applied three different strategies to increase the ϕ of the control geometry by applying a load on the Y -axis (where ϕ is measured) resulting in a displacement $f_y(y_k)$ on the y_k coordinate: $\mathbf{d}_k = [0 \ f_y(y_k) \ 0]$.

- The first strategy, denoted as ($Y \rightarrow$), expanded the epicardium of the LV by applying a surface traction on the epicardial surface with a boundary condition $f_y(y_k) = 0$, no displacement, for y_k in the septum nodes.
- In the second strategy, we applied a similar load on the septal left wall

Table 3.1: Base-apex length \mathcal{L} , basal diameter ϕ , and sphericity index SpI feature values from echocardiographic measurements, with statistical difference between patient groups, [13] and the same morphometry measurements in the simulations models \mathcal{C} and \mathcal{G}_A to \mathcal{G}_H deformed models variants.

Data \ Feature		\mathcal{L} length (cm)		ϕ diameter (cm)		SpI	
		Left	Right	Left	Right	Left	Right
Clinical dataset	Control subjects	6.9±0.6	6.5±0.6	3.4±0.3	3.0±0.4	2.0±0.01	2.1(0.2-0.22)
	IUGR subjects	6.4±0.6	6.1±0.6	3.5±0.3	3.0±0.3	1.9±0.01	2.0(0.1-0.2)
	p-value	0.003	0.01	0.003	0.32	<0.001	0.006
Model	Control (\mathcal{C})	7.0	5.7	4.6	4.2	1.5	1.4
	\mathcal{G}_A [$Y \leftarrow, Z \uparrow$]	6.5	5.3	4.7	4.2	1.4	1.3
	\mathcal{G}_B [$Y \leftarrow, Z \downarrow$]	6.5	5.3	4.7	4.2	1.4	1.3
	$\mathcal{G}_{C, D}$ [$Y \leftarrow, Z \updownarrow$]	6.5	5.3	4.7	4.2	1.4	1.3
	\mathcal{G}_E [$Y \leftrightarrow, Z \uparrow$]	6.5	5.2	4.7	4.3	1.4	1.2
	\mathcal{G}_F [$Y \rightarrow, Z \downarrow$]	6.5	5.2	4.7	4.3	1.4	1.2
	$\mathcal{G}_{G, H}$ [$Y \leftrightarrow, Z \updownarrow$]	6.5	5.4	4.7	4.2	1.4	1.3

($Y \leftarrow$), $f_y(y_k) = 0$ for y_k in the left ventricular wall.

- In the third strategy, a similar load was homogeneously applied to the entire endocardial wall of the LV ($Y \leftrightarrow$),
 $\mathbf{d}_k = [f_x(x_k) \quad f_y(y_k) \quad 0]$, $f_x(x_k), f_y(y_k) = 0$ for x_k and y_k in the right ventricular wall.

We also applied three different strategies to reduce the \mathcal{L} length,

$$\mathbf{d}_k = [0 \quad 0 \quad f_z(z_k)].$$

- In the first strategy, a surface load ($Z \uparrow$) was applied to the apex, $f_z(z_k) = 0$ for z_k in the base.
- In the second strategy ($Z \downarrow$), the load was applied to the base, with $f_z(z_k) = 0$ for z_k in the apex.
- In the third strategy ($Z \updownarrow$), a scale factor, α , was introduced to homogeneously reduce the \mathcal{L} length, \mathcal{L}_{AB} , up to $\mathcal{L}_{AB} - \Delta\mathcal{L}_{AB}$, $\alpha = \Delta\mathcal{L}_{AB}/\mathcal{L}_{AB}$. We calculated the displacement on the Z -axis as $f_z(z_k) = \alpha(z_r - z_k)$, where z_r is the zero displacement reference coordinate. \mathcal{G}_G and \mathcal{G}_C models meet $f_z(z_r) = 0$ at the apex, and \mathcal{G}_H and \mathcal{G}_D models meet $f_z(z_r) = 0$ at the base (Fig. 3.11).

The surface loads were applied on each one of the triangle surface elements, resulting in a total displacement $\mathbf{d}_k = [u_k \quad v_k \quad w_k]$ formed by the summation

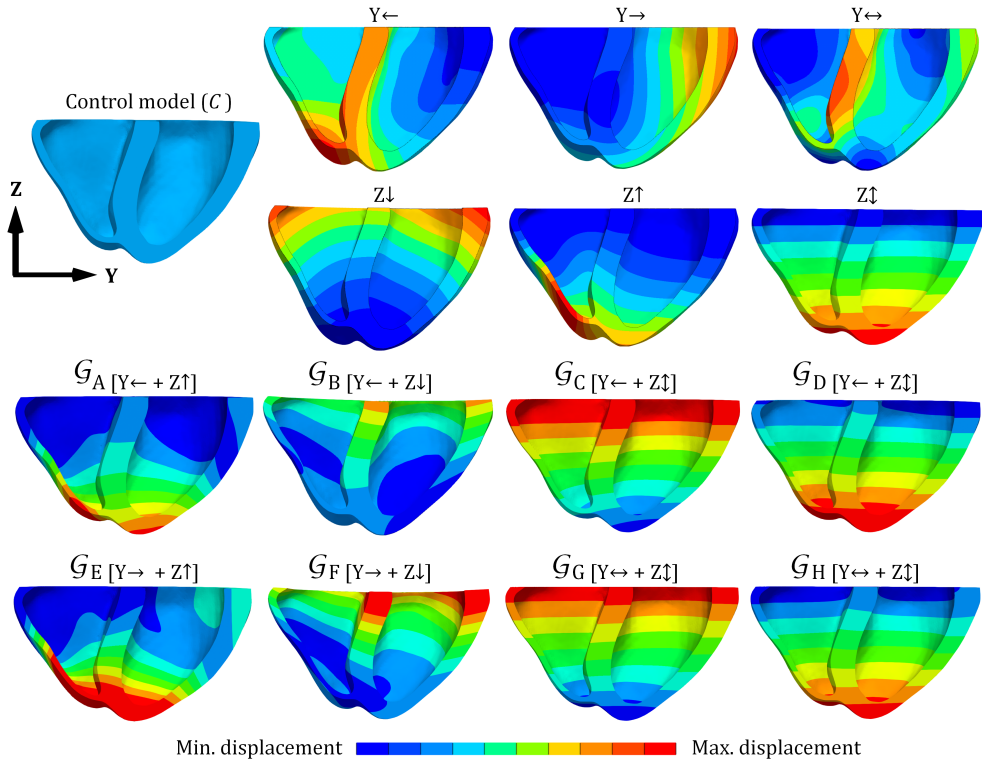


Figure 3.11: The upper part shows, through the color map, the nodal displacement obtained as a result of the deformation of the original control model \mathcal{C} . The Y and Z axes were associated with the deformation in the ϕ and in the \mathcal{L} , respectively. The eight \mathcal{G} models resulting from combining the deformations in Y and Z axes were shown at the bottom.

of the apex-base and endo-epi displacements, and applied to the original mesh to generate the eight \mathcal{G} models (Fig. 3.11). Twelve deformed models were obtained through the combination of the three methods for ϕ deformation with the four methods for apex-base deformation. Four models were excluded from the study as the angles of depolarization and repolarization they produced fell outside the physiological limits. This could be attributed to a less uniform distribution of deformation resulting from the combined methods of modifying ϕ and \mathcal{L} length. Fig. 3.11 displays the eight models that were retained for analysis.

3.3 Confounding effect of heart location within the torso

In addition to generating multiple globular models, we investigated the impact of a global displacement of the heart's anatomy relative to the thoracic cage, with a magnitude comparable to the deformation of the model nodes. This displacement, which can also account for electrode mispositioned, was incorporated by translating the original coordinate system of the biventricular mesh. This nodal displacement raised an important question: Is the electrophysiological change observed in the results just a result of the geometric remodeling, or could it be also attribute to the nodal displacement of the biventricular model, particularly the LV?

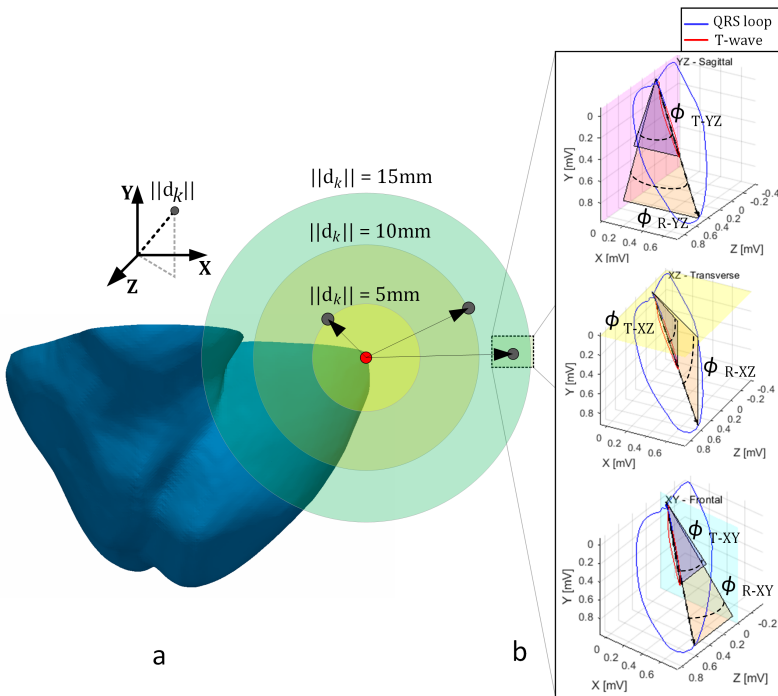


Figure 3.12: Displacement tests description for \mathcal{C} model, C334 configuration, when displacing mesh nodes by 5, 10, and 15 mm. a) location grid around a red point representing one node of the mesh and its relocation. Each gray point represents the displacement of each of the nodes of the model in any direction. 120 \mathbf{d}_k displacements were made around the original point, at 5, 10, and 15 mm. b) QRS and T-wave vectors and their angles with respect to the three corporal planes. Note that T-wave (red line) and QRS (blue line) loops have a similar dominant vector direction.

To answer this question, in addition to the morphological remodeling con-

sisting of a reduction in the SpI, a displacement of the heart anatomy within the thoracic cage was included. The \mathcal{C} model was relocated in the three axis in one hundred and twenty different forms, by displacing each node \mathbf{n}_k according to the vector $\mathbf{d}_k = [\Delta x \ \Delta y \ \Delta z]$ where $\|\mathbf{d}_k\| \in \{5, 10, 15\}$ mm (Fig. 3.12). The pseudo-ECG was computed considering the displacement of the biventricular model inside the torso mesh and the dominant vectors from the VCG were computed.

3.4 Pseudo ECG/VCG calculation from the biventricular human model

In the previous sections, all the features incorporated into the models for performing *in silico* simulations have been described. All simulations were carried out on both the control \mathcal{C} and globular \mathcal{G} models, maintaining similar propagation characteristics, heterogeneity, and fiber orientation, though adapting them to the geometric changes of the globular models. The features incorporated into the models are summarized in Fig. 3.13.

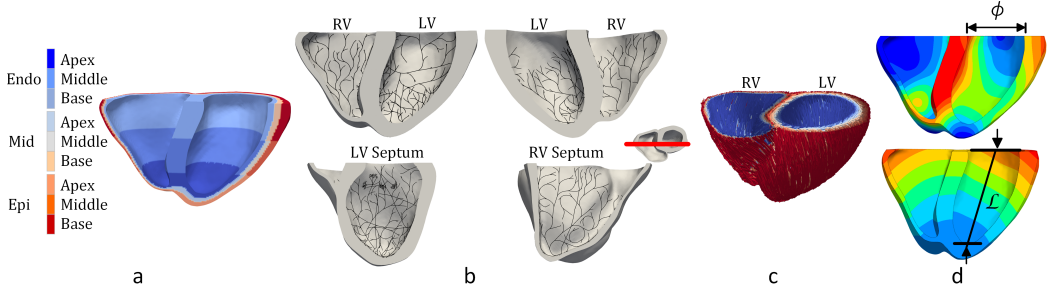


Figure 3.13: Parameters considered on the \mathcal{C} and \mathcal{G} models. a) Mesh segmentation considering transmural (endo/mid/epi myocardium) and gradient heterogeneities (apex/intermediate/base, dark blue to light blue), b) Purkinje network on the endocardial surface, c) fiber orientation from endocardial (blue lines) to epicardial surface (red lines), and d) color map showing the nodal displacement on the \mathcal{C} model to obtain the \mathcal{G} models.

The voltages in the biventricular mesh nodes and in the torso volume where it was embedded were used to compute extracellular potentials, using a monodomain cell model. Virtual electrodes were positioned on the torso surface at electrode positions required to compute the standard 12-lead ECG [112]. The torso volume consisted of $\sim 3\,250\,000$ nodes and $\sim 19\,500\,000$ tetrahedral elements. The torso structure and its position in space allow precise placement

of the heart within it, along with virtual electrodes on its surface to simulate the propagation of electrical activity through the volume and over the surface to calculate the ECG. Fig. 3.14 shows the torso and heart models, along with the electrodes and their spatial position. In this case, the \mathcal{C} model of the heart is displayed.



Figure 3.14: Heart model embedded in the torso with virtual electrodes on its surface (precordial leads V1 to V6 and limb leads RL, RA, LL, and LA).

We calculated the VCG from the synthetic ECG using the inverse Dower matrix [87], as described in Section 2.4.2. The projection of the QRS-T angle on the XY plane was calculated (θ_{RT-XY}). Three angles were determined between the QRS loop vector and each of the three VCG planes (ϕ_{R-XZ} , ϕ_{R-XY} , and ϕ_{R-ZY}), and other three for the T-wave vector (ϕ_{T-XZ} , ϕ_{T-XY} , and ϕ_{T-ZY}).

Finally, the angular difference between the QRS and T-Wave on each of the three planes was calculated ($\phi_{R-XZ}-\phi_{T-XZ}$, $\phi_{R-XY}-\phi_{T-XY}$, and $\phi_{R-ZY}-\phi_{T-ZY}$).

Fig. 3.15 shows the projection of the dominant depolarization and repolarization vectors of the VCG, obtained by simulating the \mathcal{C} model, in the three planes frontal, transverse, and sagittal. Additionally, the projection of the dominant vectors on the XY plane is illustrated. The loop observed corresponds to the third simulated heartbeat.

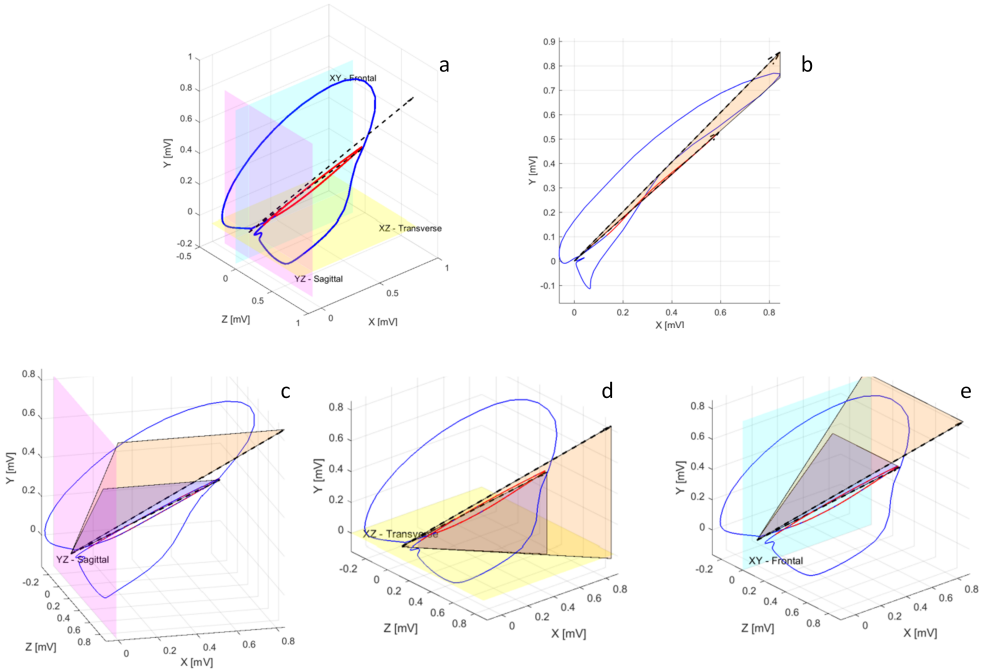


Figure 3.15: Loops and dominant vectors of depolarization and repolarization in the three reference planes: frontal, sagittal, and transverse. The QRS complex loop is shown in blue, and the T-wave loop is shown in red. The dashed line represents the dominant vectors of depolarization and repolarization. a: VCG and the three planes, b: Projection of the QRS vector onto the XY plane, with the angle highlighted in orange, c: Angles of the dominant vectors with respect to the YZ-Sagittal plane, d: With respect to the XZ-Transverse plane, and e: With respect to the XY-Frontal plane.

Three different stages were simulated for evaluation of the angular variables. First, simulations were performed in the control model \mathcal{C} incorporating transmural and apicobasal heterogeneities, as described in previous sections. Second, the control model was deformed to make the ventricles more globular \mathcal{G} using eight different strategies, \mathcal{G}_A to \mathcal{G}_H . Subsequently, different transmural

heterogeneities were incorporated in two representative deformed models, \mathcal{G}_G and \mathcal{G}_H . In the third stage, a global displacement test applied to the \mathcal{C} model was introduced by moving all mesh nodes equally.

3.5 Results

3.5.1 Transmural heterogeneities induced angular variation

Variability in the depolarization and repolarization VCG and ECG leads was introduced by using different transmural proportions of endo, mid and epi cells across the ventricular wall. The resulting X, Y, and Z leads are shown in Fig. 3.16. Dotted lines show the QRS and T-wave time intervals from which the dominant vectors were computed. The QRS complex was defined to occur between 12 and 85 ms, while the T-wave was considered to span from 200 to 378 ms. Fig. 3.16 shows the variation in the T-wave corresponding to different tissue heterogeneities for the fifteen simulated combinations described in the table inside Fig. 3.16.

The calculated angles of the QRS and T-wave loops with respect to the three corporal planes from different $Cuvw$ configurations were plotted in Fig. 3.17, leftmost boxplot in each angle column. The angles variance across the $Cuvw$ configurations were: in the frontal plane XY, 2.6° , 3.0° , and 3.7° for θ_{RT-XY} , ϕ_{R-XY} , and ϕ_{T-XY} , respectively; in the transverse plane XZ, 0.02° and 0.1° for ϕ_{R-XZ} and ϕ_{T-XZ} , respectively, and in the sagittal plane ZY, 2.1° and 1.7° for ϕ_{R-ZY} and ϕ_{T-ZY} , respectively.

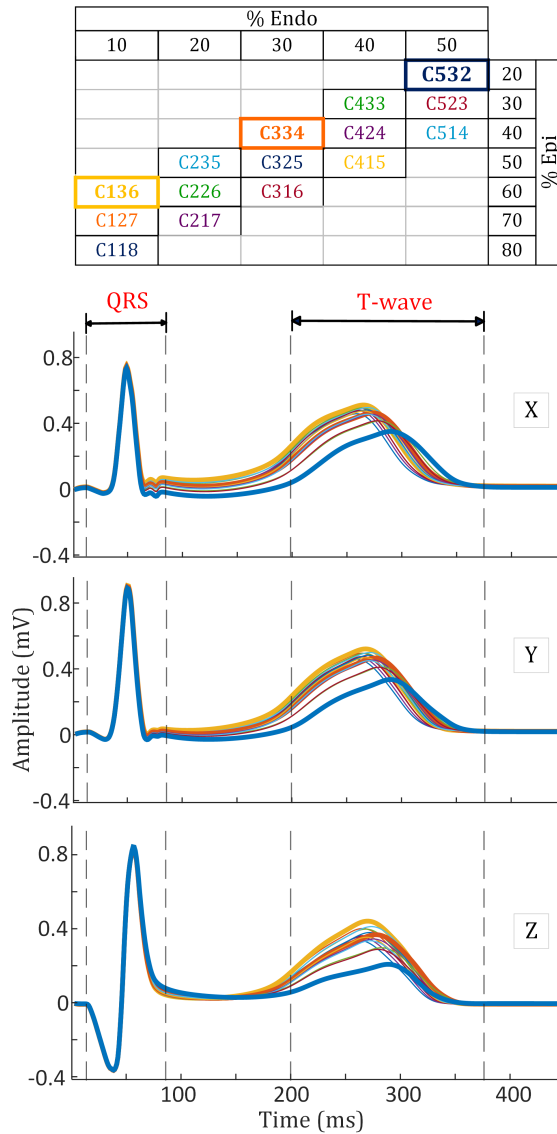


Figure 3.16: List of the different transmural tissue heterogeneities configurations. Columns and rows indicate the percentage of endocardium and epicardium respectively. Bold lines correspond to configurations with inter-middle (C334) and extremes (C136 and C532) T-wave amplitudes. X, Y, and Z leads computed using the biventricular model at the *C* case, combining different endo-mid-epi tissue ratios configurations, *C_{uvw}*. Dotted lines show QRS and T-wave time intervals from where the dominant vectors were computed.

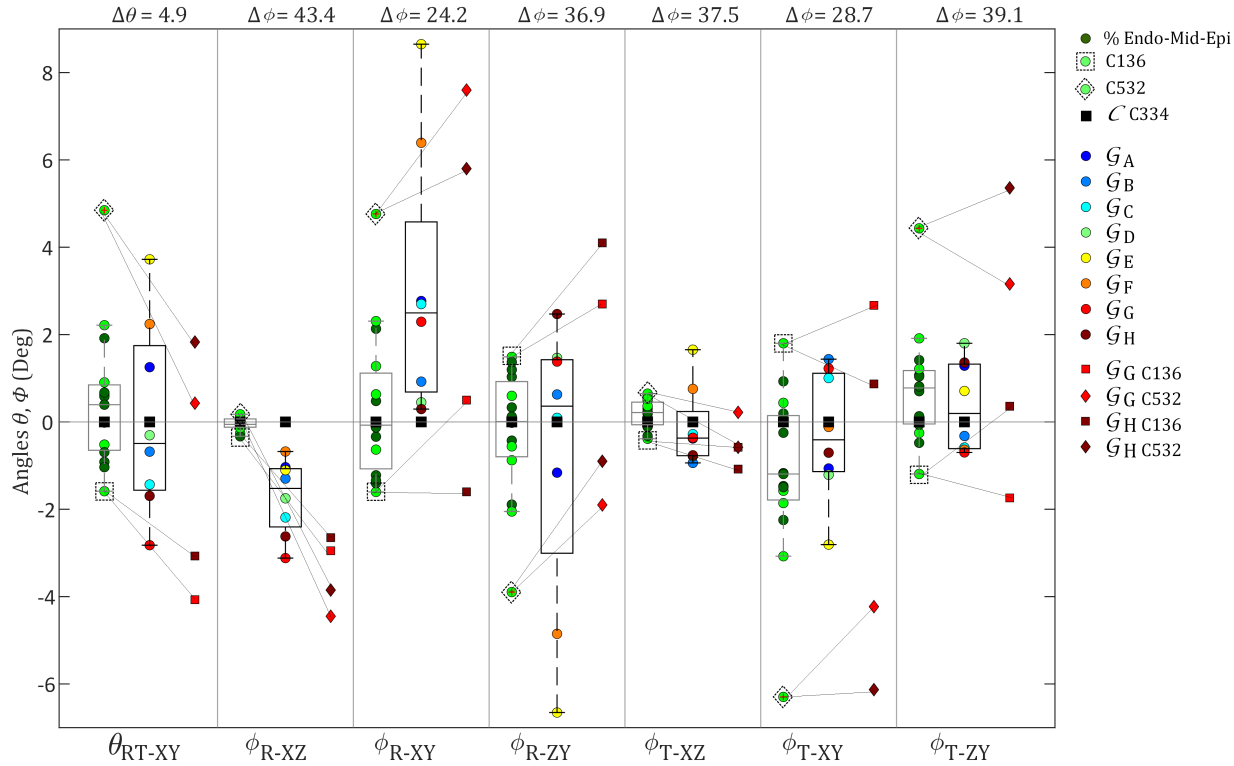


Figure 3.17: Depolarization and repolarization angles, plotted with a bias $\Delta\theta$ or $\Delta\phi$ reported on each column top, for visualization purposes. Each column corresponds to an angle and includes three subplots. The leftmost subplots include the angles estimate from \mathcal{C} case for the 15 different $Cuvw$ transmural configurations, representing the central configurations (endo having 20%, 30%, and 40%) in dark green, with percentiles boxplot, and in light green otherwise except the reference C334 which is plotted in black square; the two extreme cases of C136 and C532, were surrounded by square and diamond, respectively. The middle plots have eight colored dots, corresponding to angles estimated from the \mathcal{G}_A to \mathcal{G}_H models deriving from the control \mathcal{C} at transmural distribution C334 (black square). The rightmost subplot includes angles estimates for \mathcal{G}_G (red) and \mathcal{G}_H (brown) for the extreme transmural configurations C136 (squares) and C532 (diamond).

3.5.2 Angular variation in globular, \mathcal{G} , models

The eight deformed \mathcal{G} models, for C334 transmural distribution, exhibited varying QRS and T-wave angles with respect to the three VCG planes (Fig. 3.17, central columns), despite having a similar SpI. For each deformed model, we computed the QRS and T-wave loops. Subsequently, we derived the average QRS loop and the average T-wave loop across all the deformed models. The average loops were then compared to the loops of each deformed model using a least squares adjustment. As a result the \mathcal{G}_C and \mathcal{G}_G models exhibited the closest similarity to the average QRS loop, while \mathcal{G}_G and \mathcal{G}_H demonstrated the closest similarity to the average T-wave loop. Based on this observation, the \mathcal{G}_G and \mathcal{G}_H models were selected as the two representative deformed models for the study. The \mathcal{G}_G model shares the same ϕ deformation as the \mathcal{G}_H model but differs in its apex-base variation, allowing the two models to capture complementary features of cardiac deformation.

To analyze in detail the QRS loops changes, Fig. 3.18, we divided them into three colored segments: blue from loop start to 31 ms, gray from 31 to 64 ms, and magenta from 64 to 85 ms. We plotted the simulation results of the \mathcal{G}_G and \mathcal{G}_H models as representatives of average deformations. \mathcal{G}_G keeps an apex constraint as the reference point of deformation while \mathcal{G}_H keeps a base constraint.

In the first segment, the electrical propagation went from His bundle through the branches until the septum, discretely to the right, as can be evidenced in the frontal plane of the VCG (Fig. 3.18). Dominant vectors from \mathcal{G}_G and \mathcal{G}_H extended slightly towards the right side of the torso, probably due to the enlargement of the LV in the upper third septal myocardium and there was a slightly angular change in the sagittal and transverse planes. In the second segment of the loop, between 31 and 64 ms (Fig. 3.18), the electrical propagation in the LV predominated and the direction of the vector towards the lower left part of the torso can be observed. By decreasing the \mathcal{L} length in the \mathcal{G} models, the local activation time (LAT) of the region was reduced, causing a loop that reached its maximum point faster. After the potentials reached the apex, propagation continued into the large regions corresponding to the free walls of the LV. In the third segment of the loop, after 64 ms (Fig. 3.18), the last areas close to the base in the posterior area were mainly activated. In the globular \mathcal{G} models, the LAT was reduced on the base of the left and RV.

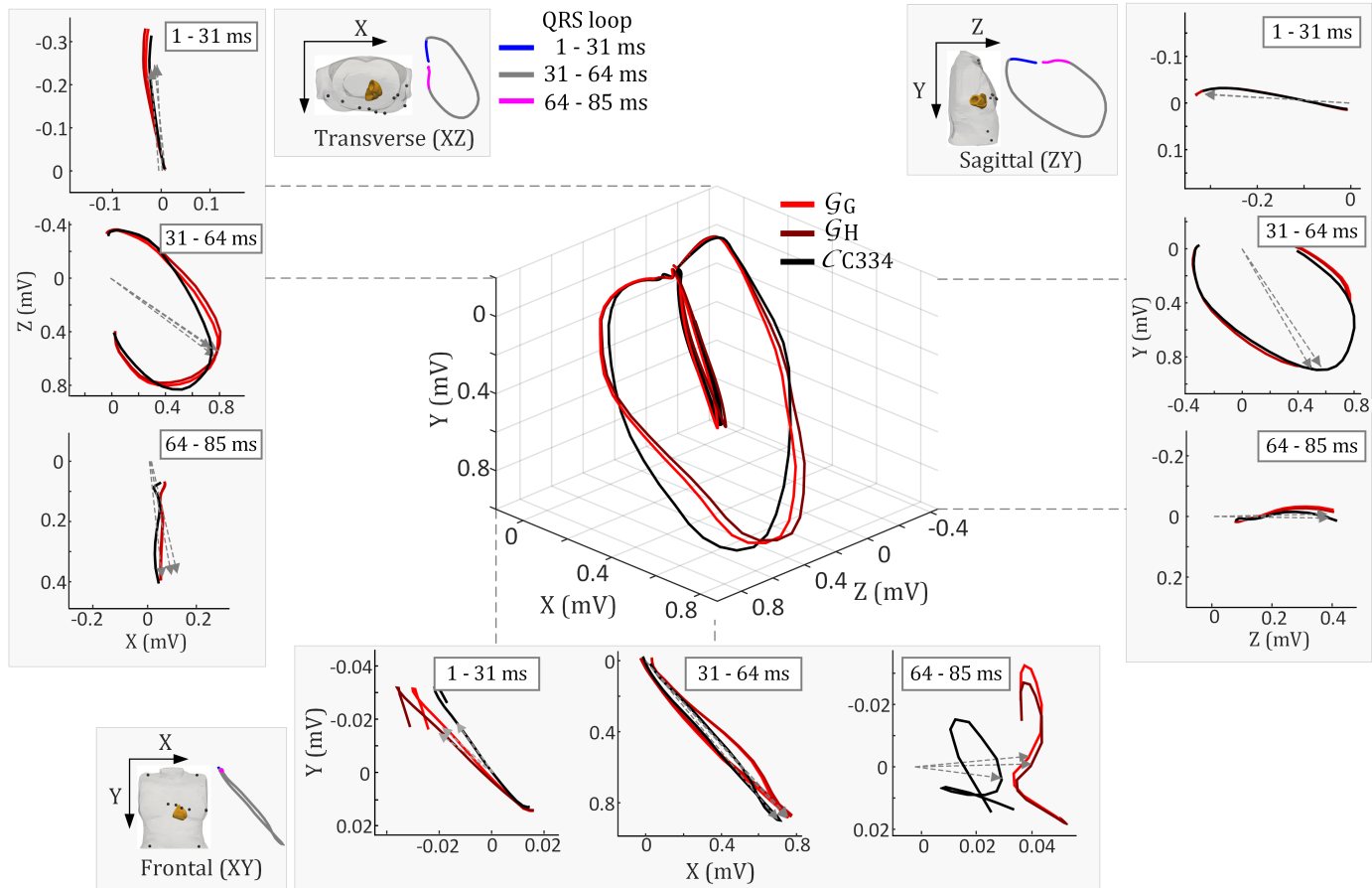


Figure 3.18: Temporal segmentation of the QRS loop in three parts to analyze the vector changes. QRS loop projections of the \mathcal{C} , and its evolved \mathcal{G}_G and \mathcal{G}_H models, all in C334, between 1 and 31 ms, 31 and 64 ms, and 64 and 85 ms. Dashed arrows represent the dominant vectors of the loops.

Subsequently, three tests were performed on the \mathcal{G}_G model, incorporating transmural heterogeneities: C136, C334, and C532. The first and the last configurations were selected as extreme scenarios in the behavior of the T-wave, and the C334 was the one showing a behavior closer to the average, based on the tests carried out on the \mathcal{C} model, Fig. 3.16.

The C136 configuration reached a higher T-wave amplitude but decayed faster. On the contrary, C532 reached the lowest amplitude but extended its decay beyond the two additional compared models, Fig. 3.16. Regarding the QRS and T-wave angles, the C136 and C334 models maintained similar trends as those reported in the clinical data at certain angles (θ_{RT-XY} , ϕ_{R-ZY} , ϕ_{T-XY} , ϕ_{T-ZY} for adults, and θ_{RT-XY} , ϕ_{R-XZ} , ϕ_{R-XY} , ϕ_{T-XZ} for preadolescents, in Table 3.2). To compare the angular variation not only the angle difference values between control, \mathcal{C} , and deformation, \mathcal{G} , models, Δ , were compared, but the relative change, \mathcal{R} , calculated as the ratio between angle at deformation \mathcal{G} and at control \mathcal{C} , was computed, and displayed in Table 3.2. A value of $\mathcal{R} < 1$ represents an angular reduction in the \mathcal{G} model with respect to the \mathcal{C} model and a value of $\mathcal{R} > 1$ represents an increase. This index shows that the θ_{RT-XY} angle decreases in the \mathcal{G}_G models compared to the \mathcal{C} model but in a non-homogeneous way. The \mathcal{R} index shows a noticeable change on $\phi_{R-XZ} - \phi_{T-XZ}$, less marked in $\phi_{R-XY} - \phi_{T-XY}$, and shows a pronounced heterogeneous change on the $\phi_{R-ZY} - \phi_{T-ZY}$. Here it is possible to observe that the models C136 and C532 generate opposite extreme angular values, Fig. 3.16. For further comparative testing we also report the C334 model results as the intermediate behaviour.

The \mathcal{G} models kept the same Purkinje network and the apico-basal gradient and transmural heterogeneities than the \mathcal{C} model. The angle measurements are presented in Table 3.3. Second to fourth columns show the preadolescent results presented in [14], fifth to seventh columns show the adults results from [15], together with the \mathcal{R} and Δ indexes. Results on \mathcal{G}_G and \mathcal{G}_H models relative to the \mathcal{C} , were shown from eighth to twelfth columns. Angles that followed in simulation the same trend as in the clinical data are highlighted in bold and underlined.

Table 3.2: QRS and T-wave angles using different transmural heterogeneities on \mathcal{G}_G model. Δ and \mathcal{R} , angle difference and ratio, respectively, between deformed \mathcal{G}_G and control \mathcal{C} models. Bold, and underlined, font highlights the angles which tendency of change between \mathcal{G}_G and \mathcal{C} models follows similar trend to clinical results between IUGR and control for preadolescents [14], and adults [15], respectively.

Angle (degrees)	C136			C334			C532		
	\mathcal{C}	\mathcal{G}_G	$\Delta \mathcal{R}$	\mathcal{C}	\mathcal{G}_G	$\Delta \mathcal{R}$	\mathcal{C}	\mathcal{G}_G	$\Delta \mathcal{R}$
ϕ_{R-XZ}	43.1	40.4	-2.7 0.9	43.4	40.2	-3.1 0.9	43.2	38.9	-4.3 0.9
ϕ_{R-XY}	22.6	24.7	2.1 1.1	24.2	26.5	2.3 1.1	29.0	31.8	2.8 1.1
ϕ_{R-ZY}	38.4	<u>39.6</u>	1.2 1.0	36.9	<u>38.3</u>	1.4 1.0	33.0	<u>35.0</u>	2.0 1.1
ϕ_{T-XZ}	37.1	36.9	-0.2 1.0	37.5	37.1	-0.4 1.0	38.0	37.7	-0.3 1.0
ϕ_{T-XY}	30.5	<u>31.4</u>	0.9 1.0	28.7	<u>30.0</u>	1.2 1.0	22.4	<u>24.5</u>	2.1 1.1
ϕ_{T-ZY}	37.9	<u>37.4</u>	-0.6 1.0	39.1	<u>38.4</u>	-0.7 1.0	43.6	<u>42.3</u>	-1.2 1.0
θ_{RT-XY}	3.3	<u>0.8</u>	-2.5 0.2	4.9	<u>2.0</u>	-2.8 0.4	9.7	<u>5.3</u>	-4.4 0.5
$\phi_{R-XZ} - \phi_{T-XZ}$	6.0	<u>3.5</u>	-2.5 0.6	5.9	<u>3.1</u>	-2.8 0.5	5.2	<u>1.2</u>	-4.0 0.2
$\phi_{R-XY} - \phi_{T-XY}$	-7.9	<u>-6.8</u>	1.2 0.9	-4.5	<u>-3.5</u>	1.1 0.8	6.5	7.2	0.7 1.1
$\phi_{R-ZY} - \phi_{T-ZY}$	0.4	2.2	1.8 5.0	-2.2	<u>-0.2</u>	2.1 0.1	-10.6	<u>-7.3</u>	3.2 0.7

Table 3.3: Results are presented in three blocks: the leftmost block represents the clinical data for preadolescents, the central block represents the clinical data for adults, and the rightmost block represents the simulation results. The loop angle values are reported as mean \pm standard deviation or interquartile range. Simulation results display the angles obtained for deformation \mathcal{G}_G and control \mathcal{C} in configuration C334. The angles that exhibit a tendency of change between \mathcal{G}_G and \mathcal{C} models, similar to the tendency observed between IUGR and control subjects for preadolescents [14], are highlighted in bold. Likewise, for adults [15], the angles are underlined. Significant differences *p-value<0.05, **p-value<0.01.

Angle (degrees)	Clinical result preadolescents [14]			Clinical result adults [15]			Simulations on C334				
	Control n=60	IUGR n=33	$\Delta \mathcal{R}$	Control n=33	IUGR n=54	$\Delta \mathcal{R}$	\mathcal{C}	\mathcal{G}_G	$\Delta \mathcal{R}$	\mathcal{G}_H	$\Delta \mathcal{R}$
ϕ_{R-XZ}	37.6 (29.9 - 40.8)	34.2 (28.6 - 40.0)	-3.4 0.9	33.0 \pm 9.1	35.7 \pm 6.1	2.8 1.1	43.4	40.2	-3.1 0.9	40.7	-2.7 0.9
ϕ_{R-XY}	20.0 (10.1 - 28.6)	25.5 (19.8 - 33.6)*	5.5 1.3	29.5 \pm 13.0	22.1 \pm 11.8**	-7.4 0.7	24.2	26.5	2.3 1.1	24.5	0.3 1.0
ϕ_{R-ZY}	46.0 \pm 9.3	43.1 \pm 8.9	-2.9 0.9	40.7 \pm 12.1	44.2 \pm 9.8	3.5 1.1	36.9	<u>38.3</u>	1.4 1.0	<u>39.4</u>	2.5 1.1
ϕ_{T-XZ}	36.4 (32.1 - 38.8)	32.0 (28.6 - 38.6)*	-4.4 0.9	29.4 \pm 10.6	33.2 \pm 10.7*	3.8 1.1	37.5	37.1	-0.4 1.0	36.7	-0.8 1.0
ϕ_{T-XY}	29.4 (13.7 - 27.2)	21.5 (12.8 - 25.9)	-7.9 0.7	14.4 \pm 8.7	14.5 \pm 9.4	0.1 1.0	28.7	<u>30.0</u>	1.2 1.0	28.0	-0.7 1.0
ϕ_{T-ZY}	47.2 (38.8 - 52.9)	47.9 (41.1 - 56.6)	0.7 1.0	54.8 \pm 9.5	51.5 \pm 12.1	-3.3 0.9	39.1	<u>38.4</u>	-0.7 1.0	40.5	1.4 1.0
θ_{RT-XY}	6.6 (2.7 - 11.3)	6.5 (3.9 - 15.8)	-0.1 1.0	13.5 \pm 13.7	9.3 \pm 8.5**	-4.2 0.7	4.9	<u>2.0</u>	-2.8 0.4	3.2	-1.7 0.7
$\phi_{R-XZ} - \phi_{T-XZ}$	1.7 (-4.0 - 5.4)	0.9 (2.3 - 6.1)	-0.8 0.5	3.5 \pm 9.6	2.5 \pm 8.4	-0.9 0.7	5.9	3.1	-2.8 0.5	4.0	-1.9 0.7
$\phi_{R-XY} - \phi_{T-XY}$	-0.5 \pm 14.1	5.3 \pm 12.1*	5.8 -10.6	15.1 \pm 14.1	7.6 \pm 14.6**	-7.5 0.5	-4.5	<u>-3.5</u>	1.1 0.8	<u>-3.5</u>	1.0 0.8
$\phi_{R-ZY} - \phi_{T-ZY}$	-0.7 \pm 12.5	-4.9 \pm 12.7	-4.2 7.0	-14.1 \pm 14.0	-7.4 \pm 14.0**	6.8 0.5	-2.2	<u>-0.2</u>	2.1 0.1	<u>-1.1</u>	1.1 0.5

3.5.3 Impact of electrode position

The nodal displacement tests allowed us to identify the angular variation generated only by displacing the \mathcal{C} model a certain distance in different directions. Fig. 3.19 shows the values of the QRS loop angles, ϕ_{R-PL} , (horizontal axis) against the T-wave angles, ϕ_{T-PL} , (vertical axis), $PL \in \{XY, ZY, XZ\}$. Simulations results without displacement are shown in big squares: green for the \mathcal{C} model (center of the clouds in Fig. 3.19 subplots) and magenta and cyan for the \mathcal{G}_G and \mathcal{G}_H models, respectively.

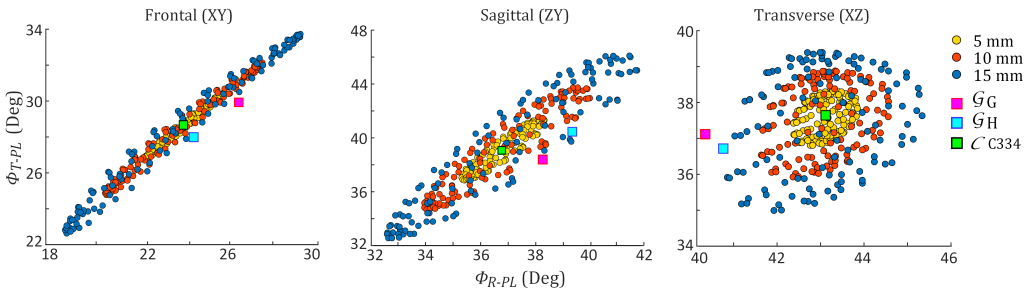


Figure 3.19: QRS, ϕ_{R-PL} , vs T-wave, ϕ_{T-PL} , angles, $PL \in \{XY, ZY, XZ\}$, from the VCG, considering a 5 (yellow), 10 (orange), and 15 (blue) mm displacement of the heart inside the torso. Each color group shows one hundred and twenty tests. The green square shows the control \mathcal{C} results, and the magenta and cyan squares correspond to the angular results for the \mathcal{G}_G and \mathcal{G}_H models without displacement, respectively.

Table 3.4 presents the impact of heart displacement on the angular loops. The analysis shows that the maximum change in angle occurs in ϕ_{T-ZY} , followed by ϕ_{T-XY} . However, the relative angles (last three rows) exhibit lower changes, likely due to their nature as relative angles, where the influence of displacement is reduced. As observed earlier (Fig. 3.17), the transverse plane XZ showed lower angle variations. Based on Fig. 3.18, we observe that the deformations primarily occur along the X and Y axes, while the deformation along the Z axis is minimal. In addition, the loop in the XZ plane mainly spans along the Z axis, resulting in minimal changes to its axis. As a result, this contributes to the lower variability of angles observed in the XZ plane, even in the displacement tests.

The nodal displacement in all the \mathcal{G}_{A-H} models did not exceed 3mm in all axes, for this reason, the angle measurements were compared against the 5mm displacement in the Fig. 3.20. In this figure, the magenta region represents the angular variation obtained when the \mathcal{C} model is displaced 5mm in any direction and is compared with the loop and dominant vector of the deformed \mathcal{G}_G model.

Table 3.4: Angle value for model \mathcal{C} with no displacement, and \pm standard deviation (\pm SD) when $\|\mathbf{d}_k\| \neq \mathbf{0}$. Bold font highlights the larger SD. Note that the angle value for $\|\mathbf{d}_k\| = \mathbf{0}$ is the same as the mean angle for $\|\mathbf{d}_k\| \neq \mathbf{0}$.

Control model \mathcal{C} , with C334				
$\ \mathbf{d}_k\ $ (mm)	0	5	10	15
Degrees ($^\circ$)	Angle	SD	SD	SD
ϕ_{R-XZ}	43.4	± 0.5	± 0.9	± 1.4
ϕ_{R-XY}	24.2	± 1.2	± 2.4	± 3.6
ϕ_{R-ZY}	36.9	± 1.0	± 2.0	± 3.0
ϕ_{T-XZ}	37.5	± 0.5	± 1.0	± 1.4
ϕ_{T-XY}	28.7	± 1.2	± 2.5	± 3.8
ϕ_{T-ZY}	39.1	$\pm \mathbf{1.5}$	$\pm \mathbf{3.0}$	$\pm \mathbf{4.6}$
θ_{RT-XY}	4.9	± 0.7	± 1.5	± 2.2
$\phi_{R-XZ} - \phi_{T-XZ}$	5.9	± 0.6	± 1.2	± 1.8
$\phi_{R-XY} - \phi_{T-XY}$	-4.5	± 0.2	± 0.3	± 0.5
$\phi_{R-ZY} - \phi_{T-ZY}$	-2.3	± 0.7	± 1.4	± 2.0

3.6 Discussion

Significant cardiac morphological changes as a consequence of IUGR remain from the fetal stage to adolescence and adulthood [113], [96], [13], [15] and have been associated with cardiovascular disease [43], [46], [114], [16]. The impact of morphological changes on cardiac electrical activity might contribute to a better understanding of IURG-related cardiac remodeling. In this work, we evaluated whether the morphological changes described in IUGR subjects [13] result in the changes in QRS and T-wave loop angles observed in patients [14, 15], using computational models based on heart and torso realistic anatomies.

3.6.1 Analysis of angular variability in simulation

The incorporation of transmural heterogeneities to the control \mathcal{C} model aims to represent *in silico* the observed inter-patient variability in tissue proportions and assess its impact on the analyzed angular parameters. In Fig. 3.16, it is possible to see the impact that transmural changes have on the amplitude of the T-wave and its duration, causing changes in all the angular parameters [115],

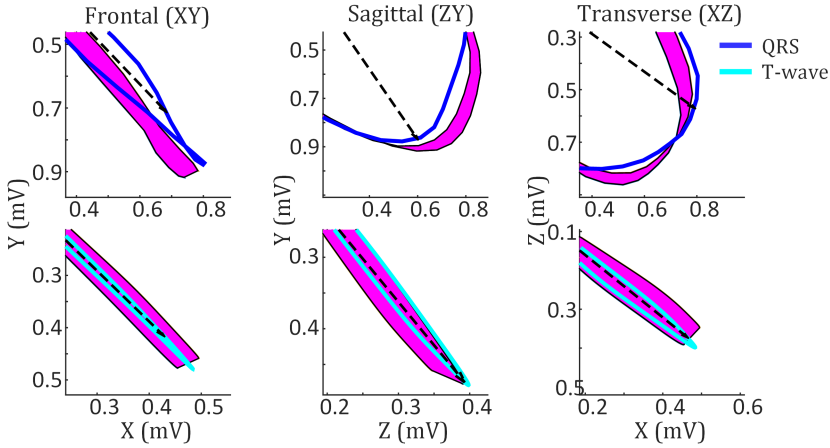


Figure 3.20: QRS and T-wave loops in the three VCG planes. The magenta region corresponds to the angle variation when displacement $\|\mathbf{d}_k\|=5$ mm in any direction. QRS and T-wave loops correspond to the \mathcal{G}_G model simulation. Dotted lines represent the dominant vectors.

but in different proportions. In Fig. 3.17, we can observe a higher dispersion of angles in the frontal plane XY. On the other hand, in the transverse plane XZ, the lowest variability in angles is evident for ϕ_{R-XZ} and ϕ_{T-XZ} .

IUGR can occur due to a combination of unfavourable maternal, placental, fetal, and genetic factors. Cardiac remodeling as a consequence of IUGR has been evidenced by a change in the ventricular SpI, reducing the \mathcal{L} length and increasing ϕ [13]. We deformed the \mathcal{C} model by applying loads on different regions of the ventricular model (Fig. 3.11). The simulated globular models underwent changes in their SpI that aligned with the magnitude observed in clinical data. These changes were achieved through the implementation of eight distinct deformation protocols, intended to replicate the effects of IUGR. The different methods applied to obtain the deformed models \mathcal{G}_{A-H} influence the angular parameters of the QRS and the T-wave. Fig. 3.17 shows these calculated angles, in addition to the reference angular value of the control \mathcal{C} model at configuration C334. QRS angles present greater variability than T-wave angles, because the reduction in the \mathcal{L} length and the widening of the ϕ directly affect QRS, reducing the time in which the apex and the external walls of the LV were activated.

In the simulation, a wide range of transmural differences were considered being C136 and C532 configurations the ones displaying extreme angular values. However, the angular variability resulting from transmural cell type is

smaller than the one resulting from the deformed \mathcal{G}_{A-H} models in Fig. 3.17, particularly when only non extreme tissues dispersion is considered, consistent with the significant variations found in patients. Fig. 3.17 additionally shows the angular result when introducing extreme transmural heterogeneities (C136 and C532) on the deformed models \mathcal{G}_G and \mathcal{G}_H . As expected, this variation caused extreme angular values in the T-wave and minor changes in the QRS, following the same pattern of change evidenced in the results with the \mathcal{C} model.

The results obtained in this article were compared with clinical results of preadolescents [14] and adult subjects [15] with IUGR. Only some of the measured parameters present a statistically significant difference between IUGR and control subjects; however, they were not the same in preadolescents and adults, with the exception of: ϕ_{R-XY} , ϕ_{T-XZ} , and $\phi_{R-XY} - \phi_{T-XY}$. The θ_{RT-XY} angle, measured in both preadolescents and adults, shows a decreasing trend in the IUGR groups, although the change reaches statistical significance only in adults.

Considering the angles that present significant variation, both control groups (preadolescent and adult) in clinical studies, exhibit different central tendency values, likely due to the anatomical and physiological differences between age groups. Similarly, when comparing the IUGR groups (preadolescent and adult), the opposing angular variations may be associated not only with the consequences of IUGR but also with changes in cardiac orientation and differences in ventricular mass, for instance. Additionally, large intersubject angular variability contributes to the apparent reversal of mean trends from adolescence to adulthood. Despite this, the changes in depolarization and repolarization angles calculated *in silico* simulations were mostly concordant with the clinical results when evaluating the \mathcal{R} index, Table 3.3.

The significant difference observed between the two clinical studies is notable, although the opposing trends warrant further investigation to identify which additional parameters are influencing these changes. It may also be necessary to conduct a more extensive study involving preadolescents and adults to obtain more detailed electrophysiological insights.

From Table 3.3, in the simulation section, it can be observed that the slight longitudinal displacement of the heart (~ 3 mm) in the globular models, resulting from the shortening of \mathcal{L} , can affect the calculated angles and their interpretation. Observing the trend of changes, the \mathcal{G}_G model shows more angular parameters aligned with those observed in the clinical data from the adult study, whereas the \mathcal{G}_H model presents a pattern of angular changes more consistent with the study in preadolescents.

These results support that the morphological remodeling of the heart is, at least partially, responsible for the observed electrophysiological changes modifying most of the depolarization and repolarization angles. However, angle variations were also observed to be sensitive to the relative position of the heart with respect to the torso and electrodes, although the impact of these variations were lower than those observed by the morphological remodeling, for low displacements, as expected from electrode misspositioning, etc.

The θ_{RT-XY} values, both in the \mathcal{C} and \mathcal{G} models, were within the ranges of healthy people [116]. A wider angle (greater than 100 degrees) is usually associated with changes in the T-wave axis rather than QRS related and carries a considerably increased cardiac risk [117]. Reasons for θ_{RT} angle changes are associated to changes in ventricular repolarization itself, or secondary to conduction abnormalities [118, 119]. A wide spatial θ_{RT} angle has been demonstrated to be a predictor of sudden cardiac death in the general population (low risk) and in groups considered to be at higher risk (clinical population) and a strong predictor of all-cause mortality in post-menopausal women [117, 119, 120]. In our study, the reduction in θ_{RT-XY} can be attributed to changes in both the QRS and the T-wave dominant vectors, being the QRS angle the one showing the largest change (Table 3.3). Both QRS and T-wave angles changed from control to deformed simulations without considering ventricular conduction abnormalities in the deformed model. A recent genome-wide association study showed that ventricular conduction abnormalities are the most likely cause of QRS-T angle widening, being able to counteract the reduction in θ_{RT-XY} [118]. As far as we know, there have been no studies indicating that conduction abnormalities occur as a result of IUGR. Therefore, in this analysis, we have kept the same conduction system in the control and deformed models in order to specifically assess the effect of geometrical changes on the VCG loops.

This reduction in θ_{RT-XY} between control and IUGR patients is tiny in the clinical results reported in [14] with $\mathcal{R} = 1.0$, and larger in [15] with $\mathcal{R} = 0.7$, and it is reproduced with a similar trend in the simulation results for the \mathcal{G}_G and \mathcal{G}_H models, with values of $\mathcal{R}=0.4$ and 0.6 respectively (Table 3.3).

Regarding the transverse plane XZ, the clinical results show a significant difference only in ϕ_{T-XZ} . The simulation results show a similar trend than in adolescents and reverted than in adults data ($\mathcal{R} = 0.9$ for preadolescents, $\mathcal{R} = 1.1$ for adults, and $\mathcal{R} = 1.0$ for the \mathcal{G}_G and \mathcal{G}_H models). In the same plane, ϕ_{R-XZ} shows an index $\mathcal{R} = 0.9$ for the \mathcal{G}_G and \mathcal{G}_H models, similar to preadolescents and contrary to $\mathcal{R} = 1.1$ in adults.

The angular variation with respect to the sagittal plane ZY does not show

a significant difference in the clinical results; however, the \mathcal{R} index shows a trend similar to the simulations results. For ϕ_{R-ZY} , $\mathcal{R} = 0.9$ (preadolescents), $\mathcal{R} = 1.1$ (adults) and 1.0 for \mathcal{G}_G and 1.1 for \mathcal{G}_H model. For ϕ_{T-ZY} , $\mathcal{R} = 1.0$ (preadolescents), $\mathcal{R} = 0.9$ (adults) and 1.0 for \mathcal{G}_G and \mathcal{G}_H models.

The changes in planarity and roundness of the QRS and the T-wave loops in \mathcal{G}_G and \mathcal{G}_H models with respect to \mathcal{C} model were also computed as in [14], and did not evidence significant changes, similar to what was reported for clinical results in preadolescents [14]. Although the angular variations in QRS and the T-wave loops introduced by deformation were small, these variations were still greater than those generated by the incorporation of transmural heterogeneities or due to displacement of the heart alone. The angular variation is more accentuated (\mathcal{R} index more different from 1) when comparing the relative angular values between the QRS and the T-wave, $\phi_{R-PL} - \phi_{T-PL}$, last three rows in Table 3.3, and its trend is congruent to the clinical results in adults. Note that in preadolescents the angles at control were very small making the index \mathcal{R} less reliable.

3.6.2 Angular changes with electrode position

We can see in Fig. 3.20 that, although the displacement of the \mathcal{G}_G model does not exceed 3 mm, the dominant vector direction of the QRS loop is clearly different, which supports the hypothesis that the angular variation is not only a result of the nodal displacement of the heart but also of its deformation.

In the 5 mm displacement test (Table 3.4), we found a linear angle variation with a maximum value of 1.5 degrees on T-wave loop with respect to the sagittal plane ZY. Considering the deformed models, the change in the θ_{RT-XY} showed a variation of less than 3 degrees. This slight variation aligns with the clinical observations of IUGR preadolescents used for validation in this study, who showed an average change of 0.1 degrees [14]. Furthermore, IUGR adults displayed a mean change of 4.2 degrees [15]. These values for changes in the θ_{RT-XY} angle are small compared to those produced by other clinical pathologies such as conduction abnormalities, suggesting that the IUGR preadolescents included in the study have not developed any conduction abnormality. Previous studies have shown that displacement of precordial leads by 2 cm can result in changes in R wave progression in the precordial zone [121].

In the study conducted by Nguyen et al. [122], an *in silico* study was performed by reconstructing cardiac structures using magnetic resonance imaging from five subjects with intraventricular conduction defects. The heart was simulated considering displacements in four directions of up to 6 cm and a rotation

of $\pm 30^\circ$ around the anteroposterior axis. The results revealed changes in the QRS-T angle ranging from -6% to 3% , and a greater variation in the amplitude of the QRS complex, ranging from -36% to 59% . In our study, θ_{RT-XY} showed a variation of -59.2% for the \mathcal{G}_G model and -34.7% for the \mathcal{G}_H model. From a clinical perspective [123], in a total of 194 patients, the diagnosis did not change in 87.5% of cases when the electrodes were shifted from the fifth to the fourth intercostal space. The QRS-T angle showed a variation ranging from -13.2% to 18.1% .

Cardiac remodeling of the fetus involves various mechanisms inducing the morphological change, as an adaptation to pressure and volume excess and resulting in a reduction of the SpI. In addition to this anatomical remodeling, electrophysiological changes with dominant QRS and T-wave angular variations have been reported [14, 15]. *In silico* simulations have allowed us to observe that the anatomical variation of the SpI of the heart is associated with an angular modification of the depolarization and repolarization vectors on most of the angles, with a similar trend to that reported in the literature. The angles also result sensitive to the relative position of the ventricles with respect to the torso and to the electrodes placed on it, which introduces an additional factor to the sphericity in the interpretation of the results.

The globularly deformed \mathcal{G} model of the heart was based on the results presented by [13] where the change in the sphericity of preadolescents as a consequence of IUGR is evidenced with a subtle variation. Although the used SpI was obtained from a cohort of preadolescents, we still compare with adults based on the study in [48], where it is evidenced that anatomical and functional changes can be maintained from childhood to adulthood, even questioned by other studies [124]. Variations in the rotation of the heart within the torso were not considered in our deformed \mathcal{G} models, a factor that can alter the potentials calculated on the leads. This fact is strengthened by observing that the depolarization and repolarization angles and their tendency change significantly when the VCG is calculated using the coefficients for Kors regression transformation. We have included the results of VCG using the inverse Dower method to be able to contrast the results with those presented in the literature [14, 15].

The control \mathcal{C} and deformed \mathcal{G} models have been simulated keeping the same fiber orientation and the same Purkinje network adapted to the globular models in order to specifically assess the impact of the morphological changes on the depolarization and repolarization loop angles. The changes observed in the QRS angle are only due to the geometrical deformation as the conduction system remained unchanged in the control and the deformed models. Factors such as conduction abnormalities have not been taken into consideration and

are deemed beyond the scope of this study, requiring proper remodeling quantification under IUGR to include the effects in a future study. Although it is known that intrauterine growth in an unfavorable environment leads to a different structuring of the fibers, which would change the cellular conductivity pattern [59], it has also been observed in adults that changes in pressure on an infarcted region do not lead to significant changes in fiber orientation at the edge of the infarct zone [124], which makes uncertain to what extent a change in pressure, characteristic of cardiac remodeling, leads to fiber orientation remodeling.

Future research should focus on extending the work presented here, using models of rounded hearts developed from real images and considering the position and rotation of the heart within the torso. Additionally, the impact of cardiac remodeling on the direction of the myocardial fibers and on the Purkinje network requires further studies.

3.7 Conclusions

The findings of this computational study indicate that the SpI of the heart, which represents anatomical variations, partially accounts for the changes observed in the dominant vectors of depolarization and repolarization reported in clinical studies [14, 15]. Changes in the dominant depolarization and repolarization angles can result from both ventricular spherical alterations and the relative displacement of the heart in relation to the torso and attached electrodes. However, it has been observed that the angular variations caused solely by heart displacements are smaller than those generated by deformation, particularly when the displacement remains within a few mm.

The reduction in θ_{RT-XY} and $\theta_{R-XZ} - \theta_{T-XZ}$ aligns with the reported clinical trends in adults and preadolescents, highlighting them as suitable biomarkers for quantifying sphericity reduction. Furthermore, these relative measures focusing on the depolarization-repolarization relationship were less sensitive to changes in heart-to-electrode positioning, making them more robust and suitable for clinical use.

The variations observed in the absolute angles (i.e., the angles between depolarization and repolarization loops) in the computational simulations, as shown in the last three rows of Table 3.3, do not align with the clinical data obtained from adults and/or preadolescents. This phenomenon can be attributed to the fact that the remodeling observed in preadolescents may not persist in adults [14, 15], thus affecting the comparison. Whether this is a result of

methodological limitations or attenuation of the remodeling in adulthood will require future studies.

CHAPTER 4

QRS WIDTH AND T-PEAK TO T-END INTERVAL IN PREADOLESCENTS WITH SEVERE IUGR AT BIRTH WHEN COMPARED TO CONTROLS

4.1 Dataset and signal processing

- 4.1.1 Dataset
- 4.1.2 ECG waves delineation
- 4.1.3 ECG interval biomarkers from delineation marks
- 4.1.4 Optimal spatial transform leads for QRS or T waves measurement

- 4.2.1 QRS width and T peak-to-end intervals in IUGR and control patients

- 4.2.2 Intervals result on PCA_{QRS} and PCA_T transform leads

4.3 Discussion

4.4 Conclusions

4.2 Results

In Chapter 3, the *in silico* impact of geometric changes associated with IUGR on the angular variation of depolarization and repolarization loops was evaluated. IUGR shows morphological changes in the ventricles beyond the fetal stage, evidencing cardiac structural and functional remodeling [13] that manifest as variations in the depolarization and repolarization phases of the VCG in preadolescents [14] (see Sections 1.5.1 and 1.5.2, respectively). Some of these electrical changes have also been measured in adults with IUGR [15,63]. Results from previous studies have shown significant changes in the duration intervals of the depolarization and repolarization phases (see Section 1.6) in

subjects who experienced IUGR. Some of the studies and their findings have been summarized in Table 1.1 of the same section.

From the standard 12-lead ECG, the QT and T_{pe} intervals have been identified as predictors of ventricular arrhythmias in several cardiac conditions [41]. Besides, the T_{pe}/QT ratio, which quantifies the dispersion of repolarization relative to ventricular action potential duration, is considered an index of arrhythmogenesis [42]. T-wave morphology accounts for the spatial dispersion of APD found in the transmural ventricular wall, apex-to-base and right-to-left directions [57]. As IUGR-related cardiac remodeling involves basal diameter ϕ widening and increase of the ventricular wall thickness (W), we hypothesize these anatomical changes may affect T-wave morphology and therefore T_{pe} . Additionally, it is not known how these differences in anatomy may affect the time of ventricular activation reflected in the ECG as QRS width.

In this chapter, we employed the methodology and the 12-lead ECG dataset introduced in Chapter 2 to measure intervals in a cohort of IUGR and control subjects. Automatic annotation was performed on the leads, and QRS_d , T_{pe} , and QT intervals were compared between the control and IUGR groups. Additionally, PCA was applied to isolate and emphasize the QRS complex (PCA_{QRS}) and the T-wave (PCA_T). QRS_d was measured on the PCA_{QRS} derived signal, while T_{pe} and QT intervals were measured on PCA_T . Finally, these interval measurements were replicated on the globular model G_G to assess whether the clinical data findings could also be observed *in silico*.

4.1 Dataset and signal processing

4.1.1 Dataset

The dataset used for the chapter was detailed in Section 2.4.5 and consisted of 12-lead ECG recordings (13 seconds at a sampling frequency of 1000 Hz) from a population of 93 preadolescents. From those, 33 subjects had severe IUGR with medically induced preterm delivery and 60 subjects were normally grown controls born at term. IUGR and control subjects were selected from the study conducted at a tertiary centre (Hospital Clinic of Barcelona) [96].

4.1.2 ECG waves delineation

The ECGs were delineated, identifying QRS onset and end and the T-peak and T-end fiducial points using a wavelet-based ECG delineator [89]. We made use

of the BioSigBrowser (BSB) software [125] using the delineator in a multi-lead strategy [89]. This wavelet-based delineator identifies the onset, offset, and primary peaks of the P wave, QRS complex, and T-wave. When executing the delineation algorithm on the ECG data of a subject, a *.mat file is generated for each of the eight independent ECG leads input into the application, containing the detection times of each characteristic point of the signal (see Fig. 4.1).

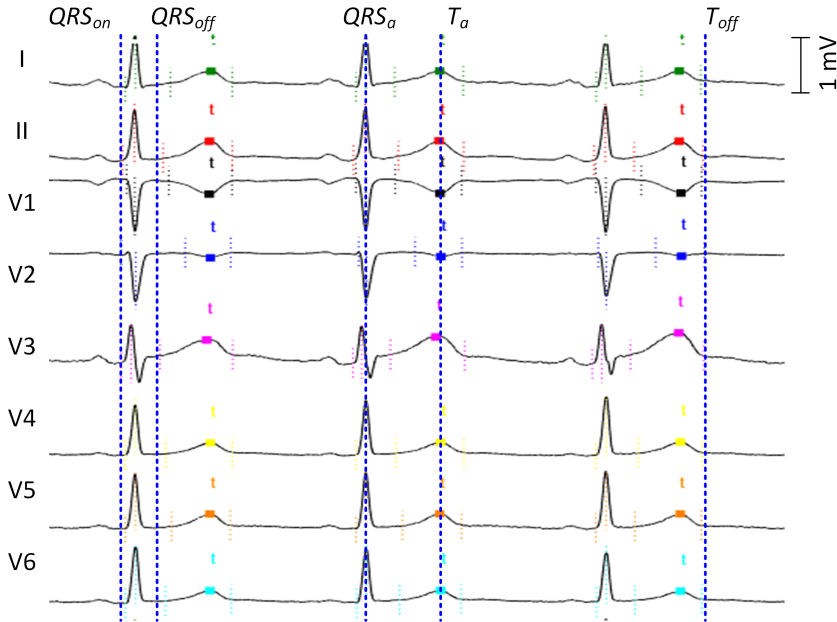


Figure 4.1: Identification and marking of the P wave, QRS complex, and T-wave across each of the 8 ECG leads. The blue dotted lines are aligned with the markers of lead V2 to illustrate that the markers for each lead are different when a selection rule is not applied.

A standard ECG recording simultaneously captures signals from all available leads. Thus, it is expected that, for instance, the P wave onset will be similar across all leads, except for some small projection termination differences at different axis (leads). Considering this fact, it can be ensured that the detection of a wave onset mark can be considered as valid as long as the detection is present in at least a number k of leads. If the detection is not found in these number of leads, it may be considered an incorrect detection in the signal. To apply this detection rule, the BSB application is configured to evaluate the single-lead generated list of detections. The algorithm organizes the detected annotation times into a matrix, with values expressed in sample units. The matrix consists of cells, one for each ECG recording. Each cell is

composed of a number of rows equal to the number of beats per subject, and the columns (15 in total) correspond to the following detected points:

- P onset, P peak, P' peak (if it exists), and P end.
- Main QRS peak, QRS onset, Q peak, R peak, S peak, R' peak (if it exists), and QRS end.
- T onset, T peak, T' peak (if it exists), and T end.

Using this annotation matrix, beat selection is performed by applying the single-lead delineation combined with a multilead rule technique to identify global, lead-independent fiducial points for each beat, following the rules described in [126]. To detect a representative mark across all leads, a selection rule based on the median of the peak positions from all leads is applied. For the identification of onset/end limits of the signals, the annotations are first ordered. Then, the selected single-lead annotation is the earliest among onsets and the latest among offsets that satisfies the condition of having at least k neighbors within a window of σ ms. In the algorithm, this selection process requires the input of certain configuration parameters, including the signal's sampling frequency, the k neighbors value, and a QRS complex period of analysis, based on the sampling frequency. Finally, an annotation matrix adjusted to these rules is generated, as shown in Fig. 4.2

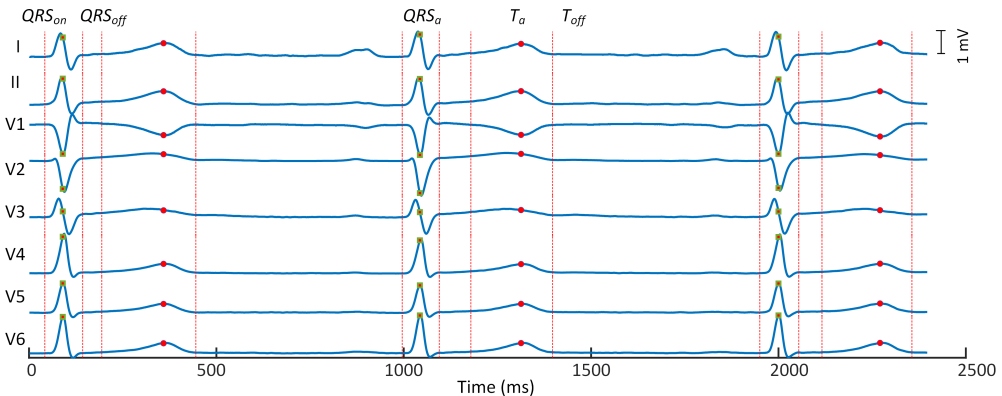


Figure 4.2: 12-lead ECG with annotations following a multilead rule. The onset, peak, and end of the QRS complex and T-wave are shown. The red dashed lines indicate the markers, now aligned across all leads.

4.1.3 ECG interval biomarkers from delineation marks

Using the dataset of 93 subjects, we proceeded to compute interval biomarkers in the 8 leads of each subject. A visual inspection was performed for each lead to detect errors in the delineation process. For all patients, the first beat was discarded, and an initial measure of the distance between R peaks (RR interval) was established, calculated as: $RR = (RR_i - RR_{i-1})/1000$, corresponding to the i -th heartbeat, when expressed in seconds. Subsequently, the duration of the QRS complex QRS_d was computed as: $QRS_d = (QRS_{end} - QRS_{onset})/1000$. Knowing this interval for each beat, the patient median value was calculated and considered representative for each patient. The position of the median value was identified to perform an additional visual analysis, ensuring that the median value was representative for each patient and that no abnormal value was selected as the median. Fig. 4.3 shows lead I from the ECG of IUGR subject #33, highlighting the identified median value of QRS_d . From this process, we obtained two vectors: one for the control group and one for the IUGR group, with 60 and 33 QRS_d values, respectively, one for each patient. Subsequently, the median and interquartile ranges of these two vectors were determined.

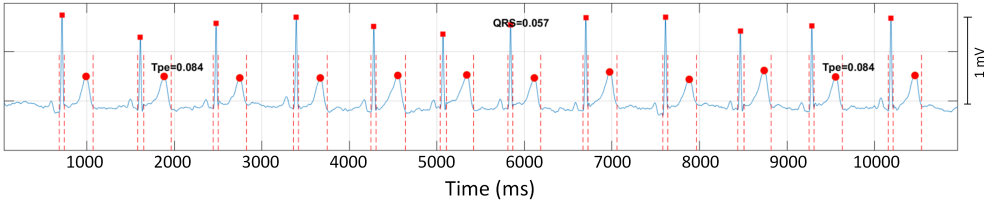


Figure 4.3: Detection of the median in IUGR subject #33 on lead I. The QRS median is a single value, while the $T_{pe,c}$ median is the average of the two observed values, as containing an even number of beats with $T_{pe,c}$ measurement.

The T_{pe} and QT values were determined for each beat and corrected using Fridericia's formula [127, 128],

$$T_{pe,c} = \frac{T_{pe}}{\sqrt[3]{RR}}, \quad (4.1)$$

$$QT_c = \frac{QT}{\sqrt[3]{RR}}, \quad (4.2)$$

respectively, ensuring that the corresponding RR value for each T-wave (rather than the median) is used for the correction. Using the corrected T_{pe} ($T_{pe,c}$) and the corrected QT (QT_c) for each patient, the median is calculated, and the

beat position is identified for further review. This median value is considered representative of each patient. Finally, we obtained two vectors: one for the control group and one for the IUGR group, with 60 and 33 median values, respectively, for both $T_{pe,c}$ and QT_c . For each patient, the ratio $T_{pe,c}/QT_c$ is also computed, resulting in a third vector for both the control and IUGR groups. From the three resulting vectors, we proceeded to calculate the median and interquartile range as representative values for each patient group. Statistical comparison was performed between the control and IUGR groups using the Student's t-test, and for each group, the median and interquartile range were recalculated. The results are displayed in the Table 4.1

4.1.4 Optimal spatial transform leads for QRS or T waves measurement

Clinical Electrocardiographic data

The measurement of intervals (QRS_d , T_{pe} , and QT) in the control and IUGR groups showed variability among the leads due to the different projection of the electrical activity at each lead axis. Each lead contains specific information that allows for defining the duration of depolarization and repolarization intervals differently. To perform a global analysis, independent of the lead projection, a linear combination of the 8 leads in the ECG database, generating a new spatial lead transformation was used to generate a new lead where the information from the independent 8-leads was maximally condensed at the transformed lead, and where more accurate delineations can be obtained. The transformation is made based on the PCA technique which maximized the signal energy at the transform lead, and consequently the robustness of measured performed on that signal. The description of the application of this technique to ECG signals was detailed in Section 2.4.4.

To extract depolarization-based biomarkers, the transform coefficients were learned by focusing on the QRS region of multiple training beats. This process generates PCA_{QRS} to improve the robustness of features measured within the QRS complex. Alternatively, when features of the T-wave were of interest, the transform PCA_T was learned using the T-wave segment. The transformed leads from PCA_{QRS} and PCA_T were then analyzed to identify key fiducial points in the ECG, including the R peak, the onset and end points of the QRS complex, the T-wave, and its peak and end (Fig. 4.4). On the new spatially transformed leads, the R amplitude (QRS_a) and the amplitude of T-wave (T_a) were measured in the PCA_{QRS} and PCA_T leads, respectively.

The T_{pe} and QT values were determined for each beat and corrected using

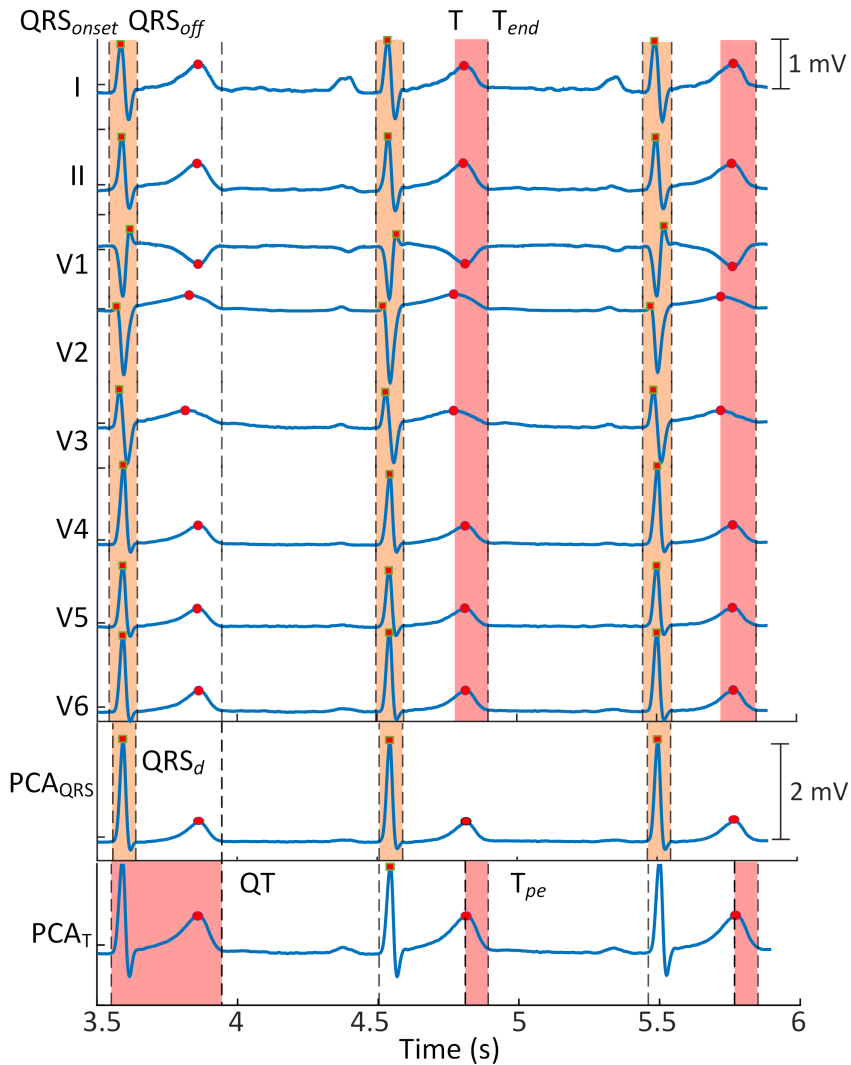


Figure 4.4: The independent 8 ECG leads from a subject in the control group with marks on QRS onset and end, R-wave peak, T-wave onset, peak, and end with red long lines. Similarly, PCA_T and PCA_{QRS} first leads include annotations marked as red lines over the leads together with definitions of the intervals of interest (T_{pe} , QT, and QRS) shaded in purple.

Fridericia's formula according to equations (4.1) and (4.2), respectively. Subsequently, the medians of $T_{pe,c}$ and QT_c series were taken as representatives for each patient. The $T_{pe,c}/QT_c$ ratio was also calculated. Statistical comparison was performed between the control and IU GR groups using the Student's t-

test, and for each group, the median and interquartile range were recalculated. The results are displayed in the Table 4.2.

On each patient's PCA_{QRS} lead, the onset and end of the QRS complex were identified, and a parallel comparison was made between the duration of this interval between the control and IUGR groups.

Manual delineation was performed on the PCA_{QRS} lead of two subjects at the QRS onset, as automatically generated marks were erroneously located on the peak of the Q-wave and not at its beginning, due to a low Q voltage protection rule of the delineator.

Simulated data from computational models

Additionally, computational simulations of cardiac electrophysiology were conducted using the biventricular electrophysiological model presented in Section 2.3, based on a realistic heart and torso [112]. The \mathcal{C} model and the globular \mathcal{G}_H model were used as computational models for control and IUGR respectively. Both models included a tissue division of 30%, 30%, and 40% for endo, mid, and epi tissue respectively.

FEM was employed on the control and IUGR models to determine the electrical propagation in cardiac tissue using a monodomain model [64]. A sequence of three beats were simulated to reach steady state conditions in the ventricular electrical activity with a cycle length of 1000 ms, using a stimulus amplitude of 200 mA and a stimulus duration of 0.5 ms. To compute the 12-lead ECG simulations, a torso volume was used to calculate the extracellular potential at virtual electrode positions. Using the simulated ECG, PCA_T and PCA_{QRS} leads were also computed and delineated for fiducial points and related interval estimations in simulation.

4.2 Results

4.2.1 QRS width and T peak-to-end intervals in IUGR and control patients

The results are described based on the comparison between the QRS_d , $T_{pe,c}$, and QT_c intervals of the IUGR cohort ($n=33$) and the control group ($n=60$). Initially, the intervals were compared across each of the eight leads between the two study groups. In general, the measurements of the ECG intervals show variability across all eight leads, as shown in Table 4.1. The intervals for

the control and IUGR groups were evaluated using the t-student test, and the p -value is included in the Table.

Statistical analysis of the ECG intervals revealed significant differences between control and IUGR groups in specific leads. In Lead II, the QRS_d was significantly shorter in the IUGR group compared to controls ($p=0.015$), with a difference between medians of 4 ms. In Lead V4, multiple parameters showed significant changes: the $T_{pe,c}$ interval was prolonged in the IUGR group (5 ms, $p=0.005$), the $T_{pe,c}/QT_c$ ratio was higher (0.006, $p=0.016$), and the QRS_a was reduced (0.1 mV, $p=0.046$), indicating both increased repolarization dispersion and diminished depolarization voltage. Additionally, in Lead I, although the median QRS_a appeared similar between groups, a highly significant difference ($p=0.004$) was observed, with greater variability in the IUGR group.

Complementary to these findings, other leads such as V2 and V5 exhibited noticeable trends toward lower QRS_a and prolonged depolarization in IUGR, although without reaching statistical significance. These results collectively highlight distinct alterations in both depolarization and repolarization processes in subjects with a history of IUGR.

Lead	ECG Intervals, (ms)					Waves amplitude (mV)	
		QRS _d	T _{pe,c}	QT _c	T _{pe,c} /QT _c	QRS _a	T _a
I	Control	85 (78 - 91)	78 (74 - 82)	394 (379 - 411)	0.197 (0.189 - 0.209)	0.5 (0.3 - 0.6)	0.2 (0.2 - 0.2)
	IUGR	82 (73 - 88)	78 (75 - 81)	397 (385 - 404)	0.199 (0.189 - 0.206)	0.5 (0.4 - 0.8)	0.2 (0.1 - 0.3)
	p-value	0.314	0.847	0.884	0.848	0.004	0.787
II	Control	83 (74 - 92)	77 (75 - 82)	395 (379 - 406)	0.197 (0.188 - 0.211)	1.1 (0.9 - 1.3)	0.3 (0.3 - 0.4)
	IUGR	79 (63 - 84)	80 (73 - 84)	390 (383 - 400)	0.201 (0.190 - 0.217)	1.1 (0.9 - 1.4)	0.3 (0.2 - 0.4)
	p-value	0.015	0.139	0.758	0.146	0.870	0.140
V1	Control	90 (82 - 96)	73 (69 - 78)	403 (387 - 418)	0.181 (0.176 - 0.192)	0.3 (0.2 - 0.3)	-0.2 (-0.3 - -0.2)
	IUGR	91 (84 - 99)	75 (70 - 77)	399 (387 - 411)	0.185 (0.178 - 0.195)	0.3 (0.2 - 0.3)	-0.3 (-0.3 - -0.2)
	p-value	0.944	0.309	0.792	0.262	0.962	0.680
V2	Control	91 (85 - 94)	84 (60 - 112)	392 (376 - 412)	0.226 (0.155 - 0.278)	0.6 (0.4 - 0.8)	0.1 (-0.0 - 0.2)
	IUGR	95 (87 - 101)	76 (62 - 114)	397 (379 - 414)	0.181 (0.161 - 0.260)	0.5 (0.3 - 0.7)	0.1 (-0.1 - 0.2)
	p-value	0.087	0.582	0.331	0.438	0.072	0.133
V3	Control	91 (88 - 95)	86 (73 - 107)	403 (383 - 415)	0.215 (0.185 - 0.263)	0.8 (0.6 - 1.2)	0.2 (0.1 - 0.3)
	IUGR	91 (86 - 95)	79 (62 - 116)	403 (395 - 414)	0.206 (0.158 - 0.282)	0.8 (0.6 - 1.0)	0.1 (0.0 - 0.3)
	p-value	0.845	0.563	0.555	0.439	0.109	0.345
V4	Control	81 (75 - 88)	78 (75 - 84)	393 (376 - 404)	0.201 (0.193 - 0.216)	1.4 (1.1 - 1.7)	0.3 (0.2 - 0.4)
	IUGR	83 (69 - 88)	83 (76 - 92)	396 (383 - 409)	0.207 (0.195 - 0.235)	1.3 (1.0 - 1.5)	0.3 (0.1 - 0.4)
	p-value	0.958	0.005	0.350	0.016	0.046	0.097
V5	Control	80 (72 - 88)	76 (73 - 80)	391 (378 - 400)	0.196 (0.186 - 0.206)	1.3 (1.1 - 1.5)	0.3 (0.3 - 0.4)
	IUGR	79 (65 - 84)	78 (74 - 82)	387 (376 - 399)	0.200 (0.191 - 0.215)	1.4 (1.0 - 1.6)	0.3 (0.2 - 0.4)
	p-value	0.177	0.087	0.571	0.080	0.554	0.432
V6	Control	78 (73 - 85)	75 (72 - 79)	392 (379 - 408)	0.191 (0.184 - 0.199)	1.1 (0.9 - 1.4)	0.3 (0.2 - 0.4)
	IUGR	78 (63 - 85)	77 (73 - 78)	390 (379 - 400)	0.197 (0.189 - 0.202)	1.2 (1.0 - 1.4)	0.3 (0.2 - 0.4)
	p-value	0.457	0.326	0.581	0.261	0.626	0.905

Table 4.1: Measurements of QRS_d, T_{pe,c}, and QT_c intervals, and QRS_a and T_a. The lower row in each lead shows the p-value obtained by comparing the two groups using the t-student test, after verifying the normality of the results.

Marker	Clinical ECG data			Computational Models	
	Control (n=60)	IUGR (n=33)	p -value	Control (\mathcal{C})	IUGR (\mathcal{G}_H)
QRS_d (ms)	83 (74 - 89)	87 (81 - 90)	0.039	67	68
$T_{pe,c}$ (ms)	76 (74 - 81)	78 (76 - 83)	0.030	78	78
QT_c (ms)	391 (376 - 406)	389 (381 - 399)	0.703	345	344
$T_{pe,c}/QT_c$	0.196 (0.188 - 0.207)	0.202 (0.196 - 0.212)	0.020	0.226	0.226
QRS_a (mV)	2.9 (2.4 - 3.5)	3.1 (2.3 - 3.6)	0.553	1.86	2.04
T_a (mV)	0.8 (0.6 - 1.0)	0.7 (0.5 - 0.9)	0.318	1.21	1.33

Table 4.2: Median and interquartile range and p -value for QRS_d , $T_{pe,c}$, QT_c , and $T_{pe,c}/QT_c$ measured on the optimally spatial transformed leads (PCA_{QRS} and PCA_T), on the control and IUGR subjects groups. The two most right columns show the results obtained in the simulation of the control and IUGR models, taking the median value of the beats.

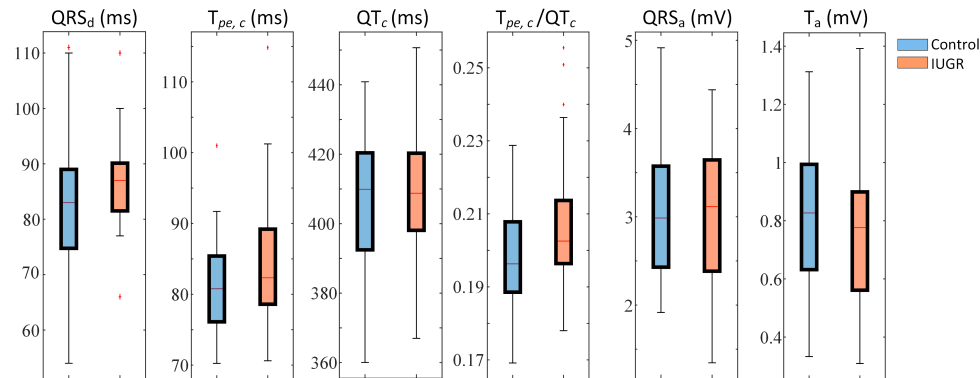


Figure 4.5: Changes in $T_{pe,c}$, QT_c , $T_{pe,c}/QT_c$, and QRS width for control (blue) and IUGR (orange) groups measured on the optimally spatial transformed leads (PCA_{QRS} and PCA_T). Central red lines indicate the median and the bottom and top edges of the box show the 25th and 75th percentiles, respectively.

4.2.2 Intervals result on PCA_{QRS} and PCA_{T} transform leads

Following the analysis of each of the 8 ECG leads from the clinical data, we proceeded to conduct the analysis on the new PCA_{QRS} and PCA_{T} leads. The IUGR group exhibited a significantly prolonged $T_{pe,c}$ compared to the control group, along with a similar increase in the $T_{pe,c}/QT_c$ ratio. The QT_c remained unchanged without significant variation, as shown in Figure 4.5 and Table 4.2. The amplitude value of the T-wave did not show a significant difference (Control=0.826(0.631-0.993) mV, IUGR=0.776(0.561-0.899) mV, p -value=0.318). In the control group, the $T_{pe,c}$ value of one subject was excluded due to a reduced RR interval, which resulted in overcorrection of heart rate using Fridericia's formula, leading to an outlier $T_{pe,c}$ value. In the IUGR group, manual correction of the T-wave end delineation was performed for two subjects due to an overshoot T-wave end in the PCA lead that led to early detection of this point.

The results for the analysis of the QRS_d can be observed in Figure 4.5. The IUGR group exhibited a significantly longer QRS_d compared to the control group, as shown in Table 4.2. Regarding the amplitudes ratio, no significant differences were observed.

For the simulation of the globular model, the \mathcal{G}_H model previously defined in Section 3.2.3 was used, which incorporated the geometric changes observed in IUGR subjects [13]. The results showed an increase of 1 ms in QRS_d in the globular model. During the depolarization phase, the T_{pe} interval remained unchanged, while the QT interval showed a reduction of 1 ms. Both QRS_a and T_a exhibited an increase in the globular model simulation of approximately 9% compared to the amplitude values of the control model.

4.3 Discussion

The present chapter focused on the analysis of changes in QRS_d , $T_{pe,c}$ and QT intervals in two groups of preadolescents: control and IUGR. The analysis was performed on the 8 independent standard ECG leads of the subjects and subsequently on the newly generated spatially transformed PCA_{QRS} and PCA_{T} leads. It also extended the analysis to the simulation of two computational models, one representing control and the other IUGR. To simulate IUGR, the sphericity index (calculated as base-apex length divided by basal diameter) was intentionally decreased, reflecting the cardiac anatomical changes observed in individuals diagnosed with IUGR (see Section 2.3).

For the correction of T_{pe} and QT, the Fridericia's formula was used having a wider range of proper correction than other formulas as Bazett's one, and still being general in application [129].

The results of interval measurements across the leads show high variability among them. Starting with QRS_d , statistically significant differences was found in lead II (p -value=0.0153). For $T_{pe,c}$, a significant difference was found in lead V4 with a p -value=0.005. In the QT interval, no significant difference was found in any lead. However, for the $T_{pe,c}/QT_c$ ratio, a significant difference was observed in lead V4 with a p -value=0.0164. Finally, the QRS_a showed significant differences in leads I and V4 (p -value=0.004 and p -value=0.046 respectively), while no significant difference was observed in T_a in any lead. This variability in the results is one of the reasons for applying PCA to spatially transform the leads into a global lead, focused on the depolarization or repolarization phases, depending on the intervals of interest.

The IUGR cohort presented a significantly prolonged QRS_d compared to the control cohort (Table 4.2). This increase could be associated with a larger ventricular tissue volume (VTV), which delays electrical propagation, widening the QRS complex. Regarding the change in QRS_d , our results align with previous studies [53, 54], where its prolongation and a greater QT dispersion were also observed in [55]. We hypothesize that the increase in \mathcal{W} impacts the intervals, especially T_{pe} . To analyze the influence of geometric remodeling on electrophysiology, *in silico* tests were conducted in the Chapter 5.

When comparing the control and IUGR groups, using the PCA_{QRS} and PCA_T leads, the results for $T_{pe,c}$ showed a significant increase in the IUGR group, potentially associated to the widening of the left ventricular wall. However, in the simulations where sphericity was adjusted to replicate IUGR by primarily modifying the apex-to-base length, no difference in this parameter was observed between the control and IUGR models. The IUGR simulation model was deformed, reducing its SpI by 8.7%, in agreement with the morphological changes reported in [13]. Nonetheless, the maximum increase in the ventricular wall width in the model was minimal at the base of the left ventricular wall (0.2 mm), resulting in an insignificant change in the $T_{pe,c}$ duration (78 ms). The next chapter presents a study exploring the impact of increased ventricular wall width on the duration of T_{pe} .

The QT_c interval results from the clinical subjects showed no significant differences between the control and IUGR groups, results mirrored by the findings in the simulation. Both the $T_{pe,c}$ and QT_c markers were measured from the PCA_T first lead. The amplitude of the T-wave peak did not exhibit a

significant difference between the analyzed groups. For the analysis of the QRS complex interval duration, delineation was performed on PCA_{QRS} first lead. QRS_d showed more variability within the control group than in the IUGR group, with the IUGR group displaying significantly higher values (see Fig. 4.5). This increase in duration could be attributed to the increase in ventricular volume and \mathcal{W} , leading to a delay in electrical propagation, thus resulting in a widening of the QRS complex in the ECG. In the simulation, no significant differences were observed in this parameter. Regarding the amplitude of the R peak, a slight increase was observed in the IUGR group, compatible with a higher ventricular tissue volume, but it did not reach statistical significance.

4.4 Conclusions

Our findings suggest that cardiac anatomical remodeling in IUGR subjects leads to an increase in $T_{pe,c}$, compatible with the previously reported increase in relative wall thickness. This rise in $T_{pe,c}$ can be associated with an increased transmural dispersion; although this increase is relatively modest (2 ms). While such a change is associated with a higher risk of ventricular arrhythmia, the impact of various additional parameters including ionic remodeling that generally affect ventricular dispersion, and not considered in this study, should not be overlooked. Similarly, an increase in QRS_d is observed, which could be also linked to the increase in the width of the ventricular walls, which leads to the analysis in the next chapter.

CHAPTER 5

ELECTROPHYSIOLOGICAL ANALYSIS OF CARDIAC REMODELING IN INTRAUTERINE GROWTH RESTRICTION: INSIGHTS FROM COMPUTATIONAL MODELS

-
- 5.1 ECG biomarkers alterations as a consequence of IUGR**
 - 5.2 Computational modeling of human electrophysiology**
 - 5.2.1 Electrophysiological propagation
 - 5.2.2 Transmural and apico-basal heterogeneities
 - 5.2.3 ECG signal processing and the computation of biomarkers
 - 5.2.4 Globular anatomical models with reduced sphericity index
 - 5.3 Results**
 - 5.3.1 *In Silico* analysis of geometric effects on ECG biomarkers
 - 5.3.2 Relationship between geometric variations and ECG biomarkers
 - 5.3.3 Role of transmural heterogeneities
 - 5.3.4 Mechanisms behind the subtle T_{pe} changes compared to the larger QRS_d changes
 - 5.4 Discussion**
 - 5.4.1 Cardiac remodeling *in silico*
 - 5.4.2 Impact of left basal diameter ϕ and wall width W in QRS_d
 - 5.4.3 T_{pe} and QT intervals
 - 5.5 Limitations**
 - 5.6 Conclusion**

5.1 ECG biomarkers alterations as a consequence of IUGR

In chapter 4, an analysis was conducted on ECG signals from a cohort of preadolescents diagnosed with severe IUGR, providing an opportunity to investigate whether the changes in biomarkers reported during the newborn stage persist into later developmental stages. Although depolarization and repolarization biomarkers exhibited variations related to IUGR, the relationship between IUGR-induced geometric remodeling and changes in these electrophysiological biomarkers remains unclear. Furthermore, the underlying mechanisms driving these variations are also not well understood.

We hypothesize that the anatomical alterations in the basal diameter ϕ and the widening of the ventricular wall thickness \mathcal{W} may impact the morphology of both the QRS complex and the T-wave.

The primary aim of this chapter was to assess *in silico* how IUGR-induced anatomical remodeling, including a reduction in the sphericity index SpI and variations in wall thickness \mathcal{W} , affects these ECG biomarkers. For this purpose, 8 globular models were developed, distinct from those presented in Section 2.3, as they included an additional variation in \mathcal{W} . The models presented in this chapter are referred to as \mathcal{G}_1 to \mathcal{G}_8 .

5.2 Computational modeling of human electrophysiology

A realistic biventricular heart within a torso model was used for this study [97] as the control model (\mathcal{C}), and was later deformed to generate globular IUGR models (\mathcal{G}). The \mathcal{C} model was meshed using tetrahedral elements ($\sim 330\,000$ nodes and $\sim 2\,000\,000$ elements).

The ORd AP model for healthy tissue [25, 130] was employed to simulate the cellular electrophysiological behavior of the ventricles. To model the propagation of electrical impulse across the myocardium, we utilized the monodomain model [74] through the finite element method [131], defined by the reaction-diffusion equation 2.9.

Extracellular potentials were calculated at the positions of virtual electrodes \mathbf{e} using a torso model to generate a virtual 12-lead ECG [86]. The same coordinates were used in all simulations. Extracellular potentials were computed

from ventricular potentials following the equation 2.19:

After pre-pacing the cellular model to achieve steady state conditions, a sequence of three beats was simulated at a frequency of 60 bpm (RR=1000 ms), using a stimulus amplitude of 200 mA with a 0.5 ms duration. The third beat was selected to ensure that the state variables involved in the cellular model reached steady state conditions. A dual adaptive explicit time integration method as described in [77] was employed, with an adaptive time step ranging from 0.01 to 0.1 ms.

The globular models generated for this stage of the research employed the methodology developed in Section 3.2.3, resulting in 8 models. These models varied in geometric properties, as will be explained in Section 5.2.4.

5.2.1 Electrophysiological propagation

The electrical propagation used in this stage was based on the methodology proposed in Section 3.1.1, where the electrical stimulus initiated at the bundle of His and spread through a Purkinje network, which couples to the myocardium at discrete sites (PMJs), see Fig. 5.1a.

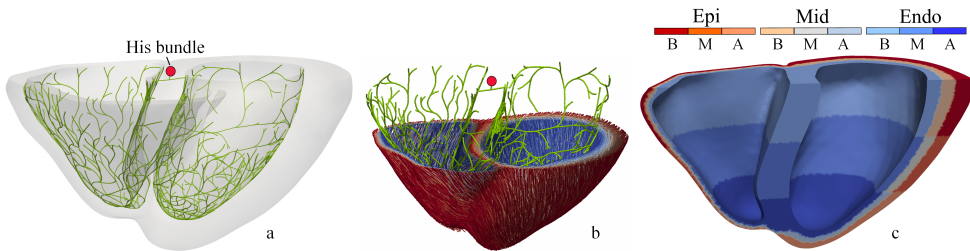


Figure 5.1: a: Implementation of the Purkinje network on the endocardial surface of the models. The red circle indicates the His Bundle where electrical propagation begins. b: Implementation of fibers and propagation direction at each node from the endocardial to the epicardial surface. c: Division of the tissue into 9 zones incorporating transmural (endo, mid, and epi tissue) and apicobasal heterogeneities (base (B), middle (M), and apex (A)).

The Purkinje network was generated using a fractal projection method [99], incorporating a posterior main branch to achieve QRS morphologies within clinical ranges. To ensure the rapid electrical conduction at 2.9 m/s, a diffusion coefficient of $0.013 \text{ cm}^2/\text{ms}$ was set along the Purkinje network [132]. At the PMJs, this value was reduced to $0.0023 \text{ cm}^2/\text{ms}$, modelling the transition to the myocardial tissue. The Purkinje cellular AP was represented using the Stewart model [20]. The Purkinje network was meshed with an average edge

length of $750 \mu\text{m}$. First, a network was generated for the \mathcal{C} model and later adapted to fit the modified endocardial surface of each of the \mathcal{G} models, while maintaining the same number of nodes and segments across all models ($\sim 7\,000$ nodes and elements), as shown in Fig. 5.2, with orange representing the control model and blue representing the globular model \mathcal{G}_6 (see Sec 5.2.4). The onset of the electrical activation was set in all simulations at the same spatial point corresponding to the His bundle.

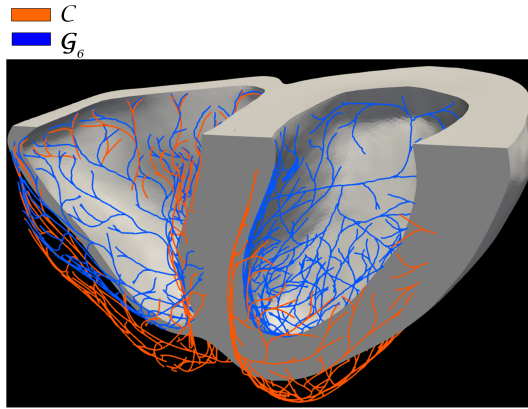


Figure 5.2: Purkinje network for the control model in orange and the globular model \mathcal{G}_6 in blue. The same network was adapted to the endocardial surface of the globular models.

Within the myocardial tissue, electrical propagation followed a fibre architecture defined by a rule-based method [104] (see Section 3.1.2). The fiber orientation exhibited a counterclockwise rotation from the apex to the base, with fiber angles gradually transitioning from -60° at the endocardium to $+60^\circ$ at the epicardium across both ventricles (see Fig. 5.1b). The myocardial tissue was modeled with orthotropic conductivity and transverse isotropy, i.e. with identical conductivities in the sheet and normal-sheet directions. A transverse-to-longitudinal conductivity ratio of 0.25 was applied, introducing CV anisotropy consistent with experimentally observed cardiac tissue behavior [133]. The longitudinal diffusion coefficient was set at $0.0013 \text{ cm}^2/\text{ms}$, complemented by a membrane capacitance of $1 \text{ pF}/\text{cm}^2$. This configuration resulted in an average longitudinal CV of 0.67 m/s within the myocardium [132].

5.2.2 Transmural and apicobasal heterogeneities

The spatial distribution of transmural heterogeneity in membrane kinetics was modelled by incorporating distinct endocardial, midmyocardial and epicardial

cell layers with varying relative thicknesses, see Fig. 5.1c. Specifically, the RV and LV wall thickness was distributed such that 30% was allocated to endocardial cells, 30% to mid-myocardial cells, and 40% to epicardial cells [134] with the interventricular septum modelled entirely as endocardial cells, as described in Section 3.2.1.

Additionally, electrophysiological heterogeneities were introduced along the apex-base axis to reflect the longer APD observed at the base compared to the apex. The model was segmented into three regions: apex, middle and base, each assigned a distinct factor, decreasing the conductance G_{K_s} , and thereby reducing the magnitude of the slow potassium current I_{K_s} . This was achieved by scaling the conductance of the slow delayed rectifier potassium current (G_{K_s}), based on findings by [108], which reported significant differences in the expression levels of proteins forming the I_{K_s} channel between the apical and basal regions of the heart. Specifically, G_{K_s} was reduced scaling factor: 5 at the apex, 2.6 in the middle, and 0.2 at the base, as described in Section 3.2.2. These repolarization heterogeneities were applied consistently to both the control $\mathcal{C}(30-30-40)$ model and each of the globular $\mathcal{G}(30-30-40)$ models.

Additionally, the impact of transmural repolarization variability on the analyzed ECG biomarkers, particularly those related to repolarization, was assessed by reducing the width of the midmyocardial layer, the region with longer APD values. For this purpose, the control \mathcal{C} model and the globular \mathcal{G}_7 model, see Section 5.2.4, were configured with 48% of endocardium, 4% midmyocardium, and 48% epicardium, denoted as $\mathcal{C}(48-4-48)$ and $\mathcal{G}_7(48-4-48)$, respectively (Fig. 5.3). The methodology and algorithms used to generate these models are described in Section 3.2.1.

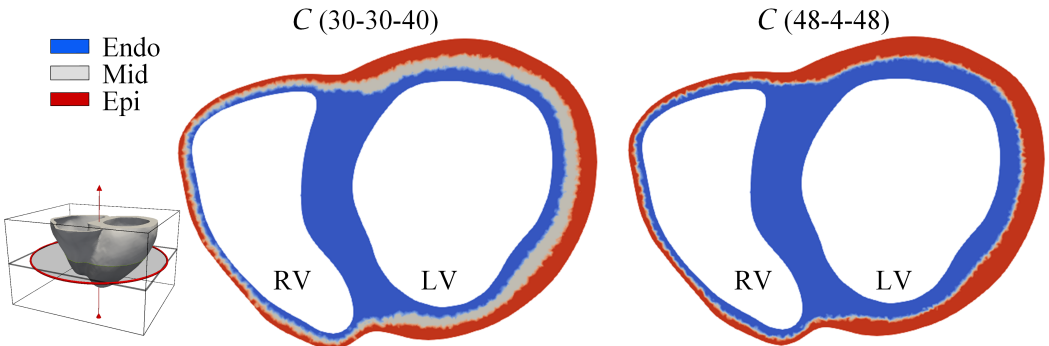


Figure 5.3: Cross-sectional view of the control model $\mathcal{C}(30-30-40)$ with 30% endocardium, 30% mid-myocardium, and 40% epicardium, and for $\mathcal{C}(48-4-48)$ model with its corresponding transmural distribution.

Extracellular potentials were calculated at the positions of virtual electrodes using a torso model to generate a virtual 12-lead ECG, with the same sampling rate than in real recording, 1000 Hz. The onset, peak, and endpoint of the synthetic ECG waves were identified through their delineation on the transformed leads obtained by applying PCA to the 8 independent virtual leads, following the same process described in Section 2.4.4.

5.2.3 ECG signal processing and the computation of biomarkers

The virtual 12-lead ECG signals were delineated using a wavelet-based delineator [125] as described in Section 4.1.2. The onset and end of the QRS complex and T-wave were identified using a single-lead delineation method enhanced by a multilead-based rule technique, ensuring accurate and lead-independent marks [89]. PCA was applied to create two spatially transformed leads: PCA_{QRS} , optimized for the QRS complex, and PCA_{T} , focused on the T-wave to improve delineation accuracy. PCA_{QRS} was used to identify the beginning, peak, and end of the QRS complex, while PCA_{T} was used for the T-wave [92]. This approach enhanced precision by tailoring each lead to the specific waveform, as shown in Fig. 5.4.

Subsequently, the median value of the QRS_d across beats was calculated and considered representative for each patient. T_{pe} and QT intervals were measured in each beat in lead PCA_{T} and T_{pe}/QT ratio was also determined.

5.2.4 Globular anatomical models with reduced sphericity index

The geometric changes resulting from IUGR were represented by constructing eight globular \mathcal{G} models. These models were developed departing from the control \mathcal{C} model and reducing its SpI plus increasing the width \mathcal{W} of the left ventricular wall. The methodology used to generate these models is detailed in Section 3.2.3.

Geometrical models were remeshed to achieve the same target edge length ($887 \mu\text{m}$). This was done by remeshing the surface using an in-house implementation of the algorithm outlined in [135], resulting in a surface mesh of high quality, as expected from state-of-the-art techniques. The surface mesh was then used as input for Tetgen [136]. As is typical in state-of-the-art practices, optimal quality parameters were employed to generate high-quality tetrahedral meshes.

Regarding the tetrahedral meshes, the quality metrics “radius ratio” and “scaled jacobian” were evaluated, both computed with VTK (<https://vtk.org>).

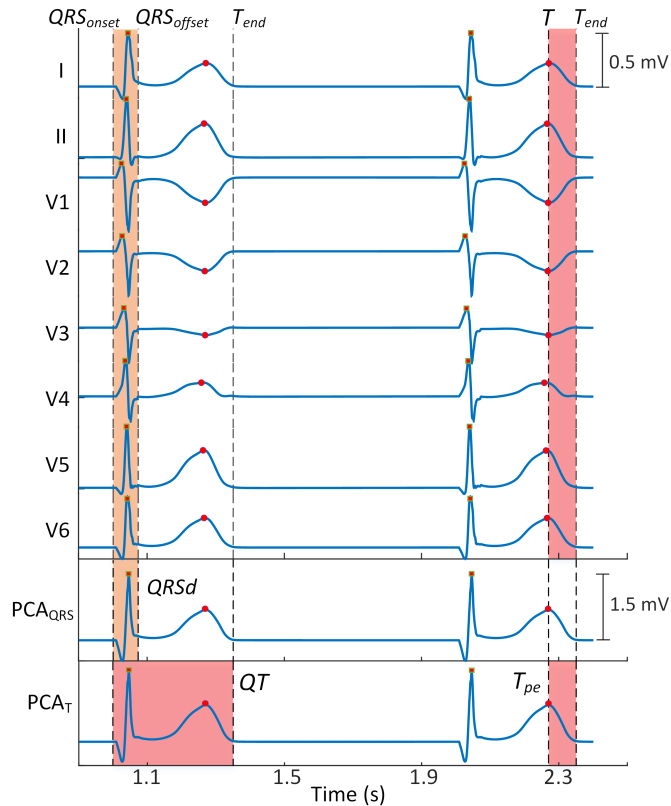


Figure 5.4: The standard 8-leads ECG, from the simulated control \mathcal{C} model, with marks on QRS and T-wave onset and end points indicated with black dashed lines, and QRS and T peaks with red squares and circles, respectively. QRS_d interval measured over PCA_{QRS} is shaded in orange and T_{pe} and QT intervals measured over PCA_T are shaded in red.

org/doc/nightly/html/classvtkMeshQuality.html). In practice, tetrahedra with a radius ratio value less than 3 are typically considered to be of good quality for FEM simulations. The meshes used in this work ensure that more than 95% of the elements meet this condition for each geometry utilized. Regarding the scaled jacobian, tetrahedra with values greater than 0.2 are regarded as having good quality, and over 95% of the tetrahedra in all the meshes used in this work satisfy this criterion.

To assess model convergence, we performed simulations on the control model using a finer mesh (edge length=400 μm). This resulted in only a 1 ms reduction in QRS duration, indicating minimal impact on activation. Based on this small difference, we chose to proceed with the coarser mesh (887 μm)

for this study.

The different geometric variations corresponding to each of these \mathcal{G}_i models are observed in Fig. 5.5. The variation in \mathcal{L} of the \mathcal{G}_i models relative to the \mathcal{C} model had a median value of 6.9(4.6-9.6) mm, while ϕ showed a median of 2.3(0.4-2.6) mm. The globular models are organized considering \mathcal{W} , and their detailed descriptions are as follows:

- Model \mathcal{G}_1 : this model was generated by deforming the \mathcal{C} model through the application of surface traction. The percentage variation in ϕ and \mathcal{L} were based on the average findings from [13], with increases of 2.7% and reductions of 6.6%, respectively. This model has an 8.4% reduction in the left SpI and an increment of 2.3% in \mathcal{W} relative to the \mathcal{C} model. The detailed methodology for generating the globular model was outlined in Section 3.2.3 [64]. This initial globular model maintains a percentage of geometric change relative to the globular models \mathcal{G}_G and \mathcal{G}_H used in the Chapter 3.
- Model \mathcal{G}_2 : this globular model aimed to generate a more pronounced deformation, pushing the boundaries of variability as presented in [13]. The left SpI was reduced by 16%, with greater expansion of ϕ and further reduction of \mathcal{L} compared to \mathcal{G}_1 . The increment in \mathcal{W} was 2.3% relative to the \mathcal{C} model.
- Model \mathcal{G}_3 : in this model, the left SpI was reduced by 14.8%, an increment of 7.1% in \mathcal{W} and 5% reduction in VTV compared to the \mathcal{C} model.
- Model \mathcal{G}_4 : in this model, \mathcal{W} increased by 7.3% compared to the \mathcal{C} model.
- Model \mathcal{G}_5 : the \mathcal{C} model was modified by applying surface traction to the epicardial tissue, increasing the left \mathcal{W} by approximately 4 mm (22.0% compared to \mathcal{C}). This increase led to a 9.9% increase in VTV compared to the \mathcal{C} model, with a corresponding reduction in left SpI of 10.9%.
- Model \mathcal{G}_6 : this model featured extreme thickening of \mathcal{W} (33.8% compared to \mathcal{C}) along with a reduced basal diameter ϕ . The left ϕ was reduced by 16% and \mathcal{L} by 21%. This produced a reduction of approximately 5% in the left SpI. This model drastically reduced the left ventricular cavity such that the total VTV of the model increased minimally by 0.04% compared to the \mathcal{C} model.
- Model \mathcal{G}_7 : this model displayed moderate changes. The left ϕ increased by 0.44% and \mathcal{L} was reduced by 8.6%. This resulted in a reduction of

8.5% in the left SpI. There was an increase in \mathcal{W} by 35.3% and VTV by 8.6% [137].

- Model \mathcal{G}_8 : This model exhibited an approximately 40% increase in muscular mass compared to the \mathcal{C} model. The left SpI was reduced by 14.4%,. The \mathcal{W} by 40.7% and VTV increased by 35.89%.

The VTV can be seen as an aggregated surrogate of a global heart size change, fusing apex-base, basal diameter and wall modifications. To evaluate the impact of geometric changes on the depolarization and repolarization phases, the electrophysiological characteristics of the \mathcal{G}_i models, including fiber orientation, ventricular heterogeneities and CV, were kept as in the \mathcal{C} model. Only the Purkinje network was adjusted to adapt to the new dimensions of the endocardial surface of the \mathcal{G}_i models. Table 1 shows the variations in basal diameter ϕ , apex-base length \mathcal{L} , wall thickness \mathcal{W} , and VTV for the eight globular models \mathcal{G}_i with $i \in \{1, \dots, 8\}$, compared to the \mathcal{C} model.

Model	Left ventricle				Right ventricle			VTV (cm ³)
	\mathcal{L} (mm)	ϕ (mm)	SpI	\mathcal{W} (mm)	\mathcal{L} (mm)	ϕ (mm)	SpI	
\mathcal{C}	69.5	45.8	1.5	13.1	57.3	42.4	1.4	139.8
\mathcal{G}_1	65.0	47.0	1.4	13.4	53.0	42.0	1.3	131.0
\mathcal{G}_2	61.1	48.2	1.3	13.4	51.1	41.1	1.2	125.3
\mathcal{G}_3	61.7	48.0	1.3	14.0	51.0	41.8	1.2	132.6
\mathcal{G}_4	64.9	48.5	1.3	14.0	53.3	41.5	1.3	131.0
\mathcal{G}_5	64.8	48.2	1.3	16.0	54.4	41.1	1.3	153.6
\mathcal{G}_6	54.9	38.3	1.4	17.5	48.1	42.7	1.1	139.8
\mathcal{G}_7	63.5	46.0	1.4	17.7	52.7	42.6	1.2	151.9
\mathcal{G}_8	59.4	46.0	1.3	18.4	49.3	42.6	1.2	189.9

Table 5.1: Measurements of \mathcal{L} , ϕ , \mathcal{W} and ratio SpI in both ventricles for the \mathcal{C} and \mathcal{G} models. \mathcal{W} shows the maximum width of the LV measured at the base and the last column show the VTV of the entire ventricular mesh models.

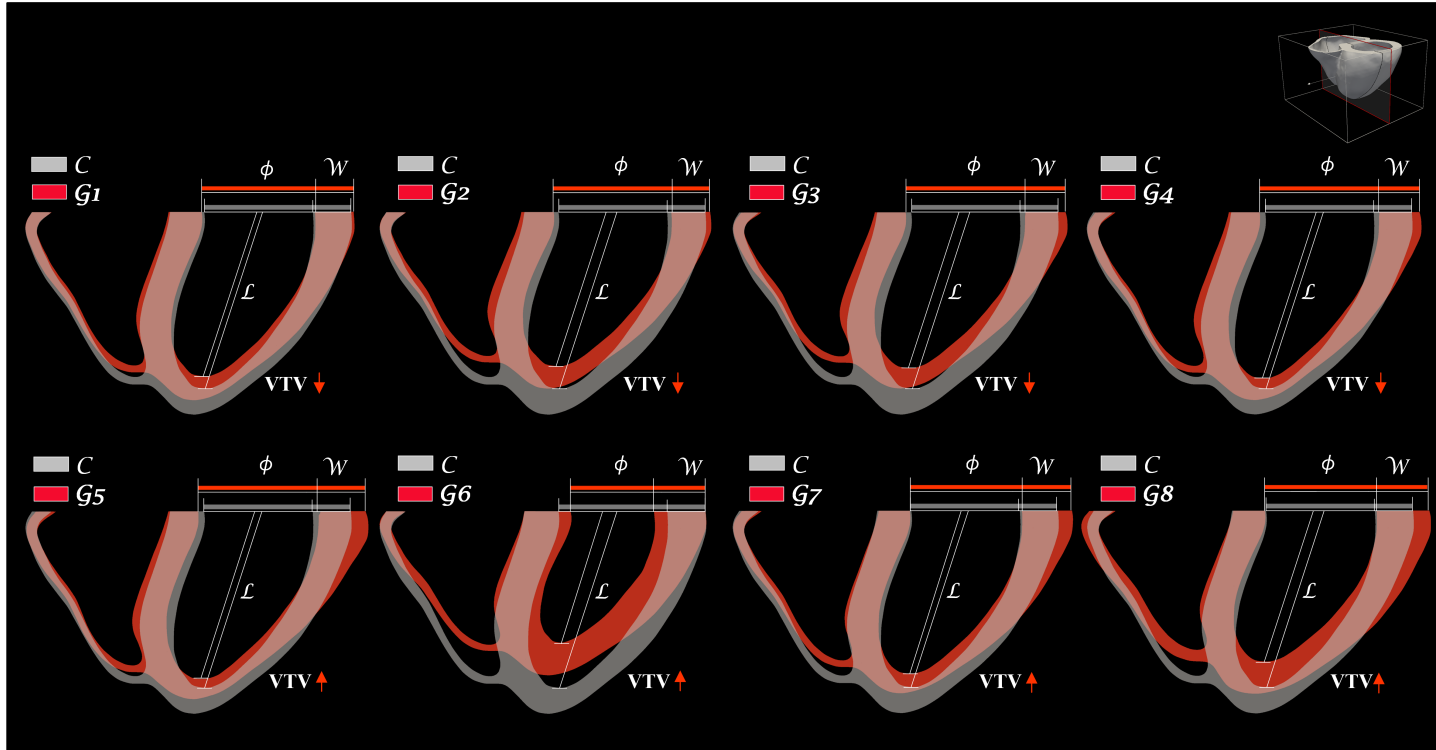


Figure 5.5: Eight \mathcal{G} models generated from \mathcal{C} model. The cross-section of the models allows for the observation of changes in \mathcal{L} , ϕ , SpI, \mathcal{W} , and VTV. The direction of the arrows indicates the direction of change in the simulated parameters.

To analyze the impact of the increase in the left ventricular wall thickness \mathcal{W} , we examined the APD in three nodes of the heart mesh in the basal region: one in the endocardial section and two in the epicardial section. The ventricular wall thickness \mathcal{W} , which varies across different globular models, was quantified as shown in Fig. 5.6. The positions were determined as follows: P1 corresponding to moving 15% of \mathcal{W} from endocardium, P2 moving 85% of \mathcal{W} , and P3 located on the epicardial surface. The extreme nodes at 0% (endo) and 100% (epi) of \mathcal{W} were selected and nodes P1 and P2 are selected as lying on the line, connecting the endo and epi nodes. To determine the exact locations of P1 and P2, a linear interpolation was first performed. Subsequently, the mesh nodes closest to these theoretical P1 and P2 points were identified, ensuring they lay within a radius of less than $887 \mu\text{m}$, corresponding to the edge length of the mesh elements. Once the spatial coordinates of the three points were identified, the nearest nodes to the calculated positions were located, and the AP was analyzed at these nodes.

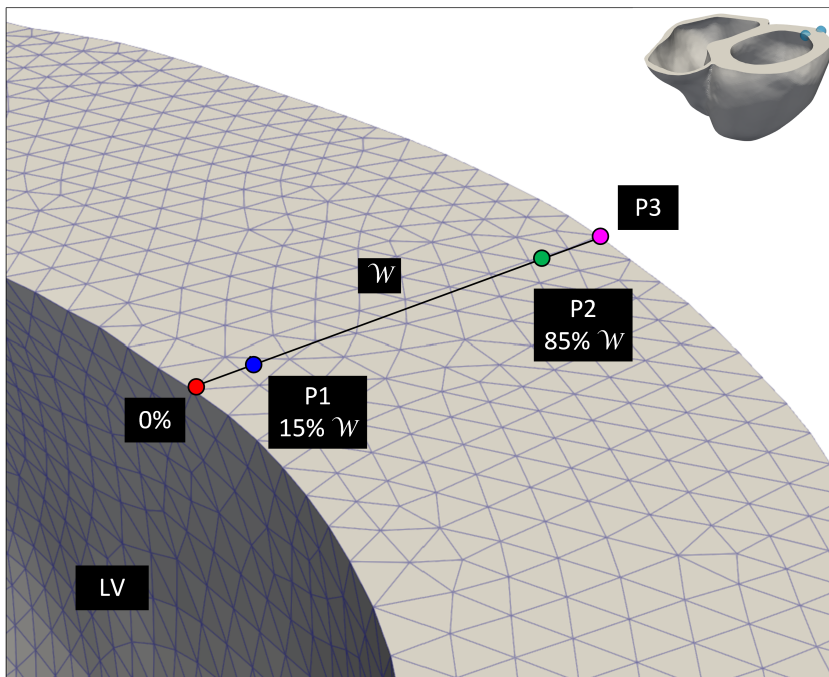


Figure 5.6: Selection of endocardial and epicardial nodes for AP analysis. The ventricular wall thickness was divided into percentages, with one node selected in the basal endocardial section (P1-blue circle) and two nodes in the epicardial section (P2-green circle and P3-magenta circle).

All measurements for computing results were taken from the third simulated heartbeat. QRS complex measurements were performed on the PCA_{QRS} lead, whereas measurements of the T-wave were performed on the PCA_{T} lead. The association between the resulted values for QRS_d , T_{pe} and the QT interval and changes in \mathcal{L} , ϕ , and \mathcal{W} was assessed using multiple linear regression.

5.3 Results

Markers	ECG Intervals (ms)				Waves amplitude (mV)	
a. Clinical result preadolescents, median(IQR)						
Dataset	QRS_d	$T_{pe,c}$	QT_c	$T_{pe,c}/\text{QT}_c$	QRS_a	T_a
Control	83(74-89)	76(74-81)	391(376-406)	0.196(0.188-0.207)	2.9(2.4-3.5)	0.8(0.6-1.0)
IUGR	87(81-90)	78(76-83)	389(381-399)	0.202(0.196-0.212)	3.1(2.3-3.6)	0.7(0.5-0.9)
p-value	0.039	0.031	0.703	0.026	0.553	0.318
b. Computational Simulations						
Model	QRS_d	T_{pe}	QT	T_{pe}/QT	QRS_a	T_a
\mathcal{C}	64.0	76	340	0.223	1.86	1.21
\mathcal{G}_1	69.0	78	344	0.226	1.76	1.29
\mathcal{G}_2	69.5	77	341	0.225	1.69	1.33
\mathcal{G}_3	72.0	75	343	0.218	2.25	1.18
\mathcal{G}_4	71.5	76	344	0.220	2.18	1.18
\mathcal{G}_5	81.5	78	343	0.227	1.78	1.37
\mathcal{G}_6	67.0	78	341	0.228	2.31	1.33
\mathcal{G}_7	76.0	79	344	0.229	2.04	1.33
\mathcal{G}_8	75.0	79	345	0.229	2.13	1.31

Table 5.2: a: ECG biomarkers from clinical data in preadolescents: control cohort (n=60) and IUGR cohort (n=33). b: ECG biomarkers computed from simulations across the \mathcal{G}_i models. All simulations used $\text{RR}=1$ s, so QT and T_{pe} correspond to their corrected QT_c and $T_{pe,c}$, respectively.

5.3.1 In Silico analysis of geometric effects on ECG biomarkers

The *in silico* study explored the impact of geometric changes associated with IUGR on depolarization and repolarization ECG biomarkers using the different globular electrophysiological models, all derived from the biventricular control \mathcal{C} model. As shown in Table 5.2b, the simulations revealed significant changes in QRS_d along with more subtle changes in T_{pe} , all of which align with the clinical findings listed in the top of Table 5.2a.

QRS_d values measured in PCA_{QRS} leads across all models, shown in Table 5.2b and illustrated in Fig. 5.7, reveal an increase relative to control \mathcal{C} , ranging

from 3 ms in \mathcal{G}_6 to 17.5 ms in \mathcal{G}_5 .

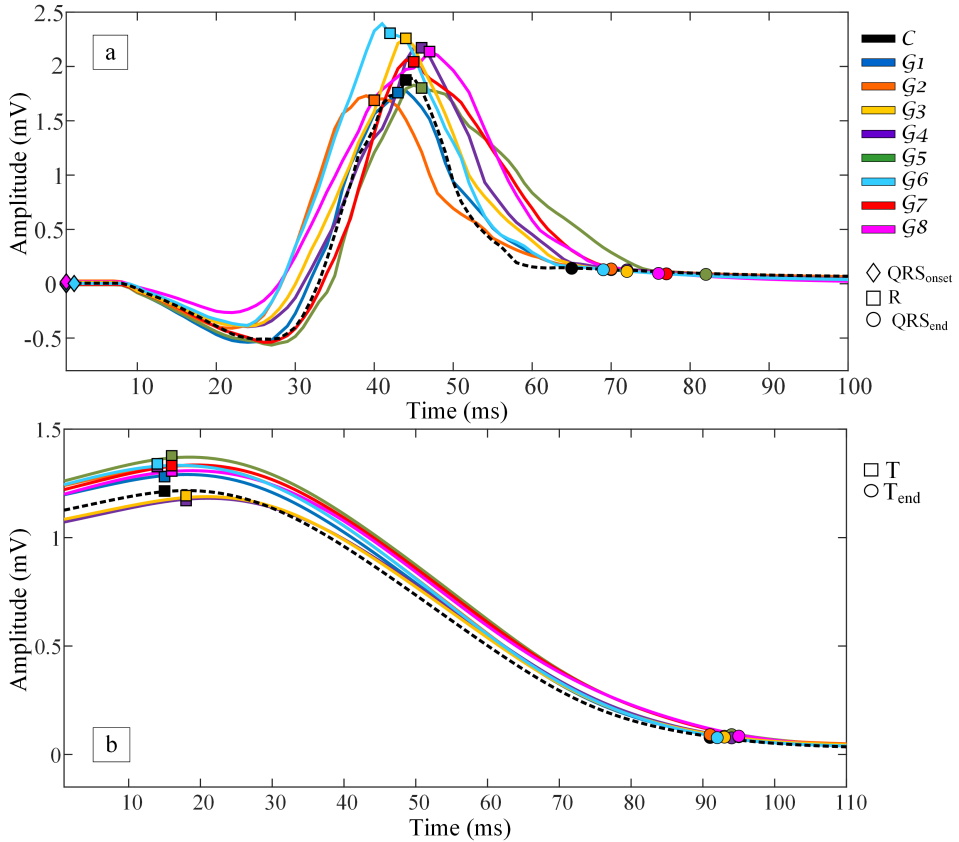


Figure 5.7: a: QRS complex in lead PCA_{QRS} of the \mathcal{C} model and \mathcal{G}_i models, with the marks of the $\text{QRS}_{\text{onset}}$, QRS peak, and the QRS_{end} . b: T_{pe} in PCA_T lead of the \mathcal{C} and \mathcal{G}_i models with the marks of the T peak, and the T_{end} .

Measurements of T_{pe} and QT intervals in the PCA_T lead as illustrated in Fig. 5.7b, showed minor fluctuations, in line with clinical findings. T_{pe} increased in six of the eight models, with a maximum increase of 3 ms in \mathcal{G}_7 and \mathcal{G}_8 . The QT interval increased across all models, ranging from a 1 ms increase in \mathcal{G}_2 and \mathcal{G}_6 to a 5 ms increase in \mathcal{G}_8 . The increase in T_{pe} in the globular models is similar to that found in clinical measurements, with a median value of 2 ms. QT, on the other hand, shows a change in the opposite direction to the clinical results, with a median increase of 3.5 ms in the globular models. T_{pe}/QT ratio increases in the globular models, in agreement with the clinical results.

The geometric changes in the globular models resulted in small changes in QRS_a , as shown in Table 5.2b. The globular models exhibited an increase in QRS_a (median=2.09 mV) compared to the control model, consistent with clinical findings. Conversely, T_a amplitude in the globular models also showed an increase (median=1.32 mV), which contrasts with the trends observed in clinical results.

The Table 5.2a include the results obtained in Chapter 4 to facilitate comparison with the results from the computational simulations. In the clinical results, the comparison between the control and IUGR cohorts revealed differences in the ECG interval measurements. The IUGR cohort showed a significant median increase of 4 ms in QRS_d , with hardly any changes in QRS wave amplitude (QRS_a) compared to the control cohort. Additionally, the IUGR cohort demonstrated a significant but moderate increase of 2 ms in median in $T_{pe,c}$ and $T_{pe,c}/QT_c$ ratio. Although the QT_c interval as well as the T-wave amplitude (T_a) were slightly lower in the IUGR cohort, these decreases were not statistically significant.

5.3.2 Relationship between geometric variations and ECG biomarkers

Table 5.3 presents the results of the multiple linear regression analysis examining the relationship between the geometric properties $\{\mathcal{L}, \phi, \text{ and } \mathcal{W}\}$ and the biomarkers measured from the synthetic ECG. Each of the ECG biomarkers was modeled as a linear combination of the three modified geometric parameters, which were treated as independent variables. This allowed us to assess both the extent to which anatomical variables account for changes in ECG biomarkers and the individual contribution of each anatomical variable to the ECG biomarker values.

The multiple regression analysis shows that anatomical variables contribute more significantly to QRS_d and to a lesser extent to T_{pe} . In the regression model that considers individual variables, none of the three anatomical variables (ϕ , \mathcal{L} , and \mathcal{W}) individually explain the variability of any of the markers, except for the contribution of \mathcal{W} to T_{pe} ($\mathcal{B}=0.50$, $p\text{-value}=0.019$).

When combining the independent geometric variables in pairs, the combination of ϕ and \mathcal{W} significantly contributes to QRS_d ($\mathcal{B}=1.40$ and 2.22 , with $p\text{-values}=0.010$ and 0.007 , respectively). For T_{pe} , in the same combination, \mathcal{W} shows a significant value ($\mathcal{B}=0.52$, $p\text{-value}=0.044$). In the same ECG biomarker, but in the combination of \mathcal{L} and \mathcal{W} , the latter shows a significant value ($\mathcal{B}=0.57$, $p\text{-value}=0.039$).

Marker	QRS _d				T _{pe}				QT			
	B	p _i	R ²	p _F	B	p _i	R ²	p _F	B	p _i	R ²	p _F
Individual variables												
ℒ	-0.04	0.930	0.001		-0.11	0.382	0.11		-0.02	0.901	0.002	
ϕ	0.65	0.297	0.15		-0.14	0.400	0.10		0.19	0.344	0.13	
ℳ	1.19	0.188	0.23		0.50	0.019	0.57		0.32	0.297	0.15	
Pairs combined variables												
ℒ	-0.58	0.339			-0.07	0.673			-0.19	0.360		
ϕ	1.13	0.176	0.28	0.370	-0.08	0.718	0.13	0.655	0.35	0.208	0.25	0.421
ℒ	0.50	0.380	0.33	0.297	0.06	0.601	0.59	0.071	0.12	0.550	0.21	0.500
ℳ	1.76	0.135			0.57	0.039			0.45	0.261		
ϕ	1.40	0.010			0.03	0.819			0.40	0.055		
ℳ	2.22	0.007	0.77	0.013	0.52	0.044	0.57	0.080	0.61	0.050	0.56	0.084
All three variables together												
ℒ	-0.06	0.885			0.06	0.670			-0.05	0.794		
ϕ	1.43	0.028	0.77	0.048	0.00	0.987	0.59	0.188	0.43	0.095	0.57	0.206
ℳ	2.18	0.023			0.57	0.066			0.58	0.113		

Table 5.3: Multiple regression analysis between the geometric variables of globular models {ℒ, ϕ, and ℳ} and the QRS_d, T_{pe} and QT intervals measured in the synthetic ECG. p_i indicates the p-value for each individual variable, while p_F represents the significance value of the model. Values with p-value < 0.05 are highlighted in bold.

Combining all three variables together, the anatomical variables have a strong contribution to QRS_d, accounting for 77% of its variance. \mathcal{B} value revealed that increases in both basal diameter ϕ ($\mathcal{B}=1.43$, p -value=0.028) and left ventricular wall thickness \mathcal{W} ($\mathcal{B}=2.18$, p -value=0.023) lead to an increase in QRS_d. In contrast, the apex-to-base length \mathcal{L} has minimal impact on QRS_d.

Unlike QRS_d, T_{pe} and QT intervals exhibited a moderate correlation with the anatomical parameters ($R^2=0.59$ and 0.57 , respectively), with the increase in wall thickness \mathcal{W} being the most significant anatomical factor contributing to the enhancement of these repolarization features ($\mathcal{B}=0.57$ and 0.58 , respectively).

5.3.3 Role of transmural heterogeneities

The impact of electrophysiological transmural heterogeneities on the findings of this study was evaluated by reducing the midmyocardial layer (which has the longest APD values), thereby increasing the endocardial and epicardial layers in \mathcal{C} and \mathcal{G}_7 .

Changes in transmural heterogeneities did not affect QRS_d in either the control (64 ms) or globular heart models (76 ms), as shown in Table 5.4. This lack of impact is a consequence of the fact that removing the midmyocardial layer mainly affects the APD within the transmural wall, affecting the repolarization phase rather than the depolarization phase, which defines QRS_d.

Model \ Marker	ECG intervals (ms)				Amplitude (mV)	
	QRS _d	T _{pe}	QT	T _{pe} /QT	QRS _a	T _a
$\mathcal{C}(30-30-40)$	64	76	340	0.223	1.86	1.21
$\mathcal{C}(48-4-48)$	64	75	329	0.227	1.86	1.21
$\mathcal{G}_7(30-30-40)$	76	79	344	0.229	2.04	1.33
$\mathcal{G}_7(48-4-48)$	76	76	331	0.229	2.03	1.27

Table 5.4: Intervals and amplitudes measured on the control \mathcal{C} and globular \mathcal{G}_7 models with different transmural divisions: 30%, 30%, and 40% for endocardium, mid-myocardium, and epicardium, and 48%, 4%, and 48%, respectively.

Therefore, transmural heterogeneities show an impact on the repolarization T_{pe} and QT intervals. The removal of the midmyocardial layer resulted in a moderate reduction of T_{pe}, with a decrease of 1 ms in the control models and a 3 ms reduction in the globular model \mathcal{G}_7 . A reduction is seen in the QT interval, showing a decrease of 11 ms in the control models and 13 ms in the globular models. This reduction occurs because the removal of the midmyocardial layer enlarges the endocardial and epicardial regions, both of which exhibit shorter and more comparable APDs, leading to reduced repolarization dispersion and, consequently, shorter T_{pe} and QT intervals.

No significant effect of the midmyocardial reduction is observed on T_{pe}/QT or the maximum amplitudes QRS_a and T_a.

5.3.4 Mechanisms behind the subtle T_{pe} changes compared to the larger QRS_d changes

To gain a deeper insight into the subtle changes in T_{pe} compared to the significant change in QRS_d, we analyzed the AP at three node positions spanning from the endocardium to the epicardium across all globular models. These three nodes are transmurally distributed in all models: one is located at the center of the endocardial-base section (P1_{endo}), another at the center of the epicardial-base section (P2_{epi}), and the third on the external epicardial-base surface of the LV (P3_{epi-e}), which corresponds to the last region to depolarize.

To analyze the changes in the QRS complex, we examined the differences in activation time (AT) at each node across the different globular models, which represent the onset of depolarization. These ATs correspond to the APD at 90% repolarization (APD₉₀), a key metric that defines the APD. Figure 5.8a shows that the epicardial surface (P3_{epi-e}) consistently defines the end of activation (i.e., the region with the most delayed or longest AT) across all anatomical models.

Note that across the different $P3_{\text{epi-e}}$ nodes, the AT values vary between 54 and 65 ms, corresponding to the phase between the R and S waves of the QRS complex in Fig. 5.7, marking the end of activation. Additionally, beyond the impact of changes in \mathcal{L} and ϕ , we found that the thicker the ventricular wall, the longer it takes for $P3_{\text{epi-e}}$ to activate (highlighted by the magenta circle, which represents the model with the greatest wall thickness).

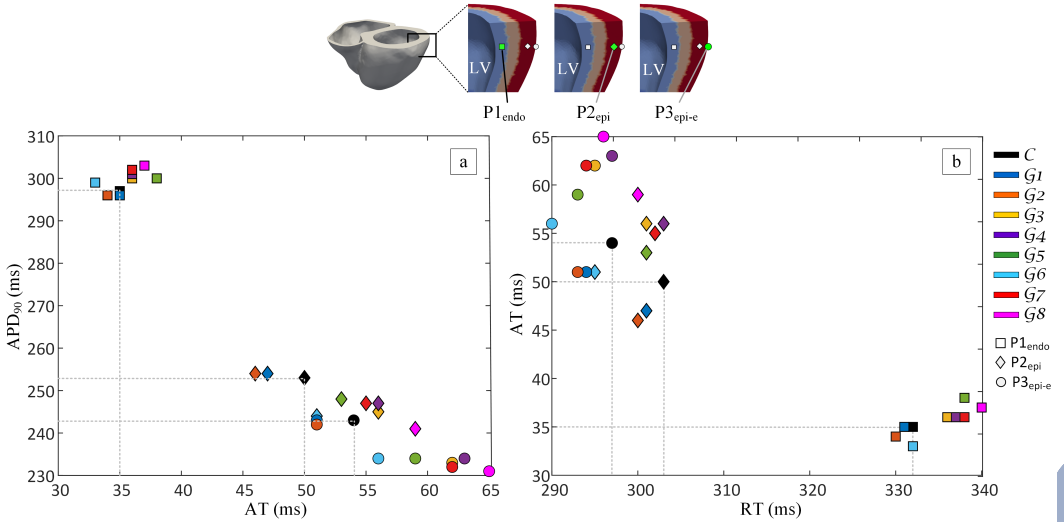


Figure 5.8: a: AT and APD at three nodes of the mesh, $P1_{\text{endo}}$ on an intermediate node of the endo-base section, $P2_{\text{epi}}$ on the middle epi-base section, and $P3_{\text{epi-e}}$ on the external surface of the epi-base section. b: A contrast between RT and AT is presented, considering the three selected nodes. The upper part of the figure outlines the location of these nodes within the heart volume.

At $P1_{\text{endo}}$, AT values in the \mathcal{G}_i models shows low variability, averaging 35.6 ± 1.6 ms, close to the \mathcal{C} model's 35 ms. In contrast, at $P2_{\text{epi}}$, AT increases to 54.8 ± 4.6 ms and at $P3_{\text{epi-e}}$, it reaches 58.6 ± 5.4 ms. Several globular models display a delayed AT relative to the \mathcal{C} model.

The \mathcal{G}_i models showed an average APD₉₀ of 299.6 ± 2.6 ms at $P1_{\text{endo}}$, 247.5 ± 4.5 ms at $P2_{\text{epi}}$, and 235.3 ± 4.5 ms at $P3_{\text{epi-e}}$ (see Fig. 5.8a). At $P1_{\text{endo}}$, most \mathcal{G}_i models exceed the APD₉₀ of the \mathcal{C} model; however, this pattern reverses in the epi nodes, where APD₉₀ is shorter. This is attributed to the wider epicardial layer, which reduces the influence of the adjacent midmyocardium's longer APD₉₀ at the surface $P3_{\text{epi-e}}$. These differences may explain why the QT biomarker remains unchanged despite the significant widening of QRS_d .

Fig. 5.8b illustrates the repolarization time (RT) of each node across all

models, calculated as the sum of AT and APD90, expressed as $RT = AT + APD90$. The figure indicates that the endocardium is the last region to repolarize for all models, implying that the end of the T-wave is determined by the APD characteristics of the endocardium. Therefore, \mathcal{W} has minimal impact on the end of the T-wave and consequently has little effect on T_{pe} or QT intervals.

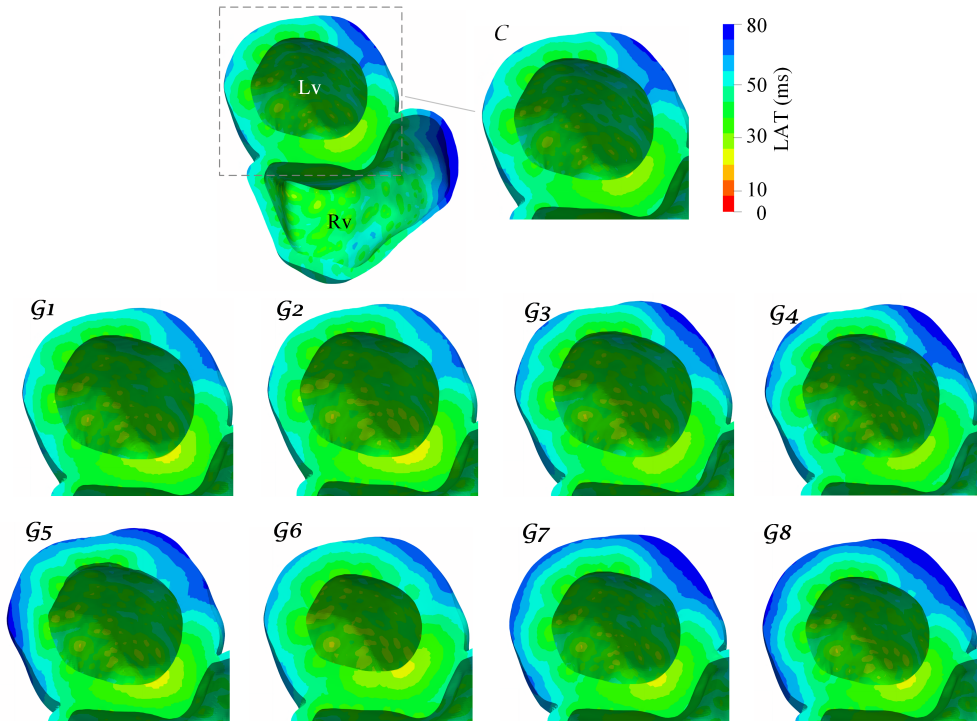


Figure 5.9: AT maps on the LV of each globular model. The control model is displayed at the top.

To visualize the variation in AT between the control model and the globular models, Fig. 5.9 was included, with an emphasis on the ventricular base. The AT maps in all \mathcal{G}_i models, except for \mathcal{G}_4 , indicate that AP propagation to the base of the LV occurs more rapidly compared to the \mathcal{C} model, particularly in the region around the endocardial surface of the LV. The faster propagation is attributed to the reduction of \mathcal{L} in all \mathcal{G}_i models, which, in turn, shortens the AP propagation time. The \mathcal{G}_i models with greater increases in \mathcal{W} show their impact on a longer AT on the outer epicardial surface of the LV. The greatest AT delay is observed in models \mathcal{G}_5 and \mathcal{G}_8 , where VTV is larger compared to the other globular models.

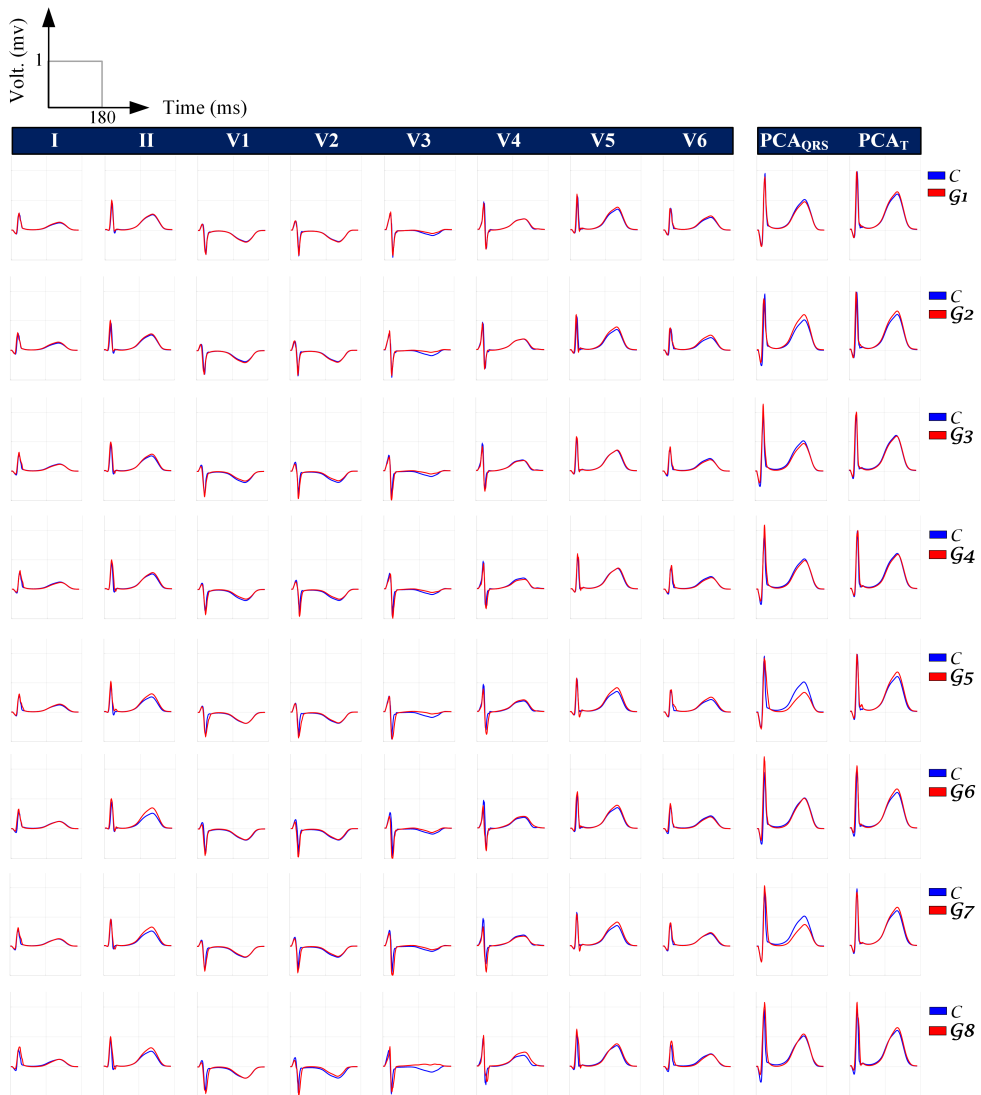


Figure 5.10: Eight independent standard ECG leads, together with PCA_{QRS} and PCA_{T} leads for each \mathcal{G}_i model, overprinted with the ECGs from \mathcal{C} model. The third beat of each simulation was represented.

In Fig. 5.10, the calculated ECGs for each of the 8 virtual leads, along with the PCA_{QRS} and PCA_{T} leads, are shown. In all leads, the globular models show an earlier depolarization phase (earlier red upstroke of QRS complex), although minimal, due to the shortening of SpI . Additionally, both QRS_d and QRS_a (specifically in precordial lead V6 and limb leads I and II) increase due

to the thickening of the free ventricular wall.

Ta tends to increase in the globular models, and in the PCAT measurements, all \mathcal{G}_i models exhibit an amplitude increase, except for \mathcal{G}_3 and \mathcal{G}_4 . Regarding the end of the T-wave, hardly differences are observed between the \mathcal{G}_i models and the control model \mathcal{C} .

5.4 Discussion

Electrophysiological variations associated with IUGR have been identified in different age cohorts [14, 64, 138] and linked to cardiovascular complications [43, 46]. Understanding the impact of reduced left ventricular SpI, increased \mathcal{W} , and VTV on cardiac electrical activity could contribute to a better understanding of IUGR-related cardiac remodeling. This research reports the changes in depolarization and repolarization intervals in control and IUGR subjects. The results from the analysis of clinical data, support that the geometric changes associated with IUGR appeared together with an electrophysiological alteration, which could be hypothesized to be related, at least partially. Additionally, this chapter simulates anatomical cardiac changes due to IUGR using eight different \mathcal{G}_i models, derived from a control \mathcal{C} model, to assess their impact on depolarization and repolarization ECG intervals, using computational models based on a real heart and torso anatomy.

The IUGR cohort presented a significantly prolonged QRS_d compared to the control cohort (Table 5.2). This increase could be associated with a larger VTV, which delays electrical propagation, widening the QRS complex. The significant increase in $T_{pe,c}$ could also be linked to the thickening of the left \mathcal{W} . However, the QT_c interval was found to be no significantly reduced in the IUGR cohort.

Regarding the change in QRS_d , our results align with previous studies [53, 54], where its prolongation and a greater QT dispersion were also observed in [55]. We hypothesize that the increase in \mathcal{W} impacts the intervals, especially T_{pe} . To analyze the influence of geometric remodeling on electrophysiology, *in silico* tests were conducted to better understand this relationship.

5.4.1 Cardiac remodeling in silico

Cardiac remodeling was simulated by deforming the \mathcal{C} model into more globular ones \mathcal{G}_i with $i \in \{1, \dots, 8\}$. Magnitude of changes in ϕ and \mathcal{L} were based on

geometric changes observed in clinical data, with the \mathcal{G}_1 model aiming for a percentage change similar to that reported in Sarvari et al. [13], with subsequent models incrementally increasing these changes to evaluate their electrophysiological impact. Deformations focused on the LV, but geometric effects also affected the RV. \mathcal{L} changes in the LV affected the entire model, leading to an average reduction of 9.4% in right ventricular \mathcal{L} , with a median value of 51.9 mm (range 50.5-53.0 mm). The right ventricular ϕ decreased by 1.2%, to 41.9 mm (range 41.4-42.6 mm), and the right ventricular SpI decreased by 8.15%.

The left ventricular \mathcal{W} increased, primarily at the base, except in \mathcal{G}_8 , where it increased by approximately 40% in both ventricular walls and in \mathcal{G}_6 , increasing the width of the LV inward (see \mathcal{G}_8 and \mathcal{G}_6 in Fig. 5.5). VTV increases, as shown in Table 5.1, mainly as a reflect of the increase in left ventricular wall width. This width increase is significant in IUGR infants [8] and noticeable, though non-significantly, in preadolescents [13].

The Purkinje network applied to the \mathcal{G}_i models was reduced in length in the apex-base direction and widened in the diametrical ϕ direction compared to the \mathcal{C} model. Its effect on a earlier activation is evident when observing the AT on the epicardial periphery of the LV in Fig. 5.10 for all \mathcal{G}_i models. While this reduction in the \mathcal{L} direction brought nodes closer, generating areas with a higher node density, no evidence was found of conduction system changes due to IUGR. This study focused on the geometric changes; hence, the same Purkinje network configuration was used throughout the models.

For the simulated ECG on virtual electrodes, considering the QRS complex, almost all models exhibited increased QRS_d across all leads, also visible in QRS_d measurements on PCA_{QRS} . A slight increase in QRS_a and T_a is also evident. In \mathcal{G}_8 , the model with the highest VTV increase, a significant rise in T_a is observed, mainly in leads V2, V3, and V4 (see Fig. 5.10).

The geometric changes applied to the globular models in this study were introduced homogeneously across the ventricular wall; however, different strategies could have been followed. In this study we had restricted to homogeneous changes since no evidences supporting non-homogeneous changes were found [13].

5.4.2 Impact of left basal diameter ϕ and wall width \mathcal{W} in QRS_d

Previous studies have reported that during the fetal stage, changes in QRS_d exhibit contradictory patterns, as we can see in [51, 52, 58]. However, in our study, with an IUGR and control preadolescent cohort, a significant median

QRS_d increase of 4 ms (p -value=0.039) was observed (see Table 5.2a).

In addition to these findings, we found in simulation that all globally deformed \mathcal{G}_i models showed an increase in QRS_d, in agreement with clinical results and those pointing to QRS_d widening as result of IUGR conditioning. Through multiple regression analysis, it is observed that in QRS_d, a significant contribution of its variance, depends on geometric changes with an $R^2=0.77$ and p -value=0.048. Two of the parameters alone have a p -value<0.05 (ϕ : p -value=0.028 and \mathcal{W} : p -value=0.023), indicating that these variables have a significant impact on the change in QRS_d. These values should be analyzed with caution due to the limited number of simulations (eight cases).

The deformations in wall ventricular thickness \mathcal{W} varied across the models, and revealed a strong relationship between the increase in \mathcal{W} at the base and the rise in QRS_d. For instance, \mathcal{G}_6 produces the smallest change in QRS_d (3 ms) and exhibits an increase in \mathcal{W} toward the interior of the ventricle. In contrast, model \mathcal{G}_5 shows an increase in \mathcal{W} in the opposite direction, with a corresponding QRS_d increase of 17.5 ms.

In middle-aged and older adults, a QRS_d > 100 ms significantly increases heart failure risk [39]. In this study, in both clinical results (QRS_d=87 (81-90) ms) and *in silico* results, QRS_d did not exceed 81.5 ms, even in the extreme case of \mathcal{G}_5 , probably indicating low cardiac risk for its age, but pointing to higher propensity in the IUGR cases. Clinical data showed an increase in QRS complex maximum amplitude in the IUGR cohort, replicated in the models (\mathcal{G}_3 , \mathcal{G}_4 , \mathcal{G}_6 to \mathcal{G}_8) simulations.

The VTV feature as such does not capture well the morphological changes induced by IUGR. Note that only three out of eight cases (\mathcal{G}_5 , \mathcal{G}_7 , and \mathcal{G}_8 , see Table 5.1), result in larger VTV than the control heart \mathcal{C} . When computing the regression of the ECG parameters QRS_d T_{pe} and QT with VTV, no significant correlation in any case was found, implying that the translation of VTV to ECG changes is not straightforward. On the contrary, we observed that morphological features, such as basal enlargement or apex-base length, correlated to the observed changes in ECG characteristics.

5.4.3 T_{pe} and QT intervals

T_{pe}, related to spatial dispersion of ventricular repolarization, is significantly increased with hypertrophy [139]. Clinical results showed a significant heart rate corrected T_{pe}, T_{pe,c}, increase of 2 ms in the IUGR cohort (p -value=0.031) and a non-significant decrease in T-wave amplitude of 0.15 mV. In simulations,

Table 5.2b shows a small T_{pe} increase, with a maximum change of 2 ms. Except for \mathcal{G}_3 and \mathcal{G}_4 , T_{pe} increased in all globular models. The reduction here seems to be related to T-wave peak delay associated with the lower T-wave amplitude (Fig. 5.7b).

The increase in VTV leads to a subtle rise in T_{pe} across all \mathcal{G}_i models, except for \mathcal{G}_3 and \mathcal{G}_4 . However, the extreme increase in VTV in \mathcal{G}_8 does not result in a proportional rise in T_{pe} . In Table 5.3 we see that geometric changes do not have a significant effect on T_{pe} and QT.

The QT interval showed a non-significant reduction of 2 ms in median in clinical data. Despite the QRS_d increase, the T_{end} mark remained nearly constant (Fig. 5.7b). This is significant as the \mathcal{G}_i models underwent various geometric and volumetric changes without much effect on repolarization. The subtle differences in the QT interval indicate that the increase in \mathcal{W} does not significantly affect the repolarization phase. As shown in Fig. 5.8, the APD_{90} in epicardial cells shows that the delay in the depolarization phase does not directly affect the T_{end} point. In the same epi cells, it is observed that the wider the \mathcal{W} in the LV, the shorter the APD_{90} . Additionally, it can be seen that the endo cells determine the duration of QRS_d . While endo cells activate earlier, they are the last to repolarize (Fig. 5.8b), which explains why QT does not show changes as remarkable as those observed in QRS_d .

Several methodologies exist for detecting and delineating ECG waves, potentially leading to different ECG interval values. However, to ensure a meaningful comparative analysis of results across different models and between real and simulated data, it is essential to use the same algorithms, as has been done in this study, along with a reliable and widely used methodology [89].

The reduction of the midmyocardial section directly affected the T-wave, leading to a decrease in both the T_{pe} and QT intervals (see Table 5.4). However, this effect occurs alongside changes induced by SpI and \mathcal{W} , which moderate the overall variation in these intervals. As expected, modifications in transmural composition did not influence QRS_d , aligning with previous findings. Additionally, it is important to acknowledge the ongoing debate regarding the presence of M-cells with prolonged repolarization in human hearts [108, 140]. Interestingly, when the midmyocardial layer is reduced, the differences in QT and T_{pe} intervals between the control and globular models become smaller, showing better agreement with the clinical results in Table 5.2. The fact that the differences between control and globular model in T_{pe} and QT when midmyocardium is reduced (Table 5.4) are smaller, and in better accordance with the clinical results in Table 5.2 could suggest the possibility of questioning their

existence.

A comparison of ECG wave intervals between the simulated models and clinical data reveals interesting differences in the order of magnitude, as shown in Table 5.2. While the simulated QRS_d and T_{pe} parameters align well within clinical ranges, the QT interval exhibits a slightly higher deviation. This discrepancy may stem from differences in the RR interval or ionic properties between the control \mathcal{C} model design [97] and the average subject geometry in the dataset. However, since the primary analysis focuses on the relative changes between the globular and control models, this difference is not expected to significantly impact the comparative assessment.

All simulations were performed with $RR=1000$ ms. This allows comparisons with repolarization intervals in ECGs recorded at different heart rates by considering heart rate corrected intervals, as presented in Table 5.2. Running simulations at different RR interval values could allow for more personalized heart rate analyses by selecting ECG data from patients with matching RR intervals. However, this would require a significantly larger dataset, which is beyond the scope of the current study.

The results suggest that the considered cardiac remodeling primarily affects the depolarization cycle, notably QRS_d . The incorporated globular model changes only consider geometric variations. It can be speculated if other remodeling, as conduction abnormalities or electrophysiological modifications, can add to better reproduce the ECG clinical observations. This can be the subject of future studies.

The main finding of this chapter underscores the effect of anatomical remodeling in IUGR-born subjects on the ECG, specifically prolonging the QRS_d without influencing the QT interval. The computational framework offers insights into the underlying mechanisms, identifying ventricular wall thickening at the base as the primary factor driving these effects, without any ionic remodeling involved. It also represents a potentially useful clinical tool to monitor cardiac risk derived from the IUGR condition.

5.5 Limitations

Beyond its findings, this study has some limitations that should be addressed. First, the number of subjects in both the control and IUGR groups is limited. While significant differences were identified in QRS_d and T_{pe} , the findings should be interpreted with caution. However, the results provide a foundation for future research involving a larger cohort, which could further validate and

refine the observed associations. Despite the sample size constraint, significant differences were identified in QRS_d and T_{pe} , with their variability ranges indicating considerable distinctions in both biomarkers.

From a computational simulation perspective, this study has developed a simulation framework designed to achieve a realistic scenario, specifically analyzing the effects of geometric changes resulting from IUGR while maintaining other parameters, such as the conduction system and propagation velocity, as constants. To achieve this, eight globular models were developed based on clinically observed geometric changes, incorporating additional modifications to evaluate their impact on cardiac electrophysiology. While various alternative approaches could be explored for constructing globular models, the ones used in this study encompass a meaningful range of variations in ϕ , \mathcal{L} , \mathcal{W} , and VTV. The findings highlight a strong relationship between changes in \mathcal{W} and their impact on QRS_d . Nevertheless, further investigation is necessary, considering parameters beyond those addressed in this study.

The selection of eight models represents a balance between comprehensive evaluation and capturing the range of plausible anatomical dynamics. While a more extensive set of models with gradual variations could provide deeper insights, this study offers valuable learning that can guide future work. Further refinements, including additional remodeling, may help address phenomena not fully observed or replicated in this study.

5.6 Conclusion

This chapter has shown a direct relationship between anatomical cardiac remodeling and ECG changes which are compared with a cohort of preadolescents born with IUGR. In the clinical results, a significant increase in QRS_d and a slight increase in $T_{pe,c}$ were observed in ECG data when compared to the control cohort. However, no significant differences were found in the QT interval.

In silico simulation results reveal that anatomical changes induced by IUGR, particularly in apex-base length \mathcal{L} , basal diameter ϕ , and ventricular wall thickness \mathcal{W} , significantly impact electrocardiographic parameters. The observed increases in QRS_d and T_{pe} align with clinical data, reinforcing a direct connection between geometrical deformations and ECG modifications. However, while the simulated QT interval shows a 1% increase, clinical observations show no change in the QT interval. This discrepancy may be attributed to cellular coupling within the computational mesh, affecting AP propagation during

the T-wave, as evidenced by the pilot test generating a model with different transmural cellular distribution.

The variation in QRS_d in IUGR patients highlights a direct relationship with increased ventricular wall thickness \mathcal{W} , particularly at the basal region. In contrast, changes in T_{pe} and the QT interval, which are more strongly linked to transmural heterogeneities, highlight the need for further research to investigate additional electrophysiological mechanisms beyond the geometrical factors explored in this study.

CHAPTER 6

CONCLUSIONS AND FUTURE WORK

6.1 Main findings

6.1.1 Angular variation of depolarization and repolarization loops *in silico*

6.1.2 ECG interval biomarkers in clinical studies

6.1.3 Biomarkers in the synthetic ECG

6.2 General conclusions

6.3 Perspectives for future work

This PhD thesis has investigated the electrophysiological effects resulting from geometric changes induced by IUGR. Using globular computational models derived from measurements in a cohort of preadolescents born with IUGR, key structural parameters including apex-to-base length, basal diameter ϕ , and ventricular wall thickness \mathcal{W} , were analyzed with a primary focus on the left ventricle.

Additionally, cardiovascular risk-associated biomarkers (QRS_d , T_{pe} , and QT) were assessed within the same cohort. To further explore the mechanisms behind these relationships, *in silico* simulations were conducted to evaluate the impact of reduced sphericity index SpI and ventricular wall thickness \mathcal{W} on the studied biomarkers. The results provide new insights into the potential mechanisms linking altered cardiac geometry to electrophysiological risks in individuals affected by IUGR.

This final chapter synthesizes the analysis of the results obtained throughout this PhD thesis and presents key perspectives for future research directions.

6.1 Main findings

The central hypothesis of this thesis posits that anatomical cardiac remodeling as a consequence of IUGR plays a significant role in the electrophysiological changes associated with increased cardiovascular risk. While various effects of IUGR have been observed in newborns, some of these alterations diminish over time, whereas others persist into later stages of life, including preadolescence and adulthood. The impact of IUGR or other adverse conditions during the fetal stage has been proposed as significant factors contributing to a higher risk of cardiovascular problems in adulthood. However, the precise relationship between geometric remodeling and cardiac electrophysiology remains unclear. For the first time, this thesis systematically evaluates the electrophysiological effects of changes in SpI and \mathcal{W} using *in silico* models. These analyses investigated the direction of the dominant vector during depolarization and repolarization loops, as well as key ECG biomarkers associated with cardiovascular risk.

6.1.1 Angular variation of depolarization and repolarization loops in *in silico*

To assess the impact of geometric alterations induced by IUGR on the depolarization and repolarization loops, these were computed using a control *in silico* model and eight deformed globular models. Analysis of the dominant vector directions in the globular models revealed significant changes compared to the control model, partially attributed to alterations in the SpI. To rule out the influence of heart displacement within the torso on these electrophysiological variations, additional simulations incorporating this factor were performed. While positional changes led to some electrical alterations, their magnitude was significantly smaller, confirming that the observed variations primarily result from geometric remodeling rather than positional effects.

The direction of the dominant vectors in the globular models exhibited changes across all spatial planes. Among these, the observed reduction in parameters θ_{RT-XY} and $\theta_{R-XZ} - \theta_{T-XZ}$ is consistent with reported clinical trends in preadolescents and adults, emphasizing their relevance as biomarkers for quantifying sphericity reduction. These findings are particularly significant

as they provide a quantifiable link between electrophysiological changes and structural alterations in cardiac geometry. Furthermore, the relative measures derived from the depolarization-repolarization relationship demonstrated lower sensitivity to heart-to-electrode positioning, enhancing their robustness and reliability across different clinical scenarios and patient conditions. Such stability is crucial for their potential integration into routine diagnostics, making them more robust and suitable for clinical use.

The discrepancies observed in the absolute angles between depolarization and repolarization loops in computational simulations, compared to clinical data from adults and/or preadolescents, highlight a critical gap in our understanding of cardiac electrophysiological remodeling across different age groups. This misalignment may stem from the transient nature of remodeling during preadolescence, which could attenuate or evolve in adulthood, thereby complicating direct comparisons.

6.1.2 ECG interval biomarkers in clinical studies

Differences in the duration of ECG biomarkers associated with cardiovascular risk (QRS_d , T_{pe} , and QT) have been widely reported in the literature, particularly in newborns, although the results have often been inconsistent. Whether the effects of IUGR persist into adulthood remains an open research question requiring further investigation. In this study, we analyzed these biomarkers in a cohort of preadolescents diagnosed with IUGR at birth. The measurement of biomarker durations across the 12 standard ECG leads revealed significant differences. Specifically, QRS_d showed notable changes in lead II, while T_{pe} and the T_{pe}/QT ratio presented significant alterations in lead V4.

To synthesize the primary information across the 12 leads and provide a more objective delineation, principal component analysis was applied, resulting in the generation of two new derived leads: PCA_{QRS} and PCA_T . These derived leads facilitated a more comprehensive and systematic evaluation of the biomarkers, improving the interpretation and reliability of the findings in this cohort.

The biomarker measurements performed on the newly derived leads, has shown a direct relationship between anatomical cardiac remodeling and ECG changes in the cohort of preadolescents who born with IUGR. The analysis revealed a significant increase in QRS_d and a slight but notable increase in $T_{pe,c}$ were observed in ECG data when compared to the control cohort. Interestingly, no significant differences were found in the QT interval, indicating that while some aspects of repolarization dynamics are affected, the overall repolarization

duration remains relatively preserved. These findings underscore the impact of IUGR on cardiac electrophysiology, providing important insights into the significance of QRS_d and T_{pe} as biomarkers for detecting and monitoring cardiac remodeling.

6.1.3 Biomarkers in the synthetic ECG

The observed increase in the duration of QRS_d and T_{pe} biomarkers in the cohort of preadolescents diagnosed with IUGR at birth suggested a hypothesis: in addition to the reduction in the SpI, the increase in \mathcal{W} might significantly influence these biomarkers. To explore the impact of these geometric changes on the biomarkers, this study modeled cardiac remodeling by incorporating variations in the SpI and \mathcal{W} . The effects of these geometric alterations on electrophysiology were reflected in the observed changes in the duration of depolarization and repolarization biomarkers. These findings reinforce the idea that structural remodeling plays a critical role in modifying cardiac electrophysiological characteristics, providing valuable insights into the mechanisms linking anatomical and functional changes in IUGR cases.

In silico simulation results reveal that anatomical changes induced by IUGR, particularly alterations in apex-base length \mathcal{L} , basal diameter ϕ , and ventricular wall thickness \mathcal{W} , have a significant effect on ECG biomarkers. These geometrical alterations are associated with observed increases in QRS_d and T_{pe} , findings that align closely with clinical data and further support a direct connection between geometrical deformations and ECG modifications. However, while the simulated QT interval shows an increase, clinical observations report no change in this parameter.

The variation in QRS_d observed in IUGR models highlights a direct relationship with increased \mathcal{W} , particularly at the basal region, suggesting that structural remodeling significantly impacts the depolarization phase of the cardiac cycle. In contrast, changes in T_{pe} and the QT interval are more strongly linked to transmural heterogeneities, highlighting the complexity of repolarization dynamics. These observations suggest that geometrical factors such as \mathcal{W} and SpI play a critical role, particularly in explaining the variations observed in depolarization parameters.

6.2 General conclusions

Cardiac remodeling induced by IUGR has been recognized as a significant factor in electrophysiological alterations associated with increased cardiovascular risk. Clinical studies have shown that this remodeling, evident in newborns, can have long-term consequences, with persistent manifestations in preadolescence and potentially into adulthood. However, the specific relationship between geometric cardiac alterations and electrophysiological changes remains poorly understood. In this research, for the first time, the effects of anatomical remodeling on electrophysiological parameters were evaluated through *in silico* simulations. Changes in the SpI and their influence on the direction of depolarization and repolarization loops were analyzed. Globular models demonstrated significant variations in the dominant vectors of these phases, largely attributed to changes in cardiac geometry. Additionally, simulations considering heart displacement within the torso ruled out this factor as the primary cause of the observed electrophysiological alterations.

ECG data from preadolescents diagnosed with IUGR at birth were analyzed using both standard leads and newly derived leads generated through PCA. This approach identified a significant increase in QRS_d and a slight but noticeable increase in $T_{pe,c}$ compared to the control cohort, while no significant differences were observed in the QT interval. These findings highlight the relevance of QRS_d and T_{pe} as biomarkers of cardiac remodeling.

The *in silico* results confirmed that geometric alterations induced by IUGR, such as reduced SpI and increased \mathcal{W} , significantly impact the studied ECG biomarkers. In particular, a direct relationship was observed between increased QRS_d and basal \mathcal{W} , while changes in T_{pe} and QT interval were more closely associated with transmural heterogeneities. However, the simulations showed an increase in the QT interval that did not align with clinical observations, suggesting the need to investigate other mechanisms, such as cellular heterogeneity or cellular coupling within the models.

This research establishes a connection between anatomical remodeling induced by IUGR and electrophysiological changes observed in the ECG. We have shown how geometric factors like the SpI and \mathcal{W} play a critical role, especially in explaining alterations in depolarization parameters. These findings underscore the complexity of the mechanisms involved and the need for further exploration through both computational and clinical approaches to advance the understanding of the impact of IUGR on cardiovascular health and risk.

6.3 Perspectives for future work

The analysis of the results obtained in this study, the methodology employed, and the review of the state of the art have allowed us to establish several future research directions within this line of investigation.

Effects of heart position in the torso on computational simulations

The variation in the direction of the dominant vectors of depolarization and repolarization loops was evaluated and compared with the impact of displacing the heart model within the torso. It was observed that the effect of displacement was significantly smaller than the impact of geometric remodeling. In this context, it may be valuable to assess the effect of rotating the heart model within the torso on the direction of the dominant vectors.

The simulation results were consistent with clinical data for certain measurements and specific planes (θ_{RT-XY} and $\theta_{R-XZ} - \theta_{T-XZ}$). However, differences in trends for angular measurements, where no similarity was found, could be attributed to the rotation of the model. Although no evidence in the current literature supports heart rotation as a consequence of IUGR, this alteration could partially explain the observed angular changes. This hypothesis emerged after observing that using different ECG-to-VCG transformation matrices introduced subtle variations in angular results. This is due to differences in the coefficients within the transformation matrices, such as the Kors and Dower matrices, and the specific leads contributing to the VCG. A potential extension of this thesis could involve further investigation into the sensitivity of angular measurements to variations in cardiac orientations. Specifically, a degree of uncertainty may arise from realistic and plausible heart positions, and future work could explore how heart model rotation influences changes in the direction of the dominant vectors. This would provide a deeper understanding of the impact of cardiac orientation on electrophysiological measurements.

Impact of IUGR on the Purkinje conduction system

In our study, we analyzed the impact of geometric variations on cardiac electrophysiology while maintaining a consistent Purkinje conduction system network in the computational models. The network was only adapted to changes in the endocardial surface of the globular models. However, modifications of the conduction system and its propagation direction could potentially occur as a result of cardiac remodeling in IUGR. The presence and effect of these changes, however, remain unclear and warrant further investigation.

Clinical analysis of ECG biomarkers identified in IUGR

This study identified several biomarkers with high potential as indicators of cardiac remodeling in ECG and VCG. Evaluating these parameters in a clinical setting could demonstrate their utility in identifying cardiac alterations not only due to IUGR but also in other scenarios involving anatomical remodeling. Assessing these biomarkers in a larger cohort would allow for improved adjustment of depolarization and repolarization interval corrections while determining whether remodeling effects are significant. Furthermore, a longitudinal study could reveal whether the electrophysiological changes observed in preadolescence persist into adulthood, as suggested by previous research.

***In silico* modeling of realistic heart models**

The computational cost and simulation time for solving the reaction-diffusion system using FEM have been significantly reduced. This improvement will enable a greater number of simulations to be conducted in shorter time frames, allowing for a more comprehensive exploration of various cardiac remodeling scenarios and their effects on electrophysiology.

These perspectives provide a road map for expanding this line of research, leveraging advanced modeling techniques and clinical data to enhance our understanding of the relationship between cardiac geometry and electrophysiology in IUGR and other conditions.

BIBLIOGRAPHY

- [1] A. Timmis, V. Aboyans, P. Vardas, N. Townsend, A. Torbica, M. Kavousi, G. Boriani, R. Huculeci, D. Kazakiewicz, D. Scherr, *et al.*, “European society of cardiology: the 2023 atlas of cardiovascular disease statistics,” *European Heart Journal*, vol. 45, no. 38, pp. 4019–4062, 2024.
- [2] O. P. de la Salud, “La carga de las enfermedades cardiovasculares en la región de las américas, 2000-2019,” 2021.
- [3] M. De Onis, M. Blössner, and J. Villar, “Levels and patterns of intrauterine growth retardation in developing countries.,” *European Journal of Clinical Nutrition*, vol. 52, pp. S5–15, 1998.
- [4] A. Lucas, “Long-term programming effects of early nutrition—implications for the preterm infant,” *Journal of Perinatology*, vol. 25, no. 2, pp. S2–S6, 2005.
- [5] L. Belkacemi, D. M. Nelson, M. Desai, and M. G. Ross, “Maternal undernutrition influences placental-fetal development,” *Biology of Reproduction*, vol. 83, no. 3, pp. 325–331, 2010.
- [6] A. Romo, R. Carceller, and J. Tobajas, “Intrauterine growth retardation (iugr): epidemiology and etiology.,” *Pediatric Endocrinology Reviews: PER*, vol. 6, pp. 332–336, 2009.
- [7] J. E. Uceda, L. Caravedo-Reyes, and M. L. Figueroa, “Malnutrición materno-fetal: Revisión de la bibliografía internacional y la urgencia de

- estudios, prevención e intervención en el Perú,” *Revista Medica Hereditana*, vol. 32, no. 1, pp. 52–58, 2021.
- [8] M. Cruz-Lemini, F. Crispi, B. Valenzuela-Alcaraz, F. Figueras, M. Sitges, B. Bijmens, and E. Gratacós, “Fetal cardiovascular remodeling persists at 6 months in infants with intrauterine growth restriction,” *Ultrasound in Obstetrics & Gynecology*, vol. 48, no. 3, pp. 349–356, 2016.
- [9] N. Amruta, H. K. Kandikattu, and S. Intapad, “Cardiovascular dysfunction in intrauterine growth restriction,” *Current Hypertension Reports*, vol. 24, no. 12, pp. 693–708, 2022.
- [10] H. Altın, S. Karaarslan, Z. Karataş, H. Alp, F. Şap, and T. Baysal, “Evaluation of cardiac functions in term small for gestational age newborns with mild growth retardation: a serial conventional and tissue doppler imaging echocardiographic study,” *Early Human Development*, vol. 88, no. 9, pp. 757–764, 2012.
- [11] D. J. Cox, W. Bai, A. N. Price, A. D. Edwards, D. Rueckert, and A. M. Groves, “Ventricular remodeling in preterm infants: computational cardiac magnetic resonance atlas shows significant early remodeling of the left ventricle,” *Pediatric Research* 2019 85:6, vol. 85, pp. 807–815, 11 2018.
- [12] M. R. Skilton, N. Evans, K. A. Griffiths, J. A. Harmer, and D. S. Celermajer, “Aortic wall thickness in newborns with intrauterine growth restriction,” *The Lancet*, vol. 365, pp. 1484–1486, 4 2005.
- [13] S. Imre Sarvari, M. Rodríguez López, M. Nuñez-García, M. Sitges, Á. Sepúlveda-Martínez, O. Camara, C. Butakoff, E. Gratacós Solsona, B. Bijmens, and F. Crispi Brillas, “Persistence of cardiac remodeling in preadolescents with fetal growth restriction,” *Circulation: Cardiovascular Imaging*. 2017 Jan; 10 (1): 1-9., 2017.
- [14] N. Ortigosa, M. Rodríguez-Lopez, R. Bailón, S. I. Sarvari, M. Sitges, E. Gratacos, B. Bijmens, F. Crispi, and P. Laguna, “Heart morphology differences induced by intrauterine growth restriction and preterm birth measured on the ecg at preadolescent age,” *Journal of Electrocardiology*, vol. 49, no. 3, pp. 401–409, 2016.
- [15] N. Ortigosa, M. Rodríguez-Lopez, R. Bailon, A. Sepulveda-Martinez, E. Gratacos, F. Crispi, and P. Laguna, “Intrauterine growth restriction

- induced eeg morphological differences measured in adulthood,” *Computing in Cardiology*, vol. 2018-Septe, pp. 3–6, 2018.
- [16] N. B. Ojeda, D. Grigore, and B. T. Alexander, “Intrauterine growth restriction: Fetal programming of hypertension and kidney disease,” *Advances in Chronic Kidney Disease*, vol. 15, pp. 101–106, 2008.
- [17] D. J. Barker, “Intrauterine programming of adult disease,” *Molecular Medicine Today*, vol. 1, no. 9, pp. 418–423, 1995.
- [18] M. D. Hughson, R. Douglas-Denton, J. F. Bertram, and W. E. Hoy, “Hypertension, glomerular number, and birth weight in african americans and white subjects in the southeastern united states,” *Kidney International*, vol. 69, no. 4, pp. 671–678, 2006.
- [19] G. J. Tortora and B. H. Derrickson, *Principles of anatomy and physiology*. John wiley & sons, 2018.
- [20] P. Stewart, O. V. Aslanidi, D. Noble, P. J. Noble, M. R. Boyett, and H. Zhang, “Mathematical models of the electrical action potential of purkinje fibre cells,” *Philosophical Transactions of the Royal Society A: Mathematical, Physical and Engineering Sciences*, vol. 367, pp. 2225–2255, 2009.
- [21] D. D. Streeter Jr, H. M. Spotnitz, D. P. Patel, J. Ross Jr, and E. H. Sonnenblick, “Fiber orientation in the canine left ventricle during diastole and systole,” *Circulation Research*, vol. 24, no. 3, pp. 339–347, 1969.
- [22] R. Plonsey and R. C. Barr, *Bioelectricity: A Quantitative Approach*. New York, NY: Springer, 3rd ed., 2007.
- [23] L. Sörnmo and P. Laguna, *Bioelectrical signal processing in cardiac and neurological applications*. Academic press, 2005.
- [24] J. D. Bronzino, *Biomedical engineering handbook 2*, vol. 2. Springer Science & Business Media, 2000.
- [25] T. O’Hara, L. Virág, A. Varró, and Y. Rudy, “Simulation of the undiseased human cardiac ventricular action potential: Model formulation and experimental validation,” *PLoS Computational Biology*, vol. 7, may 2011.
- [26] C. Antzelevitch, W. Shimizu, G.-X. YAN, S. Sicouri, J. Weissenburger, V. V. Nesterenko, A. Burashnikov, J. di Diego, J. SAFFITZ, and G. P.

- Thomas, "The m cell: its contribution to the eeg and to normal and abnormal electrical function of the heart," *Journal of Cardiovascular Electrophysiology*, vol. 10, no. 8, pp. 1124–1152, 1999.
- [27] C. Antzelevitch, "M cells in the human heart," *Circulation Research*, vol. 106, no. 5, pp. 815–817, 2010.
- [28] R. Coronel, F. J. Wilms-Schopman, T. Opthof, and M. J. Janse, "Dispersion of repolarization and arrhythmogenesis," *Heart Rhythm*, vol. 6, no. 4, pp. 537–543, 2009.
- [29] C. Antzelevitch and J. Fish, "Electrical heterogeneity within the ventricular wall," *Basic Research in Cardiology*, vol. 96, pp. 517–527, 2001.
- [30] H. Yang, S. T. Bukkapatnam, and R. Komanduri, "Spatiotemporal representation of cardiac vectorcardiogram (vkg) signals," *Biomedical Engineering Online*, vol. 11, pp. 1–15, 2012.
- [31] A. R. Pérez-Riera and R. Barbosa-Barros, "The value of the vectorcardiogram in brugada syndrome," in *Brugada Phenocopy*, pp. 99–112, Elsevier, 2018.
- [32] A. R. Pérez-Riera, R. Barbosa-Barros, R. Daminello-Raimundo, L. C. de Abreu, J. E. T. Mendes, and K. Nikus, "Left posterior fascicular block, state-of-the-art review: A 2018 update," *Indian Pacing and Electrophysiology Journal*, vol. 18, no. 6, pp. 217–230, 2018.
- [33] C. A. Pastore, N. Samesima, H. G. Pereira Filho, N. M. M. d. O. Tobias, B. A. Madaloso, and M. E. Facin, "Applicability of the electrovectorcardiogram in current clinical practice," *Arquivos Brasileiros de Cardiologia*, vol. 113, no. 1, pp. 87–99, 2019.
- [34] E. Frank, "An accurate, clinically practical system for spatial vectorcardiography," *Circulation*, vol. 13, no. 5, pp. 737–749, 1956.
- [35] Y.-H. Chuang, C.-L. Huang, W.-W. Chang, and J.-T. Chien, "Automatic classification of myocardial infarction using spline representation of single-lead derived vectorcardiography," *Sensors*, vol. 20, no. 24, p. 7246, 2020.
- [36] J. Kors, G. Van Herpen, A. Sittig, and J. Van Bommel, "Reconstruction of the frank vectorcardiogram from standard electrocardiographic leads: diagnostic comparison of different methods," *European Heart Journal*, vol. 11, no. 12, pp. 1083–1092, 1990.

- [37] R. Jaros, R. Martinek, and L. Danys, "Comparison of different electrocardiography with vectorcardiography transformations," *Sensors (Switzerland)*, vol. 19, pp. 1–19, 2019.
- [38] L. Edenbrandt and O. Pahlm, "Vectorcardiogram synthesized from a la-lead ecg: Superiority of the inverse dower matrix," *Journal of Electrocardiology*, vol. 21, pp. 361–367, 1988.
- [39] L. Ilkhanoff, K. Liu, H. Ning, S. Nazarian, D. A. Bluemke, E. Z. Soliman, and D. M. Lloyd-Jones, "Association of qrs duration with left ventricular structure and function and risk of heart failure in middle-aged and older adults: The multi-ethnic study of atherosclerosis (mesa)," *European Journal of Heart Failure*, vol. 14, pp. 1285–1292, 11 2012.
- [40] S. Aeschbacher, W. T. O'Neal, P. Krisai, L. Loehr, L. Y. Chen, A. Alonso, E. Z. Soliman, and D. Conen, "Relationship between qrs duration and incident atrial fibrillation," *International Journal of Cardiology*, vol. 266, pp. 84–88, 9 2018.
- [41] M. Yamaguchi, M. Shimizu, H. Ino, H. Terai, K. Uchiyama, O. Kotaro, T. Mabuchi, T. Konno, T. Kaneda, and H. Mabuchi, "T wave peak-to-end interval and qt dispersion in acquired long qt syndrome: A new index for arrhythmogenicity," *Clinical Science*, vol. 105, pp. 671–676, 2003.
- [42] P. Gupta, C. Patel, H. Patel, S. Narayanaswamy, B. Malhotra, J. T. Green, and G. X. Yan, "Tp-e/qt ratio as an index of arrhythmogenesis," *Journal of Electrocardiology*, vol. 41, pp. 567–574, 2008.
- [43] L. Schirone, M. Forte, S. Palmerio, D. Yee, C. Nocella, F. Angelini, F. Pagano, S. Schiavon, A. Bordin, A. Carrizzo, C. Vecchione, V. Valenti, I. Chimenti, E. D. Falco, S. Sciarretta, and G. Frati, "A review of the molecular mechanisms underlying the development and progression of cardiac remodeling," *Oxidative Medicine and Cellular Longevity*, vol. 2017, 2017.
- [44] F. Crispi, F. Crovetto, and E. Gratacos, "Intrauterine growth restriction and later cardiovascular function," *Early Human Development*, vol. 126, pp. 23–27, 2018.
- [45] D. Sharma, S. Shastri, and P. Sharma, "Intrauterine growth restriction: Antenatal and postnatal aspects," *Clinical Medicine Insights: Pediatrics*, vol. 10, p. CMPed.S40070, 2016.

- [46] S. Visentin, F. Grumolato, G. B. Nardelli, B. D. Camillo, E. Grisan, and E. Cosmi, “Early origins of adult disease: Low birth weight and vascular remodeling,” *Atherosclerosis*, vol. 237, pp. 391–399, 2014.
- [47] P. M. Nilsson, P.-O. Östergren, P. Nyberg, M. Söderström, and P. Allebeck, “Low birth weight is associated with elevated systolic blood pressure in adolescence: a prospective study of a birth cohort of 149 378 swedish boys,” *Journal of Hypertension*, vol. 15, no. 12, pp. 1627–1631, 1997.
- [48] C. Arnott, M. R. Skilton, S. Ruohonen, M. Juonala, J. S. Viikari, M. Kähönen, T. Lehtimäki, T. Laitinen, D. S. Celermajer, and O. T. Raitakari, “Subtle increases in heart size persist into adulthood in growth restricted babies: the cardiovascular risk in young finns study,” *Open Heart*, vol. 2, no. 1, p. e000265, 2015.
- [49] C. P. Leeson, M. Kattenhorn, R. Morley, A. Lucas, and J. E. Deanfield, “Impact of low birth weight and cardiovascular risk factors on endothelial function in early adult life,” *Circulation*, vol. 103, pp. 1264–1268, 3 2001.
- [50] J. Leger, C. Limoni, D. Collin, and P. Czernichow, “Prediction factors in the determination of final height in subjects born small for gestational age,” *Pediatric Research*, vol. 43, no. 6, pp. 808–812, 1998.
- [51] B. Brambati and L. Bonsignore, “Intraventricular conduction time in fetuses born with growth retardation,” *British Journal of Obstetrics and Gynaecology*, vol. 89, pp. 900–903, 1982.
- [52] G. Pardi and A. Marconi, “The intraventricular conduction time of fetal heart in pregnancies with suspected fetal growth retardation,” *British Journal of Obstetrics and Gynaecology*, vol. 93, pp. 250–254, 1986.
- [53] B. Grimm, C. Kaehler, E. Schleussner, U. Schneider, J. Haueisen, and H. J. Seewald, “Influence of intrauterine growth restriction on cardiac time intervals evaluated by fetal magnetocardiography,” *Early Human Development*, vol. 74, pp. 1–11, 2003.
- [54] P. Van Leeuwen, S. Lange, J. Hackmann, A. Klein, W. Hatzmann, and D. Grönemeyer, “Assessment of intra-uterine growth retardation by fetal magnetocardiography,” in *Biomag Proc 12th Int Conf on Biomagnetism: 13–17 August 2000; Helsinki*, pp. 603–606, 2001.
- [55] C. L. Velayo, K. Funamoto, J. Silao, Y. Kimura, and K. Nicolaides, “Evaluation of abdominal fetal electrocardiography in early intrauterine

- growth restriction,” *Evaluation of Abdominal Fetal Electrocardiography in Early Intrauterine Growth Restriction. Front. Physiol*, vol. 8, p. 437, 2017.
- [56] S. Fouzas, A. A. Karatza, P. A. Davlouros, D. Chrysis, D. Alexopoulos, S. Mantagos, and G. Dimitriou, “Heterogeneity of ventricular repolarization in newborns with intrauterine growth restriction,” *Early Human Development*, vol. 90, pp. 857–862, 12 2014.
- [57] T. Emori and C. Antzelevitch, “Cellular basis for complex t waves and arrhythmic activity following combined ikr and iks block,” *Journal of Cardiovascular Electrophysiology*, vol. 12, pp. 1369–1378, 2001.
- [58] V. Smith, A. Nair, R. Warty, J. A. Sursas, F. da Silva Costa, and E. M. Wallace, “A systematic review on the utility of non-invasive electrophysiological assessment in evaluating for intra uterine growth restriction,” *BMC Pregnancy and Childbirth*, vol. 19, pp. 1–14, 2019.
- [59] F. Crispi, Á. Sepúlveda-Martínez, F. Crovetto, O. Gómez, B. Bijmens, and E. Gratacós, “Main patterns of fetal cardiac remodeling,” *Fetal Diagnosis and Therapy*, vol. 47, no. 5, pp. 337–344, 2020.
- [60] G. C. Zaharie, M. Hasmasanu, L. Blaga, M. Matyas, D. Muresan, and S. D. Bolboaca, “Cardiac left heart morphology and function in newborns with intrauterine growth restriction: relevance for long-term assessment,” *Medical Ultrasonography*, vol. 21, no. 1, pp. 62–68, 2019.
- [61] M. Vijayakumar, C. Fall, C. Osmond, and D. Barker, “Birth weight, weight at one year, and left ventricular mass in adult life.,” *Heart*, vol. 73, no. 4, pp. 363–367, 1995.
- [62] N. Bjarnegård, E. Morsing, M. Cinthio, T. Länne, and J. Brodzki, “Cardiovascular function in adulthood following intrauterine growth restriction with abnormal fetal blood flow,” *Ultrasound in Obstetrics & Gynecology*, vol. 41, no. 2, pp. 177–184, 2013.
- [63] F. L. Bueno-Palomeque, K. A. Mountris, A. Mincholé, N. Ortigosa, R. Bailón, E. Pueyo, and P. Laguna, “Changes in qrs and t-wave loops subsequent to an increase in left ventricle globularity as in intrauterine growth restriction: a simulation study,” in *2020 Computing in Cardiology*, pp. 1–4, IEEE, 2020.

- [64] F. L. Bueno-Palomeque, K. A. Mountris, N. Ortigosa, R. Bailón, B. Binjens, F. Crispi, E. Pueyo, A. Mincholé, and P. Laguna, “Qrs-t angles as markers for heart sphericity in subjects with intrauterine growth restriction: a simulation study,” *IEEE Journal of Biomedical and Health Informatics*, 2023.
- [65] D. Noble, “Modelling the heart: insights, failures and progress,” *Bioessays*, vol. 24, no. 12, pp. 1155–1163, 2002.
- [66] A. L. Hodgkin and A. F. Huxley, “A quantitative description of membrane current and its application to conduction and excitation in nerve,” *The Journal of Physiology*, vol. 117, no. 4, p. 500, 1952.
- [67] K. H. Ten Tusscher and A. V. Panfilov, “Alternans and spiral breakup in a human ventricular tissue model,” *American Journal of Physiology-Heart and Circulatory Physiology*, vol. 291, no. 3, pp. H1088–H1100, 2006.
- [68] J. W. Moore and F. Ramon, “On numerical integration of the hodgkin and huxley equations for a membrane action potential,” *Journal of Theoretical Biology*, vol. 45, no. 1, pp. 249–273, 1974.
- [69] E. Grandi, F. S. Pasqualini, J. L. Puglisi, and D. M. Bers, “A novel computational model of the human ventricular action potential and ca transient,” *Biophysical Journal*, vol. 96, no. 3, pp. 664a–665a, 2009.
- [70] J. Tomek, A. Bueno-Orovio, E. Passini, X. Zhou, A. Mincholé, O. Britton, C. Bartolucci, S. Severi, A. Shrier, L. Virag, *et al.*, “Development, calibration, and validation of a novel human ventricular myocyte model in health, disease, and drug block,” *Elife*, vol. 8, p. e48890, 2019.
- [71] C. Bartolucci, E. Passini, J. Hyttinen, M. Paci, and S. Severi, “Simulation of the effects of extracellular calcium changes leads to a novel computational model of human ventricular action potential with a revised calcium handling,” *Frontiers in Physiology*, vol. 11, p. 314, 2020.
- [72] N. Trayanova, “Defibrillation of the heart: insights into mechanisms from modelling studies,” *Experimental Physiology*, vol. 91, no. 2, pp. 323–337, 2006.
- [73] J. Keener and J. Sneyd, *Mathematical physiology: II: Systems physiology*. Springer, 2009.

- [74] M. Potse, B. Dubé, J. Richer, A. Vinet, and R. M. Gulrajani, “A comparison of monodomain and bidomain reaction-diffusion models for action potential propagation in the human heart,” *IEEE Transactions on Biomedical Engineering*, vol. 53, no. 12, pp. 2425–2435, 2006.
- [75] J. Mayourian, E. A. Sobie, and K. D. Costa, “An introduction to computational modeling of cardiac electrophysiology and arrhythmogenicity,” *Experimental Models of Cardiovascular Diseases: Methods and Protocols*, pp. 17–35, 2018.
- [76] E. A. Heidenreich, J. M. Ferrero, M. Doblaré, and J. F. Rodríguez, “Adaptive macro finite elements for the numerical solution of monodomain equations in cardiac electrophysiology,” *Annals of Biomedical Engineering*, vol. 38, pp. 2331–2345, 2010.
- [77] K. A. Mountris and E. Pueyo, “A dual adaptive explicit time integration algorithm for efficiently solving the cardiac monodomain equation,” *International Journal for Numerical Methods in Biomedical Engineering*, vol. 37, no. 7, p. e3461, 2021.
- [78] K. A. Mountris and E. Pueyo, “Cardiac electrophysiology meshfree modeling through the mixed collocation method,” *Applied Sciences*, vol. 13, no. 20, p. 11460, 2023.
- [79] K. A. Mountris and E. Pueyo, “The radial point interpolation mixed collocation method for the solution of transient diffusion problems,” *Engineering Analysis with Boundary Elements*, vol. 121, pp. 207–216, 2020.
- [80] A. Bueno-Orovio, E. M. Cherry, and F. H. Fenton, “Minimal model for human ventricular action potentials in tissue,” *Journal of Theoretical Biology*, vol. 253, no. 3, pp. 544–560, 2008.
- [81] J. Q. Gong, M. E. Susilo, A. Sher, C. J. Musante, and E. A. Sobie, “Quantitative analysis of variability in an integrated model of human ventricular electrophysiology and β -adrenergic signaling,” *Journal of Molecular and Cellular Cardiology*, vol. 143, pp. 96–106, 2020.
- [82] M. Paci, J. Hyttinen, K. Aalto-Setälä, and S. Severi, “Computational models of ventricular-and atrial-like human induced pluripotent stem cell derived cardiomyocytes,” *Annals of Biomedical Engineering*, vol. 41, pp. 2334–2348, 2013.

- [83] L. Cardone-Noott, A. Bueno-Orovio, A. Mincholé, N. Zemzemi, and B. Rodriguez, “Human ventricular activation sequence and the simulation of the electrocardiographic qrs complex and its variability in healthy and intraventricular block conditions,” *EP Europace*, vol. 18, no. suppl_4, pp. iv4–iv15, 2016.
- [84] S. A. Maas, B. J. Ellis, G. A. Ateshian, and J. A. Weiss, “Febio: Finite elements for biomechanics,” *Journal of Biomechanical Engineering*, vol. 134, p. 011005, 02 2012.
- [85] M. Cruz-Lemini, F. Crispi, B. Valenzuela-Alcaraz, F. Figueras, O. Gómez, M. Sitges, B. Bijmens, and E. Gratacós, “A fetal cardiovascular score to predict infant hypertension and arterial remodeling in intrauterine growth restriction,” *American Journal of Obstetrics and Gynecology*, vol. 210, no. 6, pp. 552–e1, 2014.
- [86] K. Gima and Y. Rudy, “Tonic current basis of electrocardiographic waveforms: a model study,” *Circulation Research*, vol. 90, no. 8, pp. 889–896, 2002.
- [87] G. E. Dower, H. B. Machado, and J. A. Osborne, “On deriving the electrocardiogram from vectorcardiographic leads,” *Clinical Cardiology*, vol. 3, no. 2, pp. 87–95, 1980.
- [88] P. Laguna, R. Jané, and P. Caminal, “Automatic detection of wave boundaries in multilead ecg signals: Validation with the cse database,” *Computers and Biomedical Research*, vol. 27, no. 1, pp. 45–60, 1994.
- [89] J. P. Martínez, R. Almeida, S. Olmos, A. P. Rocha, and P. Laguna, “A wavelet-based ecg delineator: evaluation on standard databases,” *IEEE Transactions on Biomedical Engineering*, vol. 51, no. 4, pp. 570–581, 2004.
- [90] L. Chen, Z. Jiang, J. Barker, H. Zhou, F. S. Schlindwein, W. Nicolson, G. A. Ng, and X. Li, “Ecgvednet: A variational encoder-decoder network for ecg delineation in morphology variant ecgs,” *IEEE Transactions on Biomedical Engineering*, 2024.
- [91] I. N. Tchoupe, M. D. Diaw, S. Papelier, A. Durand-Salmon, and J. Oster, “Neural network-based ecg delineation,” *Computing in Cardiology*, vol. 51, pp. 1–4, 2024.

- [92] F. Castells, P. Laguna, L. Sörnmo, A. Bollmann, and J. M. Roig, "Principal component analysis in ecg signal processing," *EURASIP Journal on Advances in Signal Processing*, vol. 2007, pp. 1–21, 2007.
- [93] V. Monasterio, P. Laguna, and J. P. Martinez, "Multilead analysis of t-wave alternans in the ecg using principal component analysis," *IEEE Transactions on Biomedical Engineering*, vol. 56, no. 7, pp. 1880–1890, 2009.
- [94] J. Ramírez, M. Orini, J. D. Tucker, E. Pueyo, and P. Laguna, "Variability of ventricular repolarization dispersion quantified by time-warping the morphology of the t-waves," *IEEE Transactions on Biomedical Engineering*, vol. 64, p. 1619, 2017.
- [95] F. Figueras, E. Meler, A. Iraola, E. Eixarch, O. Coll, J. Figueras, A. Francis, E. Gratacos, and J. Gardosi, "Customized birthweight standards for a spanish population," *European Journal of Obstetrics & Gynecology and Reproductive Biology*, vol. 136, no. 1, pp. 20–24, 2008.
- [96] F. Crispi, B. Bijnsens, F. Figueras, J. Bartrons, E. Eixarch, F. L. Noble, A. Ahmed, and E. Gratacós, "Fetal growth restriction results in remodeled and less efficient hearts in children," *Circulation*, vol. 121, pp. 2427–2436, 6 2010.
- [97] H. Martinez-Navarro, A. Mincholé, A. Bueno-Orovio, and B. Rodriguez, "High arrhythmic risk in antero-septal acute myocardial ischemia is explained by increased transmural reentry occurrence," *Scientific reports*, vol. 9, no. 1, p. 16803, 2019.
- [98] A. Mincholé, E. Zacur, R. Ariga, V. Grau, and B. Rodriguez, "Mri-based computational torso/biventricular multiscale models to investigate the impact of anatomical variability on the ecg qrs complex," *Frontiers in Physiology*, vol. 10, p. 1103, 2019.
- [99] F. S. Costabal, D. E. Hurtado, and E. Kuhl, "Generating purkinje networks in the human heart," *Journal of Biomechanics*, vol. 49, no. 12, pp. 2455–2465, 2016.
- [100] L. Dux-Santoy, R. Sebastian, J. F. Rodriguez, and J. M. Ferrero, "Modeling the different sections of the cardiac conduction system to obtain realistic electrocardiograms," *Proceedings of the Annual International Conference of the IEEE Engineering in Medicine and Biology Society, EMBS*, pp. 6846–6849, 2013.

- [101] G. K. Massing and T. N. James, "Anatomical configuration of the his bundle and bundle branches in the human heart.," *Circulation*, vol. 53, no. 4, pp. 609–621, 1976.
- [102] D. Rohmer, A. Sitek, and G. T. Gullberg, "Reconstruction and visualization of fiber and laminar structure in the normal human heart from ex vivo diffusion tensor magnetic resonance imaging (dtmri) data," *Investigative Radiology*, vol. 42, no. 11, pp. 777–789, 2007.
- [103] M. J. Bishop, P. Hales, G. Plank, D. J. Gavaghan, J. Scheider, and V. Grau, "Comparison of rule-based and dtmri-derived fibre architecture in a whole rat ventricular computational model," in *Functional Imaging and Modeling of the Heart: 5th International Conference, FIMH 2009, Nice, France, June 3-5, 2009. Proceedings 5*, pp. 87–96, Springer, 2009.
- [104] R. Doste, D. Soto-Iglesias, G. Bernardino, A. Alcaine, R. Sebastian, S. Giffard-Roisin, M. Sermesant, A. Berruezo, D. Sanchez-Quintana, and O. Camara, "A rule-based method to model myocardial fiber orientation in cardiac biventricular geometries with outflow tracts," *International Journal for Numerical Methods in Biomedical Engineering*, vol. 35, 4 2019.
- [105] J. D. Bayer, R. C. Blake, G. Plank, N. A. Trayanova, and J. D. Bayer, "A novel rule-based algorithm for assigning myocardial fiber orientation to computational heart models," *Annals of Biomedical Engineering*, vol. 40, pp. 2243–2254, 2012.
- [106] D.-W. Liu and C. Antzelevitch, "Characteristics of the delayed rectifier current (ikr and iks) in canine ventricular epicardial, midmyocardial, and endocardial myocytes: a weaker iks contributes to the longer action potential of the m cell," *Circulation Research*, vol. 76, no. 3, pp. 351–365, 1995.
- [107] M. V. Brahmajothi, M. J. Morales, K. A. Reimer, and H. C. Strauss, "Regional localization of erg, the channel protein responsible for the rapid component of the delayed rectifier, k⁺ current in the ferret heart," *Circulation Research*, vol. 81, no. 1, pp. 128–135, 1997.
- [108] N. Szentadrassy, T. Banyasz, T. Biro, G. Szabo, B. I. Toth, J. Magyar, J. Lazar, A. Varro, L. Kovacs, and P. P. Nanasi, "Apico-basal inhomogeneity in distribution of ion channels in canine and human ventricular myocardium," *Cardiovascular Research*, vol. 65, no. 4, pp. 851–860, 2005.

- [109] P. C. Viswanathan, R. M. Shaw, and Y. Rudy, “Effects of *ikr* and *iks* heterogeneity on action potential duration and its rate dependence: a simulation study,” *Circulation*, vol. 99, pp. 2466–2474, 5 1999.
- [110] P. Ueda, S. Cnattingius, O. Stephansson, E. Ingelsson, J. F. Ludvigsson, and A. K. E. Bonamy, “Cerebrovascular and ischemic heart disease in young adults born preterm: A population-based swedish cohort study,” *European Journal of Epidemiology*, vol. 29, pp. 253–260, 4 2014.
- [111] B. Owen, N. Bojdo, A. Jivkov, B. Keavney, and A. Revell, “Structural modelling of the cardiovascular system,” *Biomechanics and Modeling in Mechanobiology*, vol. 17, no. 5, pp. 1217–1242, 2018.
- [112] E. Zacur, A. Minchole, B. Villard, V. Carapella, R. Ariga, B. Rodriguez, and V. Grau, “Mri-based heart and torso personalization for computer modeling and simulation of cardiac electrophysiology,” *Lecture Notes in Computer Science (including subseries Lecture Notes in Artificial Intelligence and Lecture Notes in Bioinformatics)*, vol. 10549 LNCS, pp. 61–70, 2017.
- [113] F. Crispi, E. Hernandez-Andrade, M. M. Pelters, W. Plasencia, J. A. Benavides-Serralde, E. Eixarch, F. L. Noble, A. Ahmed, J. F. Glatz, K. H. Nicolaides, and E. Gratacos, “Cardiac dysfunction and cell damage across clinical stages of severity in growth-restricted fetuses,” *American Journal of Obstetrics and Gynecology*, vol. 199, pp. 254.e1–254.e8, 2008.
- [114] P. Ueda, S. Cnattingius, O. Stephansson, E. Ingelsson, J. F. Ludvigsson, and A. K. E. Bonamy, “Cerebrovascular and ischemic heart disease in young adults born preterm: A population-based swedish cohort study,” *European Journal of Epidemiology*, vol. 29, pp. 253–260, 4 2014.
- [115] H. A. Bukhari, F. Palmieri, D. Ferreira, M. Potse, J. Ramírez, P. Laguna, C. Sánchez, and E. Pueyo, “Transmural ventricular heterogeneities play a major role in determining t-wave morphology at different extracellular potassium levels,” *Computing in Cardiology*, pp. 1–4, 2019.
- [116] P. W. MacFarlane, “The frontal plane qrs-t angle,” *Europace*, vol. 14, pp. 773–775, 6 2012.
- [117] A. L. Aro, H. V. Huikuri, J. T. Tikkanen, M. J. Junttila, H. A. Rissanen, A. Reunanen, and O. Anttonen, “Qrs-t angle as a predictor of sudden cardiac death in a middle-aged general population,” *EP Europace*, vol. 14, pp. 872–876, 6 2012.

- [118] W. J. Young, J. Haessler, J.-W. Benjamins, L. Repetto, J. Yao, A. Isaacs, A. R. Harper, J. Ramirez, S. Garnier, S. van Duijvenboden, *et al.*, “Genetic architecture of spatial electrical biomarkers for cardiac arrhythmia and relationship with cardiovascular disease,” *Nature Communications*, vol. 14, no. 1, p. 1411, 2023.
- [119] A. Oehler, T. Feldman, C. A. Henrikson, and L. G. Tereshchenko, “Qrs-t angle: A review,” *Annals of Noninvasive Electrocardiology*, vol. 19, pp. 534–542, 11 2014.
- [120] I. Kardys, J. A. Kors, I. M. V. der Meer, A. Hofman, D. A. V. der Kuip, and J. C. Witteman, “Spatial qrs-t angle predicts cardiac death in a general population,” *European Heart Journal*, vol. 24, pp. 1357–1364, 7 2003.
- [121] M. V. Herman, D. A. Ingram, J. A. Levy, J. R. Cook, and R. J. Athans, “Variability of electrocardiographic precordial lead placement: A method to improve accuracy and reliability,” *Clinical Cardiology*, vol. 14, pp. 469–476, 6 1991.
- [122] U. C. Nguyễn, M. Potse, F. Regoli, M. L. Caputo, G. Conte, R. Murzilli, S. Muzzarelli, T. Moccetti, E. G. Caiani, F. W. Prinzen, *et al.*, “An in-silico analysis of the effect of heart position and orientation on the ecg morphology and vectorcardiogram parameters in patients with heart failure and intraventricular conduction defects,” *Journal of Electrocardiology*, vol. 48, no. 4, pp. 617–625, 2015.
- [123] H. Riekkinen and P. Rautaharju, “Body position, electrode level, and respiration effects on the frank lead electrocardiogram,” *Circulation*, vol. 53, no. 1, pp. 40–45, 1976.
- [124] J. C. Walker, J. M. Guccione, Y. Jiang, P. Zhang, A. W. Wallace, E. W. Hsu, and M. B. Ratcliffe, “Helical myofiber orientation after myocardial infarction and left ventricular surgical restoration in sheep,” *The Journal of Thoracic and Cardiovascular Surgery*, vol. 129, pp. 382–390, 2 2005.
- [125] J. Bolea, R. Almeida, P. Laguna, L. Sörnmo, and J. Martinez, “Biosig-browser, biosignal processing interface,” in *2009 9th International Conference on Information Technology and Applications in Biomedicine*, pp. 1–4, IEEE, 2009.
- [126] R. Almeida, J. P. Martíñez, A. P. Rocha, and P. Laguna, “Multilead ecg delineation using spatially projected leads from wavelet transform

- loops,” *IEEE Transactions on Biomedical Engineering*, vol. 56, no. 8, pp. 1996–2005, 2009.
- [127] L. S. Fridericia, “Die systolendauer im elektrokardiogramm bei normalen menschen und bei herzkranken,” *Acta Medica Scandinavica*, vol. 53, no. 1, pp. 469–486, 1920.
- [128] I. Andršová, K. Hnatkova, M. Šišáková, O. Toman, P. Smetana, K. M. Huster, P. Barthel, T. Novotný, G. Schmidt, and M. Malik, “Influence of heart rate correction formulas on qtc interval stability,” *Scientific Reports*, vol. 11, no. 1, p. 14269, 2021.
- [129] S. Luo, K. Michler, P. Johnston, and P. W. Macfarlane, “A comparison of commonly used qt correction formulae: the effect of heart rate on the qtc of normal ecgs,” *Journal of Electrocardiology*, vol. 37, pp. 81–90, 2004.
- [130] S. Dutta, K. C. Chang, K. A. Beattie, J. Sheng, P. N. Tran, W. W. Wu, M. Wu, D. G. Strauss, T. Colatsky, and Z. Li, “Optimization of an in silico cardiac cell model for proarrhythmia risk assessment,” *Frontiers in Physiology*, vol. 8, p. 616, 2017.
- [131] K. A. Mountris, C. Sanchez, and E. Pueyo, “A novel paradigm for in silico simulation of cardiac electrophysiology through the mixed collocation meshless petrov-galerkin method,” *Computing in Cardiology*, vol. 2019-Septe, 9 2019.
- [132] A. G. Kléber, M. J. Janse, and V. G. Fast, “Normal and abnormal conduction in the heart,” *Comprehensive Physiology*, pp. 455–530, 2011.
- [133] M. S. Spach, W. Miller 3rd, D. B. Geselowitz, R. C. Barr, J. M. Kootsey, and E. A. Johnson, “The discontinuous nature of propagation in normal canine cardiac muscle. evidence for recurrent discontinuities of intracellular resistance that affect the membrane currents.,” *Circulation Research*, vol. 48, no. 1, pp. 39–54, 1981.
- [134] E. Pueyo, Z. Husti, T. Hornyik, I. Baczkó, P. Laguna, A. Varró, and B. Rodríguez, “Mechanisms of ventricular rate adaptation as a predictor of arrhythmic risk,” *American Journal of Physiology-Heart and Circulatory Physiology*, vol. 298, no. 5, pp. H1577–H1587, 2010.
- [135] M. Botsch and L. Kobbelt, “A remeshing approach to multiresolution modeling,” in *Proceedings of the 2004 Eurographics/ACM SIGGRAPH Symposium on Geometry Processing*, pp. 185–192, 2004.

-
- [136] S. Hang, “Tetgen, a delaunay-based quality tetrahedral mesh generator,” *ACM Trans. Math. Softw.*, vol. 41, no. 2, p. 11, 2015.
- [137] F. L. Bueno-Palomeque, E. Zacur, E. Pueyo, F. Crispi, P. Laguna, and A. Mincholé, “Implications of iugr-related geometric heart changes on the eeg and electrophysiology: an in silico perspective,” *Computing in Cardiology*, vol. 51, pp. 1–4, 2024.
- [138] F. L. Bueno-Palomeque, K. A. Mountris, N. Ortigosa, R. Bailón, B. Bijmens, F. Crispi, E. Pueyo, A. Mincholé, and P. Laguna, “Qrs width and t-peak to t-end interval are prolonged in preadolescents with severe intrauterine growth restriction at birth when compared to controls,” in *2023 Computing in Cardiology (CinC)*, vol. 50, pp. 1–4, IEEE, 2023.
- [139] I. Mozos and C. Serban, “The relation between qt interval and t-wave variables in hypertensive patients,” *Journal of Pharmacy and Bioallied Sciences*, vol. 3, pp. 339–344, 2011.
- [140] E. P. Anyukhovskiy, E. A. Sosunov, R. Z. Gainullin, and M. R. Rosen, “The controversial m cell,” *Journal of Cardiovascular Electrophysiology*, vol. 10, no. 2, pp. 244–260, 1999.

LIST OF PUBLICATIONS

Journal Publications

- **Bueno-Palomeque, F.L.**, Mountris, K.A., Ortigosa, N., Bailón, R., Bijmens, B., Crispi, F., Pueyo, E., Mincholé, A., and Laguna, P., “QRS-T Angles as Markers for Heart Sphericity in Subjects With Intrauterine Growth Restriction: A Simulation Study,” in *IEEE Journal of Biomedical and Health Informatics*, vol. 27, no. 10, pp. 4707-4718, Oct. 2023, doi: 10.1109/JBHI.2023.3297550.
- **Bueno-Palomeque, F.L.**, Zacur, E., Pueyo, E., Crispi, F., Laguna, P. and Mincholé, A., “Electrophysiological Characterization of Preadolescents Born with Intrauterine Growth Restriction: Insights from Clinical and Computational Data”, *Journal of Physiology*, doi: 10.1113/JP288197.

Conference Publications

- **Bueno-Palomeque, F.L.**, Mountris, K.A., Mincholé, A., Ortigosa, N., Bailón, R., Pueyo, E. and Laguna, P., “Changes in QRS and T-wave Loops Subsequent to an Increase in Left Ventricle Globularity as in Intrauterine Growth Restriction: a Simulation Study”, 2020 *Computing in Cardiology*, Rimini, Italy, 2020, pp. 1-4, doi: 10.22489/CinC.2020.438.
- **Bueno-Palomeque, F.L.**, Mountris, K.A., Mincholé, A., Ortigosa, N., Bailón, R., Pueyo, E. and Laguna, P., “Variación del ángulo entre QRS y onda T del ECG en función del índice de esfericidad ventricular en sujetos con crecimiento intrauterino retardado: un estudio computacional.” *Jornada de Jóvenes Investigadores del I3A 10* (2022).

- **Bueno-Palomeque, F.L.**, Mountris, K.A., Ortigosa, N., Bailón, R., Bijns, B., Crispi, F., Pueyo, E., Mincholé, A., and Laguna, P., “QRS Width and T-Peak to T-End Interval Are Prolonged in Preadolescents with Severe Intrauterine Growth Restriction at Birth when Compared to Controls,” 2023 Computing in Cardiology (CinC), Atlanta, GA, USA, 2023, pp. 1-4, doi: 10.22489/CinC.2023.344.
- **Bueno-Palomeque, F.L.**, Zacur, E., Pueyo, E., Crispi, F., Laguna, P. and Mincholé, A., “Implications of IUGR-Related Geometric Heart Changes on the ECG and Electrophysiology: an In silico Perspective.” 2024 Computing in Cardiology (CinC), Karlsruhe, Germany, 2024, pp. 1-4, *Publication in process*.

LIST OF FIGURES

- 1.1 Longitudinal view of the heart, showing the chambers and the valve system for their connection. Regions marked in red represent the chambers and the system responsible for the conduction of oxygenated blood throughout the body. Blue regions correspond to the circulation of deoxygenated blood to the lungs for reoxygenation. Adapted from <https://smart.servier.com/> 11
- 1.2 Pericardium and heart wall with their divisions. Adapted from <https://smart.servier.com/> 12
- 1.3 This figure presents a longitudinal section of the heart, highlighting the cardiac conduction system. Adapted from <https://smart.servier.com/> 14
- 1.4 Diagram of the ventricular cell AP and the ionic exchange involved in its generation. Adapted from <https://smart.servier.com/> 16
- 1.5 The three-dimensional view of 12 ECG leads on the xyz-coordinate axis system. Adapted from [35] <https://www.mdpi.com/1424-8220/20/24/7246>. 20
- 1.6 Diagram of an ECG with representative markers at different stages of the cardiac cycle: the P wave corresponding to atrial depolarization, the QRS complex corresponding to ventricular contraction, and the T-wave corresponding to repolarization. 22

1.7	2D echocardiographic image showing the four heart chambers at the end of diastole, comparing a control subject and a subject with fetal growth restriction (FGR). The apex-to-base length and basal diameter are indicated, highlighting the more spherical shape of the heart in the FGR subject. The control heart appears more elongated in contrast. Image edited from [13]	24
2.1	a: Biventricular control model and, b and c: two globular variations obtained by applying tensile force to the free wall of the LV. The color blue indicates regions without deformation, while the color red represents maximum deformation.	43
2.2	*.stl file of the human biventricular model in PreView software, showing surface regions assigned with zero mobility ($f_x(x_k), f_y(y_k), f_z(z_k) = 0$) as reference and the forces applied to the LV endocardial surface to achieve the globular models.	44
2.3	General diagram of the stages for ECG signal processing [23].	46
2.4	Five levels of WT interval scales from a simulated ECG signal. Adapted from [89].	47
2.5	8-lead ECG (I, II, V1 to V6) and the first three principal components of the signals. Marks are shown at the onset of the QRS, R-wave, and the onset, peak, and end of the T-wave, with different colors for each lead. The PCA transform is applied to the entire ECG waveform.	49
3.1	Propagation sequence of the AP. a: Simulation with manual selection of the regions where the stimulus initiates, and b: Simulation using a Purkinje network. The blue color represents an AP of -80 mV, and the red color represents +20 mV.	54
3.2	a: Endocardial surface of the right (red) and left (blue) ventricles. b: Main branch of the Purkinje network extending from the bundle of His towards the ventricles. c: Purkinje network on the ventricular endocardial surface.	55
3.3	Distribution of the Purkinje network on the endocardial surface of both ventricles, shown with white lines. The main branch and its division towards the ventricles are highlighted in green.	56

- 3.4 Each PMJ of the Purkinje network connects to the endocardial surface with the nodes located within a radius of 0.1 cm. The propagation can be seen starting from the bundle of His ($t=4$ ms), and on the right, the propagation from $t=29$ ms to $t=30$ ms is shown through the selection of nodes on the endocardial surface. 57
- 3.5 a: Right and left ventricular borders and apex labeled for fiber direction generation algorithm import, b: Detected epicardial surface, c: Complete model surface, d: RV endocardium, e: LV endocardium, f: Myocardium of the model, g: Fiber orientation per node from endocardium to epicardium. 60
- 3.6 Simulated AP on a 2D surface represented as epi, endo, and mid tissue at $t=60, 100, 200,$ and 300 ms. On the right, the AP is shown on a node with the entire surface modeled as epi, endo, and mid cells. 62
- 3.7 Representation of the algorithm for dividing cardiac tissue into endo, mid, and epi. The red circles represent nodes \mathbf{n}_{ken} and \mathbf{n}_{kepi} ; their distance is calculated and then divided into percentages according to r_{en} and r_{epi} , which are the radius of the spheres within which the nodes are selected as endo or epi. 63
- 3.8 Pseudo ECG from the simulation of 3 heartbeats on a biventricular model, showing the effect of incorporating apex-to-base heterogeneities in red compared to the simulation without apex-to-base heterogeneities in blue. 66
- 3.9 Biventricular human model with incorporated transmural and apex-to-base heterogeneities. 67
- 3.10 Propagation of the AP along a 2D surface at time $t=180$ and 280 ms for endo tissue, $t=220$ and 280 ms for mid tissue, and $t=200$ and 280 ms for epi tissue. On the bottom, the AP curve is shown for endo, mid, and epi tissue. The reference curve from the human model by ORd, without scaling, is added in black. 68
- 3.11 The upper part shows, through the color map, the nodal displacement obtained as a result of the deformation of the original control model \mathcal{C} . The Y and Z axes were associated with the deformation in the ϕ and in the \mathcal{L} , respectively. The eight \mathcal{G} models resulting from combining the deformations in Y and Z axes were shown at the bottom. 71

- 3.12 Displacement tests description for \mathcal{C} model, C334 configuration, when displacing mesh nodes by 5, 10, and 15 mm. a) location grid around a red point representing one node of the mesh and its relocation. Each gray point represents the displacement of each of the nodes of the model in any direction. 120 \mathbf{d}_k displacements were made around the original point, at 5, 10, and 15 mm. b) QRS and T-wave vectors and their angles with respect to the three corporal planes. Note that T-wave (red line) and QRS (blue line) loops have a similar dominant vector direction. 72
- 3.13 Parameters considered on the \mathcal{C} and \mathcal{G} models. a) Mesh segmentation considering transmural (endo/mid/epi myocardium) and gradient heterogeneities (apex/intermediate/base, dark blue to light blue), b) Purkinje network on the endocardial surface, c) fiber orientation from endocardial (blue lines) to epicardial surface (red lines), and d) color map showing the nodal displacement on the \mathcal{C} model to obtain the \mathcal{G} models. 73
- 3.14 Heart model embedded in the torso with virtual electrodes on its surface (precordial leads V1 to V6 and limb leads RL, RA, LL, and LA). 74
- 3.15 Loops and dominant vectors of depolarization and repolarization in the three reference planes: frontal, sagittal, and transverse. The QRS complex loop is shown in blue, and the T-wave loop is shown in red. The dashed line represents the dominant vectors of depolarization and repolarization. a: VCG and the three planes, b: Projection of the QRS vector onto the XY plane, with the angle highlighted in orange, c: Angles of the dominant vectors with respect to the YZ-Sagittal plane, d: With respect to the XZ-Transverse plane, and e: With respect to the XY-Frontal plane. 75
- 3.16 List of the different transmural tissue heterogeneities configurations. Columns and rows indicate the percentage of endocardium and epicardium respectively. Bold lines correspond to configurations with inter-middle (C334) and extremes (C136 and C532) T-wave amplitudes. X, Y, and Z leads computed using the biventricular model at the \mathcal{C} case, combining different endo-mid-epi tissue ratios configurations, C_{uvw} . Dotted lines show QRS and T-wave time intervals from where the dominant vectors were computed. 77

- 3.17 Depolarization and repolarization angles, plotted with a bias $\Delta\theta$ or $\Delta\phi$ reported on each column top, for visualization purposes. Each column corresponds to an angle and includes three subplots. The leftmost subplots include the angles estimate from \mathcal{C} case for the 15 different C_{uvw} transmural configurations, representing the central configurations (endo having 20%, 30%, and 40%) in dark green, with percentiles boxplot, and in light green otherwise except the reference C334 which is plotted in black square; the two extreme cases of C136 and C532, were surrounded by square and diamond, respectively. The middle plots have eight colored dots, corresponding to angles estimated from the \mathcal{G}_A to \mathcal{G}_H models deriving from the control \mathcal{C} at transmural distribution C334 (black square). The rightmost subplot includes angles estimates for \mathcal{G}_G (red) and \mathcal{G}_H (brown) for the extreme transmural configurations C136 (squares) and C532 (diamond). 78
- 3.18 Temporal segmentation of the QRS loop in three parts to analyze the vector changes. QRS loop projections of the \mathcal{C} , and its evolved \mathcal{G}_G and \mathcal{G}_H models, all in C334, between 1 and 31 ms, 31 and 64 ms, and 64 and 85 ms. Dashed arrows represent the dominant vectors of the loops. 80
- 3.19 QRS, ϕ_{R-PL} , vs T-wave, ϕ_{T-PL} , angles, $PL \in \{XY, ZY, XZ\}$, from the VCG, considering a 5 (yellow), 10 (orange), and 15 (blue) mm displacement of the heart inside the torso. Each color group shows one hundred and twenty tests. The green square shows the control \mathcal{C} results, and the magenta and cyan squares correspond to the angular results for the \mathcal{G}_G and \mathcal{G}_H models without displacement, respectively. 84
- 3.20 QRS and T-wave loops in the three VCG planes. The magenta region corresponds to the angle variation when displacement $\|\mathbf{d}_k\|=5$ mm in any direction. QRS and T-wave loops correspond to the \mathcal{G}_G model simulation. Dotted lines represent the dominant vectors. 86
- 4.1 Identification and marking of the P wave, QRS complex, and T-wave across each of the 8 ECG leads. The blue dotted lines are aligned with the markers of lead V2 to illustrate that the markers for each lead are different when a selection rule is not applied. 95

- 4.2 12-lead ECG with annotations following a multilead rule. The onset, peak, and end of the QRS complex and T-wave are shown. The red dashed lines indicate the markers, now aligned across all leads. 96
- 4.3 Detection of the median in IUGR subject #33 on lead I. The QRS median is a single value, while the $T_{pe,c}$ median is the average of the two observed values, as containing an even number of beats with $T_{pe,c}$ measurement. 97
- 4.4 The independent 8 ECG leads from a subject in the control group with marks on QRS onset and end, R-wave peak, T-wave onset, peak, and end with red long lines. Similarly, PCA_T and PCA_{QRS} first leads include annotations marked as red lines over the leads together with definitions of the intervals of interest (T_{pe} , QT, and QRS) shaded in purple. 99
- 4.5 Changes in $T_{pe,c}$, QT_c , $T_{pe,c}/QT_c$, and QRS width for control (blue) and IUGR (orange) groups measured on the optimally spatially transformed leads (PCA_{QRS} and PCA_T). Central red lines indicate the median and the bottom and top edges of the box show the 25th and 75th percentiles, respectively. 103
- 5.1 a: Implementation of the Purkinje network on the endocardial surface of the models. The red circle indicates the His Bundle where electrical propagation begins. b: Implementation of fibers and propagation direction at each node from the endocardial to the epicardial surface. c: Division of the tissue into 9 zones incorporating transmural (endo, mid, and epi tissue) and apicobasal heterogeneities (base (**B**), middle (**M**), and apex (**A**)). 109
- 5.2 Purkinje network for the control model in orange and the globular model \mathcal{G}_6 in blue. The same network was adapted to the endocardial surface of the globular models. 110
- 5.3 Cross-sectional view of the control model $\mathcal{C}(30-30-40)$ with 30% endocardium, 30% mid-myocardium, and 40% epicardium, and for $\mathcal{C}(48-4-48)$ model with its corresponding transmural distribution. 111

- 5.4 The standard 8-leads ECG, from the simulated control \mathcal{C} model, with marks on QRS and T-wave onset and end points indicated with black dashed lines, and QRS and T peaks with red squares and circles, respectively. QRS_d interval measured over PCA_{QRS} is shaded in orange and T_{pe} and QT intervals measured over PCA_T are shaded in red. 113
- 5.5 Eight \mathcal{G} models generated from \mathcal{C} model. The cross-section of the models allows for the observation of changes in \mathcal{L} , ϕ , SpI, \mathcal{W} , and VTV. The direction of the arrows indicates the direction of change in the simulated parameters. 116
- 5.6 Selection of endocardial and epicardial nodes for AP analysis. The ventricular wall thickness was divided into percentages, with one node selected in the basal endocardial section (P1-blue circle) and two nodes in the epicardial section (P2-green circle and P3-magenta circle). 117
- 5.7 a: QRS complex in lead PCA_{QRS} of the \mathcal{C} model and \mathcal{G}_i models, with the marks of the QRS_{onset} , QRS peak, and the QRS_{end} . b: T_{pe} in PCA_T lead of the \mathcal{C} and \mathcal{G}_i models with the marks of the T peak, and the T_{end} 119
- 5.8 a: AT and APD at three nodes of the mesh, P1_{endo} on an intermediate node of the endo-base section, P2_{epi} on the middle epi-base section, and P3_{epi-e} on the external surface of the epi-base section. b: A contrast between RT and AT is presented, considering the three selected nodes. The upper part of the figure outlines the location of these nodes within the heart volume. 123
- 5.9 AT maps on the LV of each globular model. The control model is displayed at the top. 124
- 5.10 Eight independent standard ECG leads, together with PCA_{QRS} , and PCA_T leads for each \mathcal{G}_i model, overprinted with the ECGs from \mathcal{C} model. The third beat of each simulation was represented. 125

LIST OF TABLES

1.1	Characteristics of the studies included in this research	29
2.1	Inverse Dower matrix coefficients	45
3.1	Base-apex length \mathcal{L} , basal diameter ϕ , and sphericity index SpI feature values from echocardiographic measurements, with statistical difference between patient groups, [13] and the same morphology measurements in the simulations models \mathcal{C} and \mathcal{G}_A to \mathcal{G}_H deformed models variants.	70
3.2	QRS and T-wave angles using different transmural heterogeneities on \mathcal{G}_G model. Δ and \mathcal{R} , angle difference and ratio, respectively, between deformed \mathcal{G}_G and control \mathcal{C} models. Bold, and underlined, font highlights the angles which tendency of change between \mathcal{G}_G and \mathcal{C} models follows similar trend to clinical results between IUGR and control for preadolescents [14], and adults [15], respectively.	82

- 3.3 Results are presented in three blocks: the leftmost block represents the clinical data for preadolescents, the central block represents the clinical data for adults, and the rightmost block represents the simulation results. The loop angle values are reported as mean \pm standard deviation or interquartile range. Simulation results display the angles obtained for deformation \mathcal{G}_G and control \mathcal{C} in configuration C334. The angles that exhibit a tendency of change between \mathcal{G}_G and \mathcal{C} models, similar to the tendency observed between IUGR and control subjects for preadolescents [14], are highlighted in bold. Likewise, for adults [15], the angles are underlined. Significant differences *p-value<0.05, **p-value<0.01. 83
- 3.4 Angle value for model \mathcal{C} with no displacement, and \pm standard deviation (\pm SD) when $\|\mathbf{d}_k\| \neq \mathbf{0}$. Bold font highlights the larger SD. Note that the angle value for $\|\mathbf{d}_k\| = \mathbf{0}$ is the same as the mean angle for $\|\mathbf{d}_k\| \neq \mathbf{0}$ 85
- 4.1 Measurements of QRS_d , $T_{pe,c}$, and QT_c intervals, and QRS_a and T_a . The lower row in each lead shows the p -value obtained by comparing the two groups using the t-student test, after verifying the normality of the results. 102
- 4.2 Median and interquartile range and p -value for QRS_d , $T_{pe,c}$, QT_c , and $T_{pe,c}/QT_c$ measured on the optimally spatial transformed leads (PCA_{QRS} and PCA_T), on the control and IUGR subjects groups. The two most right columns show the results obtained in the simulation of the control and IUGR models, taking the median value of the beats. 103
- 5.1 Measurements of \mathcal{L} , ϕ , \mathcal{W} and ratio SpI in both ventricles for the \mathcal{C} and \mathcal{G} models. \mathcal{W} shows the maximum width of the LV measured at the base and the last column show the VTV of the entire ventricular mesh models. 115
- 5.2 a: ECG biomarkers from clinical data in preadolescents: control cohort (n=60) and IUGR cohort (n=33). b: ECG biomarkers computed from simulations across the \mathcal{G}_i models. All simulations used RR=1 s, so QT and T_{pe} correspond to their corrected QT_c and $T_{pe,c}$, respectively. 118

5.3	Multiple regression analysis between the geometric variables of globular models $\{\mathcal{L}, \phi, \text{ and } \mathcal{W}\}$ and the QRS_d , T_{pe} and QT intervals measured in the synthetic ECG. p_i indicates the p-value for each individual variable, while p_F represents the significance value of the model. Values with p-value < 0.05 are highlighted in bold.	121
5.4	Intervals and amplitudes measured on the control \mathcal{C} and globular \mathcal{G}_7 models with different transmural divisions: 30%, 30%, and 40% for endocardium, mid-myocardium, and epicardium, and 48%, 4%, and 48%, respectively.	122

